A Highly Granular Silicon-Tungsten Electromagnetic Calorimeter and Top Quark Production at the International Linear Collider

Jérémy Rouëné

LAL 14-154

UNIVERSITÉ PARIS-SUD XI

École Doctorale : ED517 - “Particules, Noyaux et Cosmos”

Laboratoire de l’Accélérateur Linéaire
LAL, Univ. Paris-Sud, CNRS/IN2P3, Orsay, FRANCE

DISCIPLINE : PHYSIQUE DES PARTICULES

THÈSE DE DOCTORAT

Soutenue le 30 Juin 2014
par

Jérémy ROUËNÉ

Calorimètre électromagnétique silicium-tungstène hautement granulaire

Production du quark top à l’International Linear Collider

Composition du Jury :

Prof.	Achille STOCCHI	Président du jury
Prof.	Hitoshi YAMAMOTO	Rapporteur
Prof.	Werner BERNREUTHER	Rapporteur
Dr.	Matthew WING	Examinateur
Dr.	Maxim TITOV	Examinateur
Dr.	Roman PÖSCHL	Directeur de thèse
Dr.	François RICHARD	Membre invité

Thèse préparée au
Laboratoire de l'Accélérateur Linéaire - UMR8607
Centre Scientifique d'Orsay, Bât. 200, BP 34
91898 Orsay CEDEX

Résumé

Cette thèse porte sur deux aspects de l'International Linear Collider (ILC) qui est un projet d'un collisionneur linéaire électron-positron avec une énergie dans le centre de masse pouvant aller jusqu'à 500 GeV.

Le premier aspect est l'élaboration d'un calorimètre électromagnétique silicium-tungstène (SiW-ECAL) pour l'un des détecteurs de l'ILC. Le concept de ce détecteur est piloté par les spécifications du faisceau de l'ILC et par l'algorithme du Particle Flow (PFA). Cela nécessite un calorimètre hautement granulaire et très compact avec l'électronique directement intégrée à l'intérieur. Pour prouver les capacités du SiW-ECAL, un prototype technologique a été construit et testé en faisceau de test à DESY. Les résultats sont présentés ici et montrent, après la procédure de calibration, un signal sur bruit de 10, même en mode power pulsing.

Le deuxième aspect est l'étude de l'un des canaux physique importants de l'ILC, la production de pairs de quark top anti-top. L'objectif principal de cette étude est de déterminer la précision que nous pouvons attendre à l'ILC sur le couplage du top avec le boson W et le photon. Pour obtenir cette précision différentes observables sont utilisées, la section efficace, l'asymétrie avant - arrière et la distribution d'hélicité de la production de pairs de quark top anti-top. L'analyse est basée sur les événements avec des faisceaux polarisés et reconstruit avec la simulation complète du détecteur ILD, qui est le détecteur du SiW-ECAL, pour le Detector Baseline Design de l'ILD. Au final l'erreur attendue sur le couplage du quark top est de l'ordre de 2 %.

Mots-clefs : Calorimètre, physique des particules, quark top, ILC, CALICE.

Abstract

A Highly Granular Silicon-Tungsten Electromagnetic Calorimeter Top Quark Production at the International Linear Collider

This thesis deals with two aspects of the International Linear Collider (ILC) which is a project of a linear electron-positron collider of up to at least 500 GeV center of mass energy.

The first aspect is the development of a silicon-tungsten electromagnetic calorimeter (SiW-ECAL) for one of the detectors of the ILC. The concept of this detector is driven by the ILC beam specifications and by the Particle Flow Algorithm (PFA). This requires highly granular calorimeter and very compact one with integrated electronics. To prove the capability of the SiW- ECAL a technological prototype has been built and tested in test beam at DESY. The results are presented here, and show, after the calibration procedure a signal over noise ratio of 10, even in the power pulsing mode.

The second aspect is the study of one of the important physics channels of the ILC, the top anti-top quark pairs production. The main goal of this study is to determine the precision that we can expect at the ILC on the top coupling with the W boson and the photon. To get this precision differents observables are used, the cross- section, the forward- backward asymmetry and the helicity distribution of the top anti-top quark pairs production. The analysis is based on the events with polarized beams and reconstructed with the full simulation of the ILD detector, which is the detector of the SIW- ECAL, for the Detector Baseline Design of the ILD. The final expected errors on the top coupling is of the order of 2%.

Keywords : Calorimeter, particles physics, top quark, ILC, CALICE.

Remerciements

Je voudrais remercier le directeur du Laboratoire de l'Accélérateur Linéaire, Achille STOCCHI, ainsi que tout le personnel pour m'avoir permis d'effectuer ma thèse dans d'excellentes conditions pendant ces trois ans.

Je remercie également les membres de mon jury, Prof. Hitoshi YAMAMOTO, Prof. Werner BERNREUTHER, Dr. Matthew WING, et Dr. Maxim TITOV, de me faire l'honneur de leur présence.

Je veux bien évidemment remercier mon directeur de thèse, Dr. Roman PÖSCHL, pour m'avoir laissé travailler de manière autonome, tout en étant toujours présent quand j'avais besoin de lui.

Je remercie également mes collègues, François, Philippe, Thibault, Amjad, Naomi et tous les autres pour leur aide et leurs conseils.

Je tiens aussi à remercier M. Benoît de Préville qui m'a donné le goût pour la physique en prépa et m'a encouragé à poursuivre dans cette voie.

Finalement je remercie mes amis et ma famille, mes frères Loris et Florian pour leur soutien, bien que, malgré mes tentatives d'explication, ils doivent toujours se demander ce que j'ai bien pu faire pendant ces trois années de thèse.

Et enfin je remercie Anne-Gaëlle pour son soutien et pour avoir supporté mes nombreux déplacements à l'étranger. Notre aventure Parisienne se termine avec ma thèse, et nous allons pouvoir rentrer chez nous pour commencer une aventure encore plus excitante en tant que parents.

à mes parents, Gisèle et Alain

Contents

Part I

General Introduction

In this part I will give a general overview of the theory fields of the thesis, the Standard Model of particle physics, and of the International Linear Collider and one of its detectors the ILD.

In Chapter 1 I will present the Standard Model which is the global theory scope of the particle physics. It had great success to predict new particles and is, so far, undefeated. In Chapter 2 I will introduce the International Linear Collider which is a project of a linear electron-positron collider and should characterize the last success of the standard model: the Higgs boson, but also try to take to default this one. The ILD, one of the detector of the ILC, based on the Particle Flow Algorithm will also be described in Chapter 3.

Chapter 1

The Standard Model of Particles Physics

The Standard Model of particle physics was developed in the 70's to provide a consistent theoretical description of elementary particles and the fundamental forces acting between them [1]. Indeed the Standard Model describes the interaction of the matter, the elementary particles, with the electromagnetic, the weak and the strong interaction, but not, so far, with the gravitation. Despite this shortcoming, as the energy scale of the gravitation is orders of magnitude different from the one of the Standard Model the gravitation doesn't play a role at this scale, and the Standard Model remains undefeated by the experiments. The elementary particles of the Standard Model are the components of matter and the force-carriers of the interactions (see Figure 1.1). They are separated into two types, the fermions which are spin 1/2 particles and the bosons featuring an integer spin, as presented in the next section.

1.1 The Particles of the Standard Model

1.1.1 The fermions

The 12 fermions are the constituents of the matter, and can be subdivided further into six leptons and quarks. Leptons and quarks are further grouped into three families each. The Standard Model is a relativistic quantum field theory with gauge symmetries.

The fermions are classified in left-handed doublets and right-handed singlets under $SU(2)_L$ and have a charge under $U(1)_Y$ called hypercharge (Y).The relation between the hypercharge and the electric charge Q comes from the breaking of the electroweak group $SU(2)_L \times U(1)_Y$ to $U(1)_{em}$ the usual electromagnetic group,

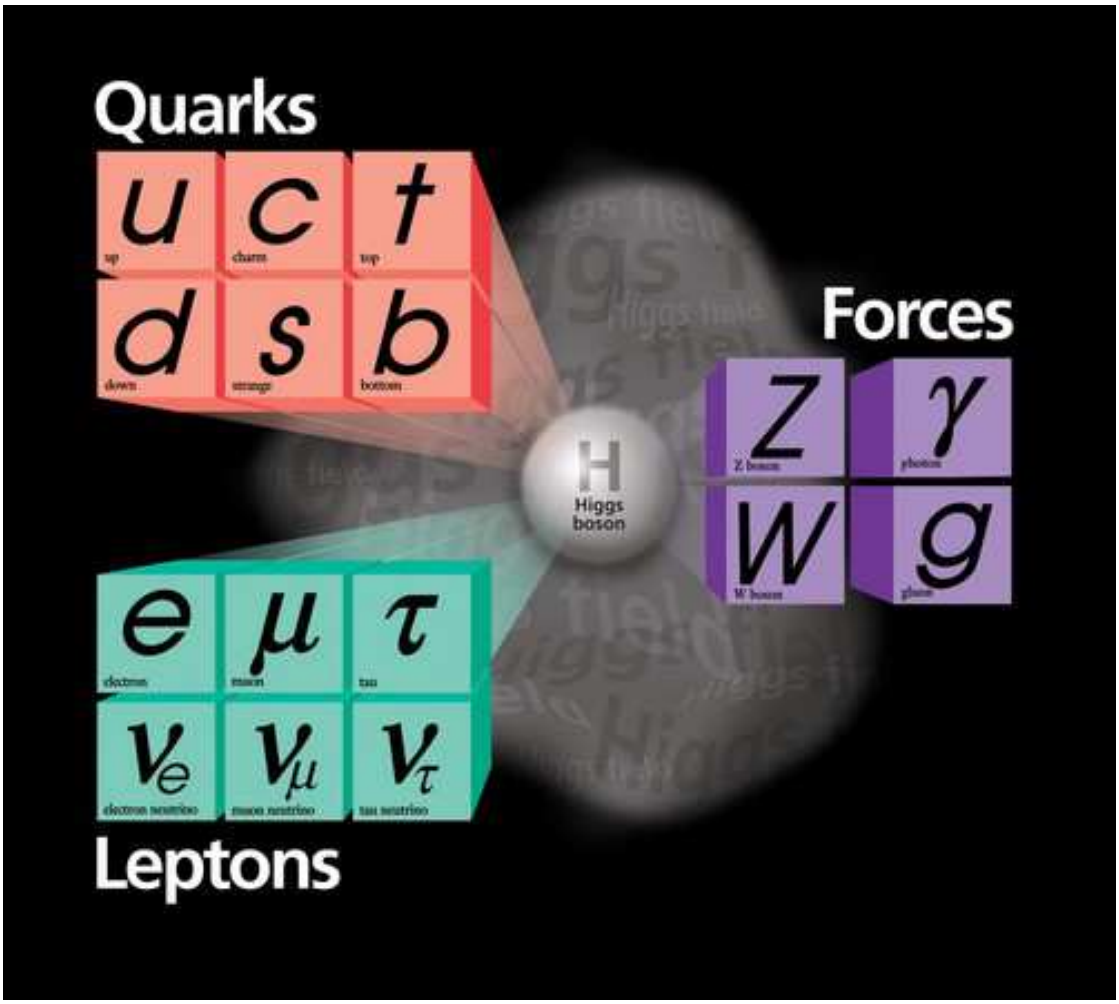

Figure 1.1: The components of the Standard Model of particle physics.

and is given by:

$$Q = I_3^L + Y \tag{1.1}$$

where I_3^L is the third component of the $SU(2)_L$ isospin.

The particles which interact via the strong interaction, carry a color charge C. This is the case for the quarks which are triplets under $SU(3)_C$ while leptons, which don't have color charge, are color singlets.

As a result, the gauge group of the Standard Model is $SU(3)_C \times SU(2)_L \times U(1)_Y$ where the $SU(3)_C$ group describe the strong interactions and the $SU(2)_L \times U(1)_Y$ the electroweak interactions.

The quantum numbers of the fermions in the Standard Model are summarized in the following table:

Family			Q	I	I_3	C
$\begin{pmatrix} \nu_e \\ e \end{pmatrix}_L$	$\begin{pmatrix} \nu_\mu \\ \mu \end{pmatrix}_L$	$\begin{pmatrix} \nu_\tau \\ \tau \end{pmatrix}_L$	0 -1	1/2	$+1/2$ $-1/2$	0
ν_{eR}	$\nu_{\mu R}$	$\nu_{\tau R}$	0	0	0	
e_R	μ_R	τ_R	-1			
$\begin{pmatrix} u \\ d \end{pmatrix}_L$	$\begin{pmatrix} c \\ s \end{pmatrix}_L$	$\begin{pmatrix} t \\ b \end{pmatrix}_L$	$+2/3$ $-1/3$	1/2	$+1/2$ $-1/2$	1
u_R	c_R	t_R	$+2/3$	0	0	
d_R	s_R	b_R	$-1/3$			

1.1.2 The Bosons

The other types of elementary particles are the bosons which are the force-carriers of the interactions. There are two types of bosons, the vector bosons, with spin 1, which mediate the fundamental interaction and the scalar boson, the Higgs with a spin 0 (see Section 1.3). Among the vector bosons the photon mediates the electromagnetic interaction. It is massless and couples to electrically charged particles. The three bosons Z^0 and $W^\pm$ mediate the weak force. They are massive, around $80 - 90\,GeV$ and couple to all the fermions. Finally there are 8 massless gluons which mediate the strong interaction and couple to particles with a color charge.

1.2 The Fundamental Forces in the Standard Model

1.2.1 A simple example: the Electromagnetic interaction

The electromagnetic interaction is described by the Maxwell equations in classical mechanics. The quantum electrodynamics, QED, is the extension of the Maxwell equations to quantum mechanics. QED is a quantum field theory of the

gauge group $U(1)_{em}$, where the equations of motion of the system are computable from a Lagrangian density $\mathcal{L}$, containing all the information of the system.

Considering the field of an electrically charge fermion $\psi(x)$, the associated Lagrangian density is:

$$\mathcal{L} = i\bar{\psi}(x)\gamma^{\mu}\partial_{\mu}\psi(x) - m\bar{\psi}(x)\psi(x) \tag{1.2}$$

where the γ^{μ} are the Dirac matrices and m the mass of the fermion.

This Lagrangian should be invariant under the local phase invariance:

$$\left\{ \begin{array}{rcl} \psi(x) & \rightarrow & e^{i\alpha(x)}\psi(x) \\ \bar{\psi}(x) & \rightarrow & e^{-i\alpha(x)}\bar{\psi}(x) \end{array} \right. \tag{1.3}$$

This transformation has no influence for $m\bar{\psi}(x)\psi(x)$ but for $i\bar{\psi}(x)\gamma^{\mu}\partial_{\mu}\psi(x)$:

$$\begin{array}{rcl} i\bar{\psi}(x)\gamma^{\mu}\partial_{\mu}\psi(x) & \rightarrow & i\bar{\psi}(x)e^{-i\alpha(x)}\gamma^{\mu}\left[e^{i\alpha(x)}\left(i\partial_{\mu}\psi(x) - (\partial_{\mu}\alpha(x))\psi(x)\right)\right] \\ & = & i\bar{\psi}(x)\gamma^{\mu}\partial_{\mu}\psi(x) - \bar{\psi}(x)\gamma^{\mu}(\partial_{\mu}\alpha(x))\psi(x) \end{array} \tag{1.4}$$

The extra term $\bar{\psi}\gamma^{\mu}(\partial_{\mu}\alpha)\psi$ can be absorbed by a gauge transformation of an A field, with the introduction of the $eA_{\mu}\bar{\psi}\gamma^{\mu}\psi$ term in the Lagrangian, where the gauge field A_{μ} transform as:

$$A_{\mu}(x) = eA_{\mu}(x) + \frac{1}{e}\partial_{\mu}\alpha(x)A_{\mu} \tag{1.5}$$

Then the final Lagrangian

$$\mathcal{L} = -\frac{1}{4}F_{\mu\nu}F^{\mu\nu} + i\bar{\psi}(x)\gamma^{\mu}\partial_{\mu}\psi(x) - m\bar{\psi}(x)\psi(x) + eA_{\mu}(x)\bar{\psi}(x)\gamma^{\mu}\psi(x) \tag{1.6}$$

where $-\frac{1}{4}F_{\mu\nu}F^{\mu\nu}$ ($F^{\mu\nu} = \partial^{\mu}A^{\nu} - \partial^{\nu}A^{\mu}$) is the massless photon field. This Lagrangian is invariant under the $U(1)_{em}$ gauge transformation, defined in Equation 1.3, and is the only renormalisable theory of $\psi, \bar{\psi}$ and A having this symmetry. The term $eA_{\mu}\bar{\psi}\gamma^{\mu}\psi$ describes the interaction between the massless photon and the electrically charge fermion $\psi(x)$. This coupling is proportional to the elementary charge e and to the coupling constant of QED, $\alpha = \frac{e^2}{4\pi} \approx \frac{1}{137}$. In fact the coupling constant α is not a constant but depends on the energy Q of the reaction. Indeed, an electron can emit virtual photons which may convert into e^-e^+ pairs and the electron is then surrounded by a cloud of e^+e^- pairs. The charge of the electron is thus screened by this cloud and appears to be lower while a probe moving closer to the electron, so a larger Q^2, would feel an increasing charge when penetrating the cloud.

This effect is a consequence of the higher order corrections. In particle physics every process can be represented by Feynman Diagrams [2] containing the initial and the final state particles, the vertex of the interactions and the intermediate virtual particles. Figure 1.2(a) shows an example of the simplest Feynman Diagrams of a fermion pair production in e^+e^- annihilation. These types of diagrams are called tree level or lowest order, by opposition to higher order corrections diagrams. Higher order corrections diagrams contain more than two vertices, as shown in Figure 1.2(b). The cross section of a process is proportional to the square of the transition matrix element at a vertex. The higher corrections added new vertices to a reaction, but the cross section should stay finite, so the divergent corrections should annihilate. To minimize the contribution of higher order correction diagrams to a given calculation one chooses a renormalization point, depending on the energy scale of the reaction, which will affect how much of a result comes from tree level Feynman diagrams and how much comes from the higher order diagrams. In renormalizable theory, like the Standard Model, the results are independant of the choice of this renormalization point.

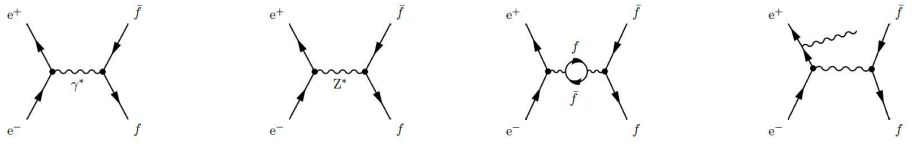

(a) (b)

Figure 1.2: Feynman Diagrams for the fermion pair production $e^+e^- \rightarrow f\bar{f}$: (a) Examples of lowest order diagrams. (b) Examples of higher order QED corrections.

This simple example of the QED can be generalized for the electroweak and the strong interaction.

1.2.2 Electroweak interactions

The electroweak interaction is a result of the unification of the electromagnetic and weak interaction. The weak interaction is carried by spin-1 bosons and acts on all the fermions. Unlike electromagnetic and strong interaction, where the photon and gluons are massless, its force carriers are massive particles, this leads to a very short interactions range. The weak interaction is responsible for many rare reactions, such as the beta decay ($n \rightarrow pe^-\bar{\nu_e}$) which was historically the first hint for this reaction. The weak interaction was firstly seen as an effective theory due to the exchange of massive charged bosons, as proposed by Fermi in 1933 [3]. Not like in QED, where the electromagnetic current (derived from Equation 1.6)

is $\bar{\psi}\gamma^\mu\psi$, the weak current is defined as $\bar{\psi}\gamma^\mu(1-\gamma_5)\psi$ and is called vector-axial vector structure (V-A structure). This change in the structure has an important effect on the left-handed, ψ_L, and right-handed, ψ_R, part of the fermions. Indeed, where the electromagnetic interaction has both left and right coupling, the weak interaction only has $\bar{\psi}_L - \psi_L$ coupling (only $\bar{\psi}_R - \psi_R$ for anti-fermions).

Later on, in the 60's, the unification of the weak interaction with the electromagnetic interaction by Glashow, Salam and Weinberg [4][5][6] leads to a new vision of the weak interaction, with predictions like neutral current and a new neutral vector boson Z^0. The theory was confirmed by the discovery of neutral current in 1973 in the Gargamelle [7] experiment at CERN, and of the $W^\pm$ and Z^0 in 1983 [8][9] at the SPS accelerator at CERN.

Starting from $SU(2)_L \times U(1)_Y$ the electroweak gauge group, we defined W^i_μ $(i = 1, 2, 3)$ for the vector fields of $SU(2)_L$ which coupled left-handed fermions to the weak isospin current $(J^i)^\mu$ with the coupling g, and B_μ the vector field of $U(1)_Y$ which coupled both left and right-handed fermions to the weak hypercharge (see Equation 1.1) current $(j^Y)^\mu$ with the coupling $g'/2$. Then the basic electroweak interaction is:

$$-ig(J^i)^\mu W^i_\mu - i\frac{g'}{2}(j^Y)^\mu B_\mu \tag{1.7}$$

If we introduce the Weinberg or weak mixing angle $\sin\theta_W$, the relation between W^i_μ and B_μ and the mass eigenstate vector bosons $W^\pm, Z^0$ and the photon is:

$$\begin{array}{rcl} W^\pm_\mu & = & \frac{1}{\sqrt{2}}(W^1_\mu \mp iW^2_\mu) \\ Z_\mu & = & -B_\mu \sin\theta_W + W^3_\mu \cos\theta_W \\ A_\mu & = & B_\mu \cos\theta_W + W^3_\mu \sin\theta_W \end{array} \tag{1.8}$$

where A_μ and Z_μ are the physical states of the photon and Z^0 boson. In order to have the same coupling for the photon as the one of the QED, we find that:

$$e = g\sin\theta_W = g'\cos\theta_W \tag{1.9}$$

The presence of the weak mixing angle in the couplings to Z_μ allows for coupling the Z^0 to both left-handed and right-handed fermions. This behavior is a fundamental difference to the W bosons that couple only to left-handed fermions.

1.2.3 Strong interaction

The strong interaction is described by the quantum chronodynamics, QCD [1]. QCD is a quantum field theory of the gauge group $SU(3)_c$ and describes the interaction between the quarks, carrying one of the three colored charge (usually labeled blue, green and red), and the fields of 8 massless gluons. The simplest

gauge invariant Lagrangian of a massless quark (for simplicity) ψ_q and massless gluons G^a_μ ($a = 1$ to 8) is:

$$\mathcal{L} = \bar{\psi_q}(i\gamma^\mu D_\mu)\psi_q - \frac{1}{4}G^a_{\mu\nu}G^{\mu\nu}_a \tag{1.10}$$

where $D_\mu = \partial_\mu - igT_aG^a_\mu$, with g the coupling constant and T^a the non-Abelian group generators. $G_{\mu\nu}$ is the analog of $F_{\mu\nu}$ in QED:

$$G^a_{\mu\nu} = \partial_\mu G^a_\nu - \partial_\nu G^a_\mu - gf_{abc}G^b_\mu G^c_\nu \tag{1.11}$$

where f_{abc} is the structure constants of $SU(3)_c$.

The non-Abelian nature of the gauge group $SU(3)_c$ leads to the fact that gluons also carry a color charge and therefore can interact with each other. This is a fundamental difference with the QED where the photon doesn't carry an electrical charge. A consequence of this is the behaviour of the running of the QCD strong coupling constant $\alpha_s = \frac{g^2}{4\pi}$. When the energy increase, or the distance becomes smaller, α_s decrease. In that case the theory is calculable with perturbation theory, via the Perturbative QCD. On the opposite when the energy decrease, or the distance becomes higher, α_s increase, and the theory is not calculable anymore, just approximated via a non-perturbative approach called Lattice QCD. This is called asymptotic freedom and confinement respectively and leads to the fact that a quark cannot be isolated, as soon as there is enough distance between two quarks, a new quark-anti-quark pair is created to have only colorless objects call hadrons.

1.3 Spontaneous Symmetry Breaking and the Higgs Boson

The gauge invariance that we have used to define the Standard Model interactions (like in Equation 1.3), implies that the spin 1 gauge bosons are massless. This is not a problem for the photon and the gluons which are massless bosons, but the $W^\pm$ and Z^0 bosons are known from measurements to be massive particles. The process called spontaneous symmetry breaking [10] can solve this problem by introducing a scalar field called the Higgs field.

1.3.1 Spontaneous symmetry breaking: the Higgs mechanism

The Lagrangian of a scalar filed is :

$$\mathcal{L} = \frac{1}{2}(\partial_\mu\phi)^2 - \frac{1}{2}\mu^2\phi^2 + \frac{1}{4}\lambda\phi^4 \tag{1.12}$$

where ϕ is a complex field:

$$\phi(x) = +\frac{1}{\sqrt{2}}[\phi_1(x) + i\phi_2(x)] \tag{1.13}$$

As the Lagrangian should be invariant under the local phase transformation like in Equation 1.3, we find the same kind of Lagrangian with an additional potential energy density of the spin 0 field:

$$\mathcal{V}(\phi) = -\frac{1}{2}\mu^2\phi^2 + \frac{1}{4}\lambda\phi^4 \tag{1.14}$$

In order to have a minimum in the solution of the potential we should have $\lambda > 0$. Then we are left with two solutions depending on the sign of μ^2.

In the case where $\mu^2 > 0$ the minimum is unique and has the value $\mathcal{V}(\phi) = 0$.

In the case where $\mu^2 < 0$, the shape of the potential changes remarkably. It has a local unstable maximum at $\mathcal{V}(\phi) = 0$ and a circle of stable minima at $\mathcal{V}(\phi) = \sqrt{-\mu^2/\lambda} = v$, where v is called the vacuum expectation value. In this case the vacuum state has an infinite number of possible values along the circle, and so is not locally gauge invariant anymore. This situation where the vacuum state doesn't have the same symmetry properties than its Lagrangian is called spontaneous symmetry breaking.

The spontaneous symmetry breaking can then be applied to the $SU(2)_L \times U(1)_Y$ group to solve the $W^\pm$ and Z^0 bosons mass problem. This is called the Higgs mechanism [11]. The minimal choice of the Higgs mechanism is by introducing a complex $SU(2)_L$ isospin doublet:

$$\phi = \begin{pmatrix} \phi^+ \\ \phi^0 \end{pmatrix}, \text{ with } \phi_0 = \frac{1}{\sqrt{2}} \begin{pmatrix} 0 \\ v \end{pmatrix} \tag{1.15}$$

Introducing the Lagrangian:

$$\mathcal{L}_\mathcal{H} = (D_\mu\phi)^\dagger D^\mu\phi - \mu^2\phi^\dagger\phi + \lambda(\phi^\dagger\phi)^2 \tag{1.16}$$

with $D_\mu\phi = \left(\partial_\mu - igT_iW_\mu^i - ig'\frac{Y}{2}B_\mu\right)\phi$, where one recognizes a part of the electroweak Lagrangian.

The choice of $\lambda > 0$ and $\mu^2 < 0$ allow to expand ϕ around its minimum ϕ_0:

$$\phi = \frac{1}{\sqrt{2}} \begin{pmatrix} 0 \\ v + H \end{pmatrix} \tag{1.17}$$

where H is the Higgs field and represents the quantum fluctuation around the vacuum expectation value.

Using this to expand the term $(D_\mu\phi)^\dagger D^\mu\phi$ leads to:

$$(D_\mu\phi)^\dagger D^\mu\phi = \frac{1}{2}(\partial_\mu H)^2 + \frac{1}{8}g^2(v+H)^2[W_\mu^1 + iW_\mu^2]^2 + \frac{1}{8}(v+H)^2[gW_\mu^3 - g'B_\mu]^2 \quad (1.18)$$

Then using the relations 1.8 and 1.9:

$$W^\pm = \frac{1}{\sqrt{2}}(W_\mu^1 + iW_\mu^2), Z^\mu = \frac{gW_\mu^3 - g'B_\mu}{\sqrt{g^2+g'^2}}, A_\mu = \frac{gW_\mu^3 + g'B_\mu}{\sqrt{g^2+g'^2}} \quad (1.19)$$

which leads to the following mass terms for the bosons:

$$M_W = \frac{1}{2}vg, M_Z = \frac{1}{2}v\sqrt{g^2+g'^2}, M_A = 0 \quad (1.20)$$

The $W^\pm$ and Z^0 bosons have acquired a mass via the Higgs mechanism, while the photon remains massless, this is the spontaneous symmetry breaking of $SU(2)_L \times U(1)_Y$ to $U(1)_Q$. Experimentally the mass of the $W^\pm$ and Z^0 bosons have been measured to [12]:

$$M_W = 80.398 \pm 0.025\,\text{GeV}, M_Z = 91.1876 \pm 0.0021\,\text{GeV} \quad (1.21)$$

The Higgs field is also linked to a spin 0 scalar boson, called the Higgs boson.

1.3.2 Giving a mass to the Fermions

The problem of mass of the bosons is now solved, but from the experiment we know that the fermions also have a mass. In the gauge group $SU(2)_L$ there are only left-handed fermions (right-handed anti-fermions) doublet and right-handed fermions (left-handed anti-fermions) singlet. So it is not possible to add a simple mass term $m\bar{\psi}\psi = m(\bar{\psi}_L\psi_R + \bar{\psi}_R\psi_L)$ in the Lagrangian, because the Lagrangian would not be gauge invariant anymore. But we can add a gauge invariant term in the Lagrangian, which is a coupling between the fermions and the Higgs field, called the Yukawa coupling. For example for the first generation of leptons the term is:

$$\begin{aligned} \mathcal{L} &= -\tfrac{g_Y}{\sqrt{2}}\left(\bar{\Psi}_L\phi\Psi_R + \bar{\Psi}_R\phi^\dagger\Psi_L\right) \\ &= -\frac{g_Y}{\sqrt{2}}\left[(\bar{\nu}_e, \bar{e})_L \begin{pmatrix} \phi^+ \\ \phi^0 \end{pmatrix} e_R + \bar{e}_R(\phi^+, \phi_0)\begin{pmatrix} \nu_e \\ e \end{pmatrix}\right] \end{aligned} \quad (1.22)$$

where g_Y is the Yukawa coupling parameter.

Then we can expand the Higgs field around its minimum like in the boson case, and this leads to:

(a) (b)

Figure 1.3: Plots of the Higgs boson. (a) Higgs to 4 leptons in ATLAS. (b) Higgs to 2 photons in ATLAS.

$$\mathcal{L} = -m_e(\bar{e}_L e_R + \bar{e}_R e_L) - \frac{m_e}{v}(\bar{e}_L e_R + \bar{e}_R e_L)h \tag{1.23}$$

where $m_e = \frac{g_Y v}{\sqrt{2}}$. The first term of equation 1.23 is the mass term of an electron of mass m_e. The second term in 1.23 is the Yukawa coupling of the electron with the Higgs boson h, which is proportional to the mass of the fermion. This relation between m_f and g_Y^f is found for all the fermions, and can be a test of the Standard Model if we can measure both, and check the consistency of the measure with the theory.

1.3.3 Discovery of the Higgs Boson

The Higgs boson has long remained the last *Terra Incognita* of the Standard Model. But on July 4^{th} 2012, the two main experiments of the LHC, ATLAS and CMS, have announced a 5σ observation of a new Higgs-like boson in both of the detectors (see Figure 1.3).

ATLAS found a Higgs-like boson mass of 126.0 ± 0.4(stat.)± 0.4(syst.) GeV [13], and CMS of 125.3 ± 0.4(stat.) $\pm$ 0.5(syst.) GeV [14]. This discovery of a low mass Higgs-like boson is a great success of the Standard Model but further studies, like the spin and the couplings, still have to be done to check if this is the Standard Model Higgs boson. ATLAS started to look at these properties [15] and the data provided evidence for the spin-0 nature of the Higgs boson, with positive parity being strongly preferred, giving more and more arguments to the Higgs nature of this new boson.

1.4 The Top Quark

By 1977 there were a strong evidence for 6 leptons, classified into 3 generations:

$$\begin{pmatrix} e \\ \nu_e \end{pmatrix}, \begin{pmatrix} \mu \\ \nu_\mu \end{pmatrix}, \begin{pmatrix} \tau \\ \nu_\tau \end{pmatrix}, \tag{1.24}$$

because,even if the ν_τ was discovered in 2000 at Fermilab [16], its existence was implied by the discovery of the τ lepton [17] and by the conservation of the lepton number. But with these 6 leptons, only 5 quarks were known:

$$\begin{pmatrix} u \\ d \end{pmatrix}, \begin{pmatrix} c \\ s \end{pmatrix}, \begin{pmatrix} \\ b \end{pmatrix}, \tag{1.25}$$

so, like for the c quark some years before, a new quark, the top quark, was postulated to restore the lepton-quark symmetry [18]. This symmetry is needed to keep the theory renormalisable at higher order corrections, and to have CP violation which needed a third generation. This new quark, with a mass predicted to be $m_t = 170 \pm 30\,\text{GeV}$ was finally discovered at Fermilab in 1995 with a mass $m_t \approx 180\,\text{GeV}$ [19][20], which is another great success of the Standard Model. Today the best estimation of the top mass is $m_t = 173.07 \pm 0.52(\text{stat.}) \pm 0.72(\text{syst.})\,\text{GeV}$ [12].

1.4.1 Properties of the top quark

Some of the properties of the top quark are different from the ones of the other quarks, mainly because of its mass. While the u quark, the lightest one, has a mass of approximately 0.35 GeV, and the b quark, the second highest, a mass around 4.5 GeV, the top quark mass is 40 times higher, of the order of a gold atom.

In particular the top quark is much heavier than the $W^\pm$ bosons and so can decay via weak interaction by the process:

$$t \to q + W^+ \text{ or } \bar{t} \to \bar{q} + W^-, \text{ with } q = \text{d,s,b.} \tag{1.26}$$

with the rates of the different decays proportional to the couplings $|g_{tq}|^2$. The couplings are extracted from the Cabibbo, Kobayashi and Maskawa matrix [21][18] or CKM matrix, which gives the allowed mixing between the quarks. A simplified version of the CKM matrix is:

$$\begin{pmatrix} V_{ud} & V_{us} & V_{ub} \\ V_{cd} & V_{cs} & V_{cb} \\ V_{td} & V_{ts} & V_{tb} \end{pmatrix} \approx \begin{pmatrix} \cos\theta_C & \sin\theta_C & 0 \\ -\sin\theta_C & \cos\theta_C & 0 \\ 0 & 0 & 1 \end{pmatrix} \tag{1.27}$$

where θ_C is the Cabibbo angle and $|g_{qq'}|^2 = |V_{qq'}|^2 g_W^2$. This immediately gives for the top quark couplings:

$$g_{td} = 0, g_{ts} = 0, g_{tb} = g_W. \tag{1.28}$$

And so the predominant decay of the top quark (99.8 % of the cases) is $t \to b + W^+$ or $\bar{t} \to \bar{b} + W^-$.

The very high mass of the top quark also implies a short lifetime. The width, Γ, of the top quark is approximately 1.5 GeV leading to a lifetime of 5×10^{-25} s. This lifetime is very short compared with that of the other quarks which is of the order of 10^{-12} s. More important the lifetime is also too short, compare to the hadronisation process, which is of the order of 10^{-23} s, for the top to form hadrons. This means that the top decays too fast to form hadrons. Therefore the decay products permit to study properties of a bare quark. An example is the preservation of spin properties.

1.4.2 Electroweak couplings of the top quark

The electroweak couplings of the top quark are the V-A couplings to the bosons Z^0 and γ at the $t\bar{t}X$ vertex, where $X = Z^0, \gamma$. The current at the $t\bar{t}X$ vertex can be written [22]:

$$\Gamma_\mu^{t\bar{t}X}(k^2, q, \bar{q}) = ie \left\{ \gamma_\mu \left(\tilde{F}_{1V}^X(k^2) + \gamma_5 \tilde{F}_{1A}^X(k^2) \right) + \frac{(q-\bar{q})_\mu}{2m_t} \left(\tilde{F}_{2V}^X(k^2) + \gamma_5 \tilde{F}_{2A}^X(k^2) \right) \right\} \tag{1.29}$$

with k^2 the four momentum of the exchanged boson, q and $\bar{q}$ the four vectors of the t and $\bar{t}$. The Gordon composition of the current gives:

$$\Gamma_\mu^{t\bar{t}X}(k^2, q, \bar{q}) = ie \left\{ \gamma_\mu \left(F_{1V}^X(k^2) + \gamma_5 F_{1A}^X(k^2) \right) + \frac{\sigma_{\mu\nu}}{2m_t} (q-\bar{q})^\mu \left(i F_{2V}^X(k^2) + \gamma_5 F_{2A}^X(k^2) \right) \right\} \tag{1.30}$$

where $\sigma_{\mu\nu} = \frac{i}{2}(\gamma_\mu\gamma_\nu - \gamma_\nu\gamma_\mu)$ and the relations between the couplings, or form factors $\tilde{F}_i^X$ and F_i^X are:

$$\tilde{F}_{1V}^X = -(F_{1V}^X + F_{2V}^X), \tilde{F}_{2V}^X = F_{2V}^X, \tilde{F}_{1A}^X = -F_{1A}^X, \tilde{F}_{2A}^X = -iF_{2A}^X. \tag{1.31}$$

Finally in the Standard Model the form factors F_i^X have the following values:

$$\begin{aligned} F_{1V}^{\gamma,SM} &= -\tfrac{2}{3} \quad ; \quad F_{1A}^{\gamma,SM} = 0 \\ F_{1V}^{Z,SM} &= \tfrac{1}{4\cos\theta_W \sin\theta_W} \left(1 - \tfrac{8}{3}\sin\theta_W{}^2\right) \quad ; \quad F_{1A}^{Z,SM} = -\tfrac{1}{4\cos\theta_W \sin\theta_W} \end{aligned} \tag{1.32}$$

and F_{2V}^X and F_{2A}^X are respectively the magnetic and electric dipole moment form factors. Note that if the F_{1V}, F_{1A} and F_{2V} are Charge and Parity symmetry, CP, conserving form factors, F_{2A} violates CP.

Thanks to the γ/Z^0 interference a e^+e^- collider can fix the sign of the form factors, whereas at the LHC the top quark couples either to the photon or to the Z^0. In that case the cross section of γ and Z^0 are separated and are mainly proportional to, for example, $(F_{1V}^Z)^2 + (F_{1A}^Z)^2$. So the precision expected at the LHC cannot exclude a sign flip of neither F_{1V}^Z nor of F_{1A}^Z.

1.5 Open Questions in Particle Physics

The Standard Model is a complete theory describing the interactions between today known elementary particles up to a scale of about 1 TeV. It is consistent culminated in major discoveries such as the weak neutral current, the charm and the top quark and most recently the Higgs boson. It has been tested to high precision at machines like PETRA,HERA,LEP and the TEVATRON and since 2008 at the LHC. The observed quantities are subject to a fit that assumes the Standard Model as the underlying theory. In this context no deviation larger than 2.5σ has been found so far. A summary of the electroweak precision measurements after the Higgs discovery is shown in Figure 1.4 and confirmed that there is no deviation higher than 2.5σ between the measurement and the Standard Model prediction [23].

Despite this success, the Standard Model also leaves some unanswered questions:

- The electroweak spontaneous symmetry breaking is an elegant way to give mass to the bosons and fermions, but the reason of this remains unknown. Concerning the Higgs mechanism another problem, called the hierarchy problem, comes from the fact that the Higgs boson is a scalar boson. Assuming that the Standard Model is only valid up to some scale, the Planck scale, leads to correction to the Higgs mass much higher than the Higgs mass itself. This implies that the mass has to be fine-tuned, up to ≈ 16 digits, to arrange this quantum corrections.
- The hierarchy of the fermions masses is another mystery. We have already pointed out that the mass of the top quark is much higher than the one of the others quarks, and this is even more dramatic if we compare to the masses of the leptons. The mass range of all the fermions runs on 11 orders of magnitude, without explanation. Some theory, like Little Higgs [24] permit to solve both the hierarchy problem and the fermions mass scale.
- The baryon anti-baryon asymmetry and the three fermion generations, are also problems. Both are well observed phenomena, we are all made of matter

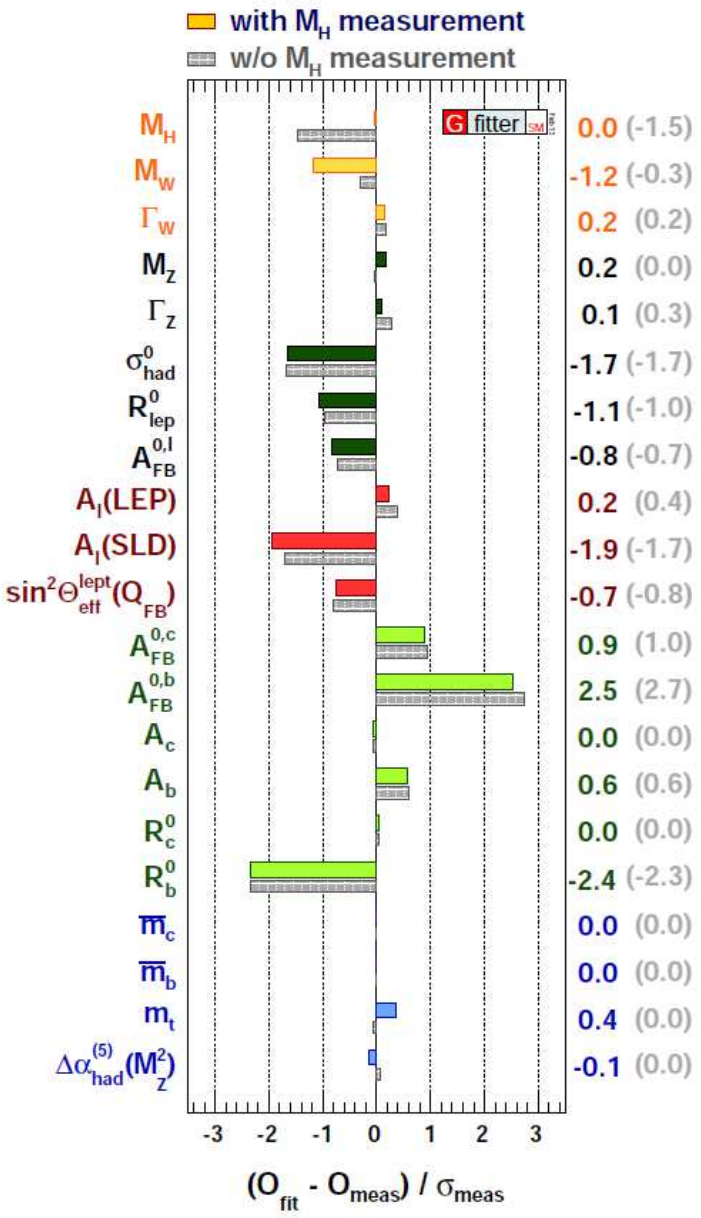

Figure 1.4: Differences between the Standard Model prediction and the measured parameter in units of the G-fitter uncertainty. Plot extract from [23]

for the first one, and in the width of the Z^0 boson for the second, but doesn't have an explanation in the Standard Model.

- The Standard Model includes three of the four fundamental forces, it doesn't manage to include the gravitation theory so far. This is justified at the typical mass scale of the electroweak theory around 100 GeV, where the gravitational effects can be neglected. However at the Plank scale around 10^{19} GeV, the gravity can't be ignored anymore and should be unified to the theory.
- Another aspect of astrophysics which have no answer in the Standard Model is the observation of dark matter. If the visible matter accounts only for around 5 % of the total mass of the universe, the dark matter represents around 27 % of this total [25]. The Standard Model doesn't contain an explanation for these weakly interacting particles.

The role of the accelerators, and in particular of the ILC, is to give answers to these questions, or at least some clues in order to know in which direction one should search.

Chapter 2

The International Linear Collider

2.1 Presentation and Motivation of the ILC

Since the beginning of the accelerator era in particle physics there has been a good complementarity between hadronic and leptonic colliders. The first ones are powerful tools to make discovery, as for example the ones of the W and Z bosons, or the discovery of the top quark at the Tevatron in 1995. The second ones on the other hand are rather used to make precision measurement like the mass measurement of the bosons W and Z at LEP (Large Electron Positron) and SLC (Stanford Linear Collider). Today the great hadronic machine is the LHC (Large Hadron Collider) which is already a success due to the discovery of the Higgs boson in 2012, and to continue this good complementarity we only miss a new leptonic machine.

The other important characteristic is that we need a linear machine. With a circular one the maximal energy is roughly define by the diameter of the machine, and its parameters are usually tuned for this energy. On the opposite at a linear collider it is possible to run with different energies. In addition it also facilitates if needed an upgrade of the accelerator to go beyond the nominal maximum beam energy by simply adding new accelerating cavities to the accelerator. This allows for having a complete physics program at different energy like shown in the Table 2.1.

A Linear electron-positron Collider of up to at least 500 GeV should be the next major project of particle physics. There are two proposals for the linear collider: the ILC (International Linear Collider) and CLIC (Compact Linear Collider) [26] with up to 3 TeV center of mass energy. The ILC, the more advanced project, is an international project for an e^+e^- linear collider with up to 1 TeV center of mass energy. This facility has concluded its technical design phase and could go for construction if approved [27]. The footprint of the accelerator has a length of about 31 Km. The acceleration will be made by 16,000 superconducting radio-

frequency accelerating cavities. The ILC should be a complement to the LHC of CERN in Geneva. Indeed, unlike the LHC where the collisions are between protons, which are composite particles, the electrons and positrons are point-like particles. This has many advantages, as the knowledge of the initial state. In the case of the proton, the energy is shared between its different components. In the case of the electron the energy is concentrated in the point-like particles. Also at an e^+e^- collider the ratio between the different production rates are much smaller. This leads to the fact that, even if the cross section are smaller at the ILC than at the LHC, the proportion of rare events is higher. For example we have one Higgs event every one billion pp collisions at the LHC, where one will have 1 % of Higgs events at the ILC. All this leads to much easier physics analysis, because cleaner environment makes easier to separate signal from background. The other effect is that you don't need trigger at the ILC, all the bunch crossing events will be stored, where at the LHC you keep only one over 10^6 events.

The ILC will provide polarized beam, both for electron beam and for positron beam. This will give the possibility to physics analysis, to study the processes for each initial and final polarization state. This is an important fact in the electroweak theory framework, where the V-A structure leads to different possible processes and effects for left-handed and right-handed particles (see section 1.2.2). This is important for top quark, W and Z bosons decay which are spin dependent. This spin effect is a powerful test of the Standard Model. Then polarization also has the advantage for some processes to change the cross section, which becomes different for $e^+_L e^-_R$ and for $e^+_R e^-_L$. The physics program can use this effect to enhance the cross section of the process one is interested in, and to reduce the background.

According to the Standard Model of particle physics, spontaneous symmetry breaking in combination with the Higgs mechanism gives rise to massive vector bosons and a massive scalar boson, called the Higgs boson. For studying this electroweak symmetry breaking one of the important reactions of the ILC is therefore the Higgs-strahlung $e^+e^- \to Z^* \to HZ^0$, where one Z^0 boson is created in association to a Higgs boson. This reaction could help to measure the Higgs mass and its quantum numbers in a model independent way. The mass of the Higgs-like boson discovered at the LHC is around 125 GeV and is well within the energy range of 0.1 Gev to 1 TeV of the ILC.

The main scientific goal of the ILC is to study in detail the Higgs boson with a better precision than the LHC as explained above. This will permit to measure with a good precision the mass, width, and the couplings of the Higgs. The second important goal of the ILC is to study the top quark, the quark with a mass much higher than the one of the others quarks. This higher mass and so, by construction of the Standard Model, higher coupling with the Higgs boson can be a good probe for new physics. Finally the ILC will also try to look elsewhere than in the Standard

Energy	Reaction	Physics Goal
91 GeV	$e^+e^- \to Z$	ultra-precision electroweak
160 GeV	$e^+e^- \to WW$	ultra-precision W mass
250 GeV	$e^+e^- \to Zh$	precision Higgs couplings
350-400 GeV	$e^+e^- \to t\bar{t}$	top quark mass and couplings
	$e^+e^- \to WW$	precision W couplings
	$e^+e^- \to \nu\bar{\nu}h$	precision Higgs couplings
500 GeV	$e^+e^- \to f\bar{f}$	precision search for $Z^{'}$
	$e^+e^- \to t\bar{t}h$	Higgs coupling to top
	$e^+e^- \to Zhh$	Higgs self-couplings
	$e^+e^- \to \tilde{\chi}\tilde{\chi}$	search for supersymmetry
	$e^+e^- \to AH, H^+H^-$	search for extended Higgs states
700-1000 GeV	$e^+e^- \to \nu\bar{\nu}hh$	Higgs self-couplings
	$e^+e^- \to \nu\bar{\nu}VV$	composite Higgs sector
	$e^+e^- \to \nu\bar{\nu}t\bar{t}$	composite Higgs and top
	$e^+e^- \to \tilde{t}\tilde{t}^*$	search for supersymmetry

Table 2.1: Main physics processes of the ILC for different energies. Table extracts from the Technical Design Report [28].

Model, to try to point out the problems of this one, in order to find new physics beyond the standard model and the scale of this new physics.

2.2 Physics at the International Linear Collider

The Standard Model had a lot of success in the last years, the last one with the Higgs-like boson discovery at the LHC around 125 GeV, but it is admitted that it is incomplete (see section 1.5). That is why we need a precision machine in order to test with a very high precision the Standard Model and try to find where it fails. The Table 2.1 shows a list of the main physics processes that will be studied at the ILC. The energy in the table is the minimal energy from which the reaction could be studied.

The first physics goal of the ILC will be to study in detail the new Higgs-like particle discover at LHC with a mass of 125 GeV. The first step will be to study the reaction $e^+e^- \to Zh$ at a center of mass energy of 250 GeV. With this reaction, the distribution of the invariant recoil mass against the reconstructed Z boson, gives a measurement of the Higgs mass independently of the Higgs decay mode, and in a model independent way. But it is also possible to measure the rate of all the Higgs decay mode, even the invisible ones, with a high precision. At higher

energies it will also be possible to measure the Higgs self-couplings and the top Yukawa coupling.

Another important aspect of the ILC physics program is the study of the top quark. As the heaviest particle of the standard model it has the higher coupling with the Higgs boson. The $\bar{t}t$ measurement at threshold will give precise measurement of the top quark mass and width. At higher energies a precise measurement of the top quark couplings should be a probe for new physics beyond the standard model.

Finally the ILC will also look for new particles, like the ones predicted by supersymmetry or other models. These new particles, difficult to identify at the LHC, might be an answer for the dark matter question.

Table 2.2 presents a list of measurements that could be carried out at the ILC and their expected precision for each one. Note that corresponding results for the top quark electroweak couplings will be elaborated in this thesis.

2.3 The Accelerator

The International Linear Collider (ILC) is a linear accelerator in contrast to circular machine like was LEP at CERN. The centripetal force in a circular machine provokes an energy loss of the electrons known as Synchrotron radiation. The energy loss in each turn by an accelerated particle with a mass m and an energy E is proportional to:

$$\Delta E \propto \frac{E^4}{rm^4} \tag{2.1}$$

where r is the radius of the accelerator. This shows that the energy loss is a limitation of a circular accelerator where the maximal practical energy is limited by this radiation, so by its radius, from which the radiation is proportional. At the energy range of the ILC this is especially true for particles with a low mass, like electrons, as the energy loss is inversely proportional to the 4th power of the particle's mass. So the ILC was chosen to be linear mainly in order to limit the synchrotron radiation and to be upgradeable in energy, which is not possible in a circular accelerator where one face the wall of the radius.

The ILC is an accelerator based on the superconducting radio-frequency accelerating technology. This cold technology uses 1.3 GHz superconducting niobium nine cells accelerating cavities in the main linac for a center of mass energy range of 200 to 500 GeV upgradeable to 1 TeV. The footprint of the ILC has a length of about 31 km, and a single interaction point where two detectors can be placed alternately in a so-called "push-pull" configuration. The two detector concepts are the Silicon Detector, SiD [29], and the International Large Detector, ILD [30].

Topic	Parameter	Accuracy $\Delta X/X$	
Higgs	m_h	0.03 %	$\Delta m_h = 35\,\text{MeV}$, 250 GeV
	Γ_h	1.6 %	250 GeV and 500 GeV
	$g(hWW)$	0.24 %	
	$g(hZZ)$	0.30 %	
	$g(hb\bar{b})$	0.94 %	
	$g(hc\bar{c})$	2.5 %	
	$g(hgg)$	2.0 %	
	$g(h\tau^+\tau^-)$	1.9 %	
	$BR(h \to invis.)$	< 0.30 % (95 % conf.)	
	$g(ht\bar{t})$	3.7 %	1000 GeV
	$g(hhh)$	26 %	
	$g(h\mu^+\mu^-)$	16 %	
Top	m_t	0.02 %	$\Delta m_t = 34\,\text{MeV}$, threshold scan
	Γ_t	2.4 %	
W	m_W	0.004 %	$\Delta m_W = 3\,\text{MeV}$, threshold scan
	g_1	0.16 %	500 GeV
	κ_γ	0.03 %	
	κ_Z	0.03 %	
	λ_γ	0.06 %	
	λ_Z	0.07 %	
H^0, A^0	m_H, m_A	1.5 %	
	$\tan\beta$	20 %	
$\tilde{\chi}^+$	$m(\tilde{\chi}^+)$	1 %	
	$m(\tilde{\chi}^0)$	1 %	
$\tilde{t}$	$m(\tilde{t})$	1 %	
	$\cos\theta_t$	0.4 %	

Table 2.2: Main physics quantities that can be measured at the ILC with their expected precision. Table extracts from the Technical Design Report [28].

The different parts of the accelerator are shown in Figure 2.1. The summary table of the machine parameters, presented in Table 2.3, is extracted from the Technical Design Report [28]. This table contains the numbers for different working center of mass energies of the baseline 500 GeV machine. The parameters are also presented for a so-called 1st stage machine version, where the length of the main linac is half the one of the baseline. Finally luminosity and energy upgrade parameters are shown.

The main parts of the accelerator are:

– the polarized electron source.
– the polarized positron source.
– the damping rings.
– the main linac.
– the beam delivery system.

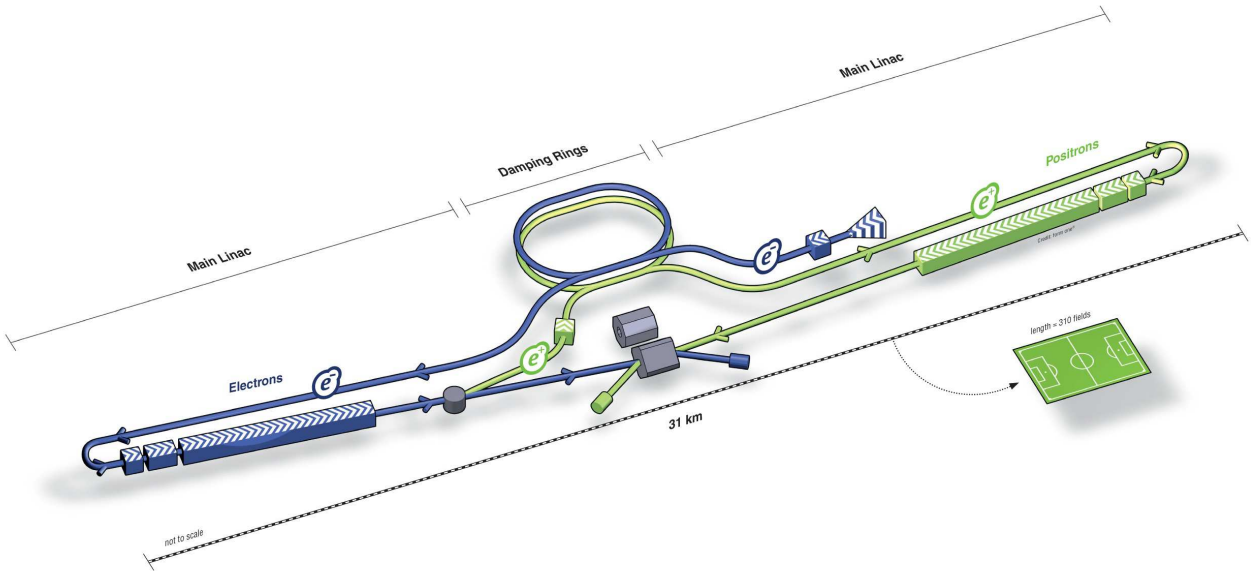

Figure 2.1: Schematic view of the ILC.

			Baseline 500 GeV Machine			1st Stage	$\mathcal{L}$ Upgrade	E_{CM} Upgrade
Center-of-mass energy	E_{CM}	GeV	250	350	500	250	500	1000
Collision rate	f_{rep}	Hz	5	5	5	5	5	4
Electron linac rate	f_{linac}	Hz	10	5	5	10	5	4
Number of bunches	n_b		1312	1312	1312	1312	2625	2450
Bunch population	N	$\times 10^{10}$	2	2	2	2	2	1.74
Bunch separation	Δt_b	ns	554	554	554	554	366	366
Pulse current	I_{beam}	mA	5.8	5.8	5.8	5.8	8.8	7.6
Main linac average gradient	G_{a}	MV.m^{-1}	14.7	21.4	31.5	31.5	31.5	38.2
Average total beam power	P_{beam}	MW	5.9	7.3	10.5	5.9	21.0	27.2
Estimated AC power	P_{AC}	MW	122	121	163	129	204	300
RMS bunch length	σ_{z}	mm	0.3	0.3	0.3	0.3	0.3	0.250
Electron RMS energy spread	$\Delta p/p$	%	0.190	0.158	0.124	0.190	0.124	0.083
Positron RMS energy spread	$\Delta p/p$	%	0.152	0.100	0.070	0.152	0.070	0.043
Electron polarization	P_-	%	80	80	80	80	80	80
Positron polarization	P_+	%	30	30	30	30	30	20
Horizontal emittance	$\gamma\epsilon_x$	μm	10	10	10	10	10	10
Vertical emittance	$\gamma\epsilon_y$	nm	35	35	35	35	35	30
IP RMS horizontal beam size	$\sigma_{\text{x}}*$	nm	729	683.5	474	729	474	481
IP RMS vertical beam size	$\sigma_{\text{y}}*$	nm	7.7	5.9	5.9	7.7	5.9	2.8
Luminosity	$\mathcal{L}$	$\times 10^{34}\, cm^{-2}s^{-1}$	0.75	1	1.8	0.75	3.6	3.6
Fraction of luminosity in top 1%	$\mathcal{L}_{0.01}/\mathcal{L}$	%	87.1	77.4	58.3	87.1	58.3	59.2
Average energy loss	δ_{BS}	%	0.97	1.9	4.5	0.97	4.5	5.6
Number of pairs per bunch crossing	N_{pairs}	$\times 10^3$	62.4	93.6	139.0	62.4	139.0	200.5
Total pair energy per bunch crossing	E_{pairs}	TeV	46.5	115.0	344.1	46.4	344.1	1338.0

Table 2.3: Parameters of the ILC, at the time of the Technical Design Report [28].

2.3.1 The Electron Source

The polarized electron production starts out from a photocathode DC gun. A laser is sent on a strained superlattice GaAs cathode which creates a bunch of electrons with 90 % polarization. The beam is then accelerated to 5 GeV and injected into the electron damping ring.

2.3.2 The Positron Source

After passing through the main linac the electron beam passes inside a superconducting helical undulator that creates circularly polarized photons with up to 30 MeV. The photons are then sent to a rotating Ti-alloy target to create e^+e^- pairs that inherit the polarisation of the photons [31]. The positrons are then separated from the electrons and the remaining photons. The positron beam is finally accelerated to 5 GeV and injected into the positron damping ring. This method provides a polarization of at least 30 % for the positron beam. More details on the ILC positron source are shown in Figure 2.2.

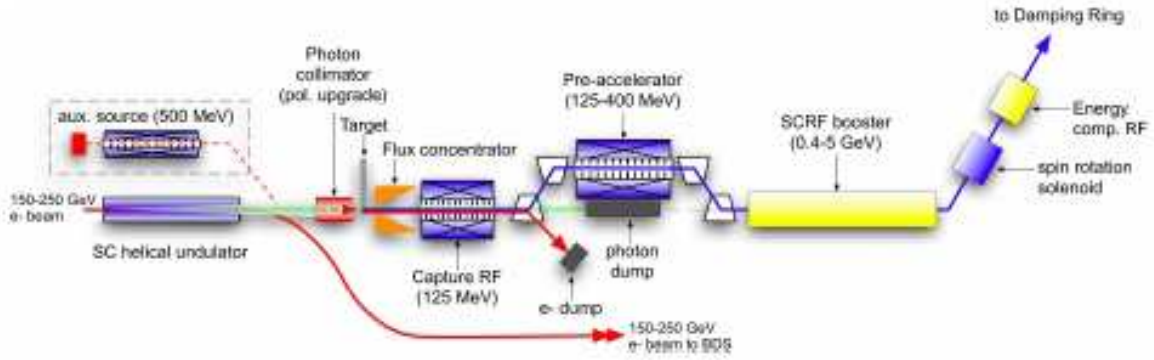

Figure 2.2: Layout of the positron source.

2.3.3 The Damping Rings

Two damping rings, one for the electron and one for the positron, operating at a beam energy of 5 GeV, and with a circumference of 3.2 km each, are foreseen in the baseline design. The damping rings cool the emittance of the incoming beam to the low level required for the high luminosity of the ILC. The damping rings should also store stable bunch trains within the 200 ms between machine pulse.

After the extraction from the damping rings, the two beams are transferred to the main linac part of the accelerator via the ring to main linac. The ring to main linac has many functions, transport the beam for about 15 km at 5 GeV, prepare

the beam for betatron and energy collimation and stabilization, use spin rotators to orient the beam to the desired longitudinal polarization and accelerate it to 15 GeV, before the beam enters the main linac.

These two parts of the accelerator are the most important, with the beam delivery system, to prepare the beam in terms of emittance, beam shape, and energy spread which is very important to reach the high luminosity goals.

2.3.4 The Main Linac

The two main linac are 11 km long and accelerate beams from 15 GeV, at the end of the ring to main linac, to a maximum energy of 250 GeV at the entrance of the beam delivery system. One linac consist of approximately 7400 1.3 GHz superconducting nine-cell niobium cavities (see Figure 2.3) operating at 2 K. The average accelerating gradient of the cavities is 31.5 MV/m, with a tolerated gradient spread between the cavities of $\pm$ 20 %, and a quality factor $Q_0 \geq 10^{10}$. Each cavity is equipped with a high-power input coupler to transfer the RF-power from the waveguide system into the cavity.

The cavities are assembled into two types of cryomodules, of 12.65 m long (see Figure 2.4). The $\approx$ 850 cryomodules are separated between Type A module consisting of 9 1.3 GHz superconducting nine-cell niobium cavities, and every third cryomodule, a Type B module where the central cavity is replaced by one superconducting quadrupole package.

2.3.5 The Beam Delivery System

The two beam delivery systems (BDS) are 2.2 km long and they transfer the beams from the end of the main linac to the interaction point (IP). Within the BDS the beams are focused to a few nm (see Table 2.3 for details), the size required to reach the luminosity goals. The tests carried out at the ATF2 facility at KEK currently achieve a 55 nm vertical beam size with a low energy beam. Finally they are brought into collision with a 14 mrad crossing angle. Linear collider also imposes that a bunch train can be used only once, so the BDS should also transport the beams to the main beam dumps.

The BDS has also other tasks like characterize the beams (energy, polarization, ...) before and after the IP, and also remove the beam halo in order to minimize the beam background in the detectors.

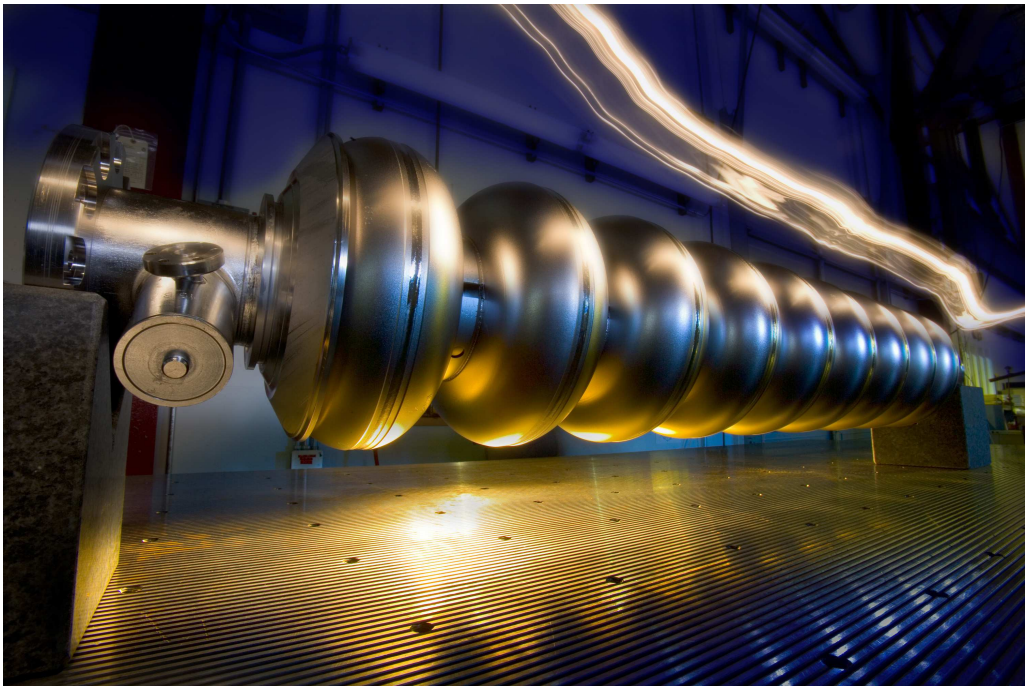

Figure 2.3: ILC superconducting RF cavity.

Figure 2.4: ILC cryomodule.

Chapter 3

The International Large Detector

3.1 Presentation of the ILD

The ILC is designed for two detectors at the interaction point, the Silicon Detector, SiD a compact, cost-constrained detector made possible with a 5 Tesla magnetic field and silicon tracking [29], and the International Large Detector, ILD [30]. The ILD is a classical multi-purpose 4π detector, composed of several subsystems ordered as layers around the interaction point. To meet the physics goals of the ILC, the ILD has been optimized for the application of the Particle Flow Algorithm, PFA. Table 3.1 is a summary of the ILC physics requirements. The schematic drawing of the detector is shown in Figure 3.1. A description of each system, as in the baseline simulation, ordered by the distance from the beam collision point, is given in the following:

- A multi-layer pixel-vertex detector (VTX). The VTX, which enables the measurement of the position of charge particles, is optimized for excellent point resolution and minimum material thickness.
- A large volume time projection chamber (TPC) with up to 224 points per track. The TPC, which measures the position of charged particles, is optimized for 3-dimensional point resolution and minimum material in the field cage and in the end-plate. It also provides dE/dx based particle identification capabilities.
- A highly segmented ECAL providing up to 30 samples in depth and small transverse cell size. It consists of interleaved layers of absorbing material (tungsten) and sensitive material (silicon). The ECAL measures photons, charged particles and neutral hadrons, which will leave a shower of secondary particles as they interact with tungsten.
- A highly segmented HCAL with up to 48 longitudinal samples and small transverse cell size. It consists of steel absorber material, and scintillator

tiles as active medium, which measures the resulting showers. The HCAL measures the energy deposited by charged and neutral hadrons.
- Other smaller calorimetric detectors use to cover 4π and measure the luminosity.
- A large volume superconducting coil surrounds the calorimeters, creating an axial B-field of nominally 3.5 Tesla. It provides the magnetic field necessary to bend the charged particles inside the detector.
- An iron yoke returns the magnetic flux of the solenoid, and at the same time, serves as a muon detector and tail catcher.
- A sophisticated data acquisition (DAQ) system which operates without an external trigger, to maximize the physics sensitivity.

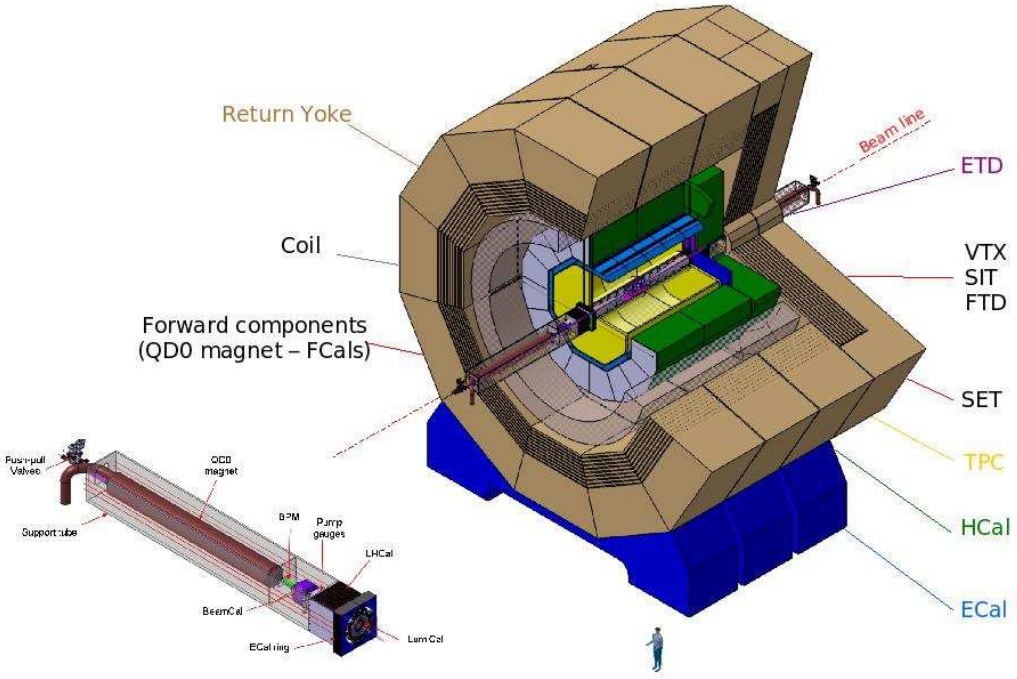

Figure 3.1: Sketch of the ILD.

Physics Process	Measured Quantity	Critical System	Physical Magnitude	Required Performance	Comments
Zhh $Zh \to q\bar{q}b\bar{b}$ $Zh \to ZWW^*$ $\nu\bar{\nu}W^+W^-$	Triple Higgs coupling Higgs mass $B(h \to WW^*)$ $\sigma(e^+e^- \to \nu\bar{\nu}W^+W^-)$	Tracker and Calorimeter	Jet Energy Resolution $\Delta E/E$	 3 % to 4 %	 2 times better than LEP
$Zh \to l^+l^-X$ $\mu^+\mu^-(\gamma)$ $Zh + h\nu\bar{\nu} \to \mu^+\mu^-X$	Higgs recoil mass Luminosity weighted E_{CM} BR($h \to \mu^+\mu^-$)	μ detector Tracker	Charged particle Momentum Resolution $\Delta p_t/p_t^2$	 $5 \times 10^{-5}\, GeV^{-1}$	 10 times better than LEP
$Zh, h \to bb, c\bar{c}, gg$	Higgs branching fractions b-quark charge asymmetry	Vertex	Impact parameter	$5\,\mu m \oplus$ $10\,\mu m/p(GeV)\sin\theta^{3/2}$	3 times better than SLD
SUSY, eg. $\tilde{\mu}$ decay	$\tilde{\mu}$ mass	Tracker Calorimeter μ detector	Momentum Resolution Hermiticity		

Table 3.1: Detector performance needed for key ILC physics measurements. Table extract from the Technical Design Report.

3.2 The Particle Flow Algorithm

The Particle Flow is a paradigm based on the observation of the particle composition in a jet [32]. About 62 % of the energy of a jet comes from charged particles, 27 % from photons, 10 % from neutral hadrons and around 1 % from neutrinos. On the other hand the momentum resolution of a tracking system is much more precise than the energy resolution of a calorimeter, up to a given energy as illustrated in Figure 3.2 [34]. Both facts lead to the conclusion that the charged particles of a jet should be measured in the tracking system, while only the neutral ones should be measured by the calorimeters. This is the particle flow algorithm philosophy, using the best suitable detector subsystem to measure a particle energy, like shown on Figure 3.3.

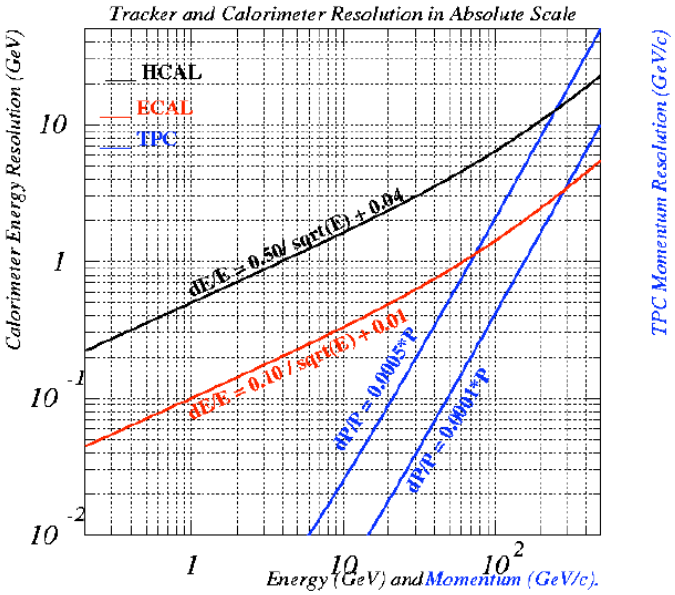

Figure 3.2: Energy and momentum resolution as provided by tracking devices (TPC) and calorimeters (ECAL, HCAL). The study presented here was performed for the TESLA detectors [33] which was similar to the ILD concepts.

The concept of PFA implies that the detector is able to separate the particles from each other. Indeed it is important that a charged particle, which is measured in the tracker system, is not counted a second time in the calorimeters, or that a neutral particle is not misidentifing as a charged one. To reduce this confusion, the detector has to be optimized in the framework of the PFA. First of all the tracking and the calorimeters have to be placed inside the coil to support best the particle separation in the calorimeters. A high separation powers of the close by showers requires in particular highly granular calorimeters. The high granularity, with a

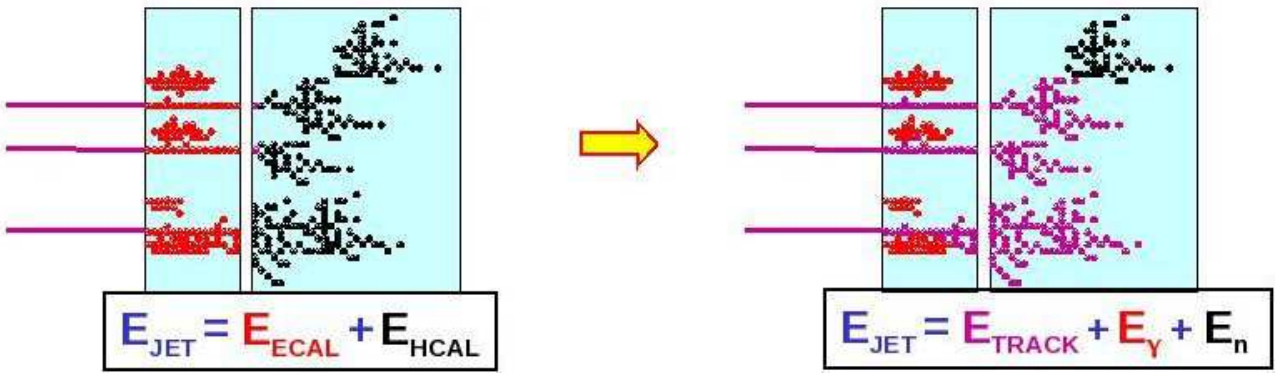

Figure 3.3: Illustration of the Particle Flow Algorithm principle.

reduce lateral size of the shower, helps to separate the charged showers, already measure in the trackers, from the neutral ones.

These requirements and the aim of resolving the jet energy to $\sigma_{E_{jet}}/E_{jet} \approx 3-4\,\%$ are the main guidelines of the ILD design. Figure 3.4 illustrated that the current jet energy resolution is within these guidelines [28].

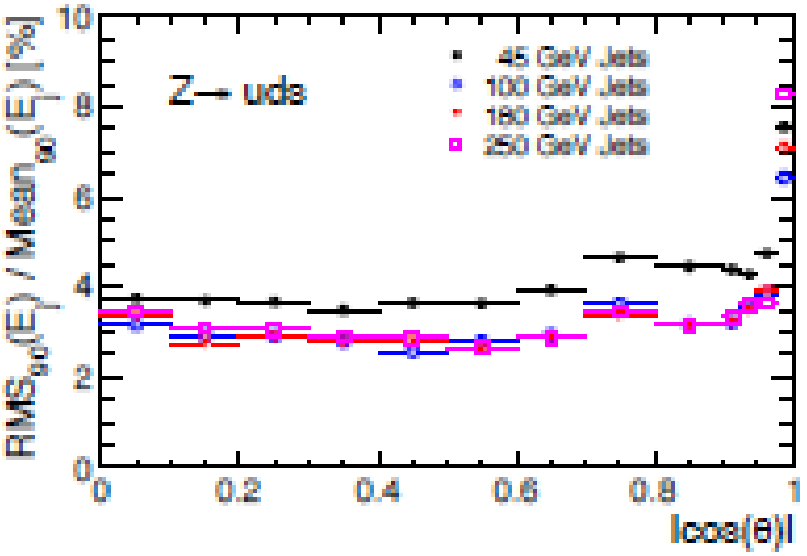

Figure 3.4: Fractional jet energy resolution plotted against $|\cos\theta|$ where θ is the thrust axis of the event.

3.3 The Tracking System of the ILD

3.3.1 The Vertex Detector

With the detection of the primary vertex the aim of the vertex detector is to identify b and c quarks and tau leptons, which is a key point in the ILC physics program. This identification is possible because the hadrons formed from the quarks, like D or B mesons, are short lived particles. These hadrons live yet long enough to have a different decay vertex displaced from the primary one. The secondary vertex of the meson decay is reconstructed thanks to the track information of its decay products. This permits in addition to reconstruct the charge of the jet linked to the vertex.

The performance of the vertex detector is expressed in terms of its impact parameter resolution, $\sigma_b < \left(5 \oplus 10/p \sin\theta^{3/2}\right)\ \mu m$. To reach this level of precision, the vertex detector must comply with the following conditions:

- A material budget below 0.15 % X_0/layer.
- A first layer as close as $\approx 1.6\,cm$ of the IP.
- A pixel occupancy not exceeding a few %.
- A power consumption low enough to minimize the material budget needed by the cooling system.

The baseline design of the ILD vertex detector is composed of three cylindrical layers, equipped on both sides with pixel sensors, and separate by ≈ 2 mm. This leads to 6 measured track positions with a radii range from 16 mm to 60 mm from the IP. A sketch of the baseline design is shown on Figure 3.5. There are currently three options for the technology of the vertex detector: the CMOS Pixel Sensors, the Fine Pixel CCD sensors, and the Depleted Field Effect Transistor sensors. All of them have the potential to meet the ILD vertex detector specifications.

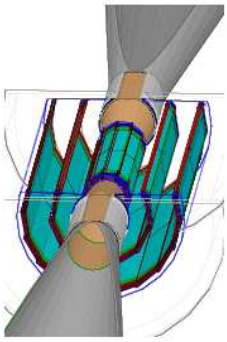

Figure 3.5: Sketch of the ILD vertex detectors.

3.3.2 The Silicon Tracking

The ILD silicon tracking system is composed of four parts: the Silicon Inner Tracker (SIT), the Silicon External Tracker (SET), one end cap component behind the end-plate of the TPC (ETD), and the forward tracker (FTD). They are all surrounding the TPC (see Figure 3.6), and act as a link between the TPC and the others detectors around. For example the SIT helps to link the TPC and the vertex detectors, improving the overall momentum resolution, while the SET helps to extrapolate the track from the TPC to the calorimeter, which is an important step of the PFA.

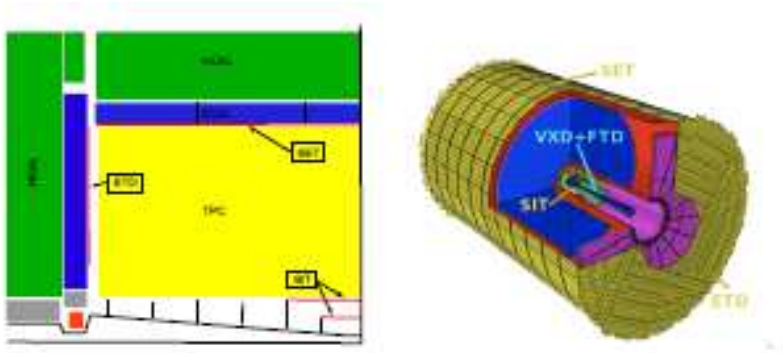

Figure 3.6: Left: a quadrant view of the ILD silicon tracking system. Right: a 3D view illustrating the position of the four components around the TPC.

The SIT, SET and ETD are made of two single-side silicon micro-strip layers, while the FTD is also made of pixel detectors to deal with higher occupancies in the forward area.

3.3.3 The Time Projection Chamber

The central tracker system of ILD is a Time Projection Chamber, TPC. It offers the possibility to have a continuous tracking, with up to 224 points per track. The TPC also has the advantage to present of low amount of material budget, which is important for the PFA performance. Finally the TPC also provides a particles identification via the dE/dx methods, which is a welcomed feature for many physics analyses.

In the baseline design of the ILD (see Figure 3.7(a)), the TPC is 4.70 m length along the beam axis, with an inner radius of 329 mm and an outer one of 1808 mm. The solid angle coverage is up to $|\cos\theta| \approx 0.98$. The TPC is immersed in a magnetic field of 3.5 T, and should achieve under this condition a point resolution

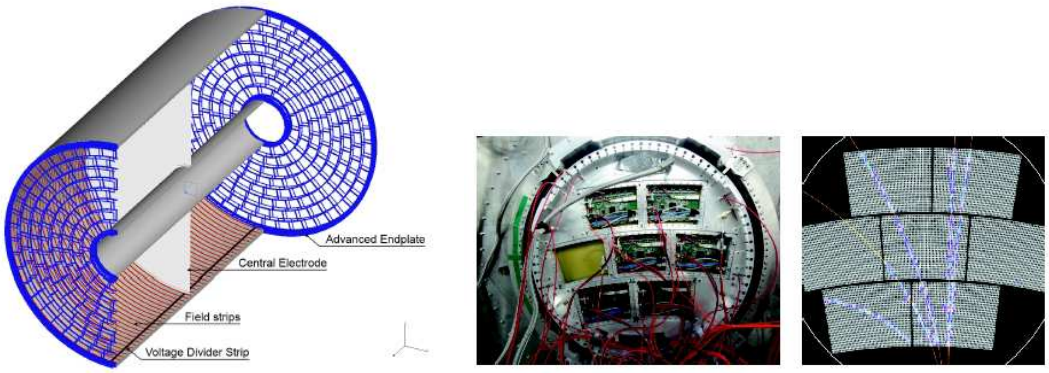

(a) (b)

Figure 3.7: (a) Sketch of the ILD TPC. (b) TPC *R&D* with micromegas.

better than 100 μm for a complete drift and a double hit resolution of less than 2 mm.

There are currently two options for the gas amplification systems, the Micromegas (see Figure 3.7(b)) and the Gas Electron Multipliers (GEM). Both options are using pads of size approximately $1 \times 6\,mm^2$ leading to 10^6 pads per end-plate.

3.4 The Calorimeter System of the ILD

3.4.1 The Electromagnetic Calorimeter

The main role of the electromagnetic calorimeter, ECAL, in the framework of the PFA is to measure the properties of the electrons and the photons. As explained in Section 3.2 this leads to constraints on the ECAL design. First, as the ECAL has to be placed inside the magnetic field, it has to be as compact as possible in order to limit the size of the overall detectors. Also it has to clearly separate the close by showers, and to have a tracking capability, to identify neutral and charged ones and to link the charged ones with their tracks in the TPC. This implies to have a high granularity and an absorber material with a small Molière radius.

The current baseline design of the ILD ECAL has a barrel and an end-cap structure. It has 30 readout layers with $24X_0$ as thickness, but the details of the design are under optimization.

The Silicon Tungsten Electromagnetic Calorimeter, SiW-ECAL, is one of the technological options for the ILD ECAL. The choice of the Tungsten as absorber

material is guided by the PFA performance:

- $R_M = 9\,\text{mm}$: a small Molière radius to better separate close-by showers.
- $X_0 = 3.6\,\text{mm}$: a small radiation length to make the ECAL as compact as $24X_0$ within 20 cm.
- $\lambda_l/X_0 = 27.5$: a large interaction length over radiation length ratio to clearly distinguish electromagnetic showers from hadronic ones. One should notice that about half of the hadronic showers start inside the ECAL.

The choice of the Silicon as active material is driven by the ease of pixelisation needed for the granularity of the ECAL. For a pad size of $5 \times 5\,mm^2$, the silicon pin diodes are easy to produce and offers good performances in the detector environment. The silicon is also a stable material, which leads to an easier calibration (more stable and no temperature dependence). An alternative option is based on scintillator strips as active material.

More details about the SiW-ECAL *R&D* will be given in Part II.

3.4.2 The Hadronic Calorimeter

The role of the hadronic calorimeter, HCAL, in the framework of the PFA, is mainly to measure the properties of the neutral hadrons. The HCAL should have a fine longitudinal sampling while keeping the detector volume low. This is possible by using steel as absorber material. Its ratio interaction length, $\lambda_l = 17\,\text{cm}$, over radiation length, $X_0 = 1.8\,\text{cm}$, keeps the shower reasonable and allows a good longitudinal sampling in the baseline design of 48 layers. As for the ECAL, the HCAL will have a barrel and an end-cap structure, and the rigidity of the steel allows for fabricating a self-supporting structure, reducing by this way the uninstrumented zones.

For the active material, two options are considered. First a scintillator-tile based Analog HCAL, using silicon photo-diodes, SiPMs, with cells of $3 \times 3\,cm^2$ (see Figure 3.8(a)). Second a Glass Resistive Plate Chamber, GRPC, Semi-Digital HCAL, with cells of $1 \times 1\,cm^2$ (see Figure 3.8(b)).

The calorimeter system of the ILD is completed at very forward angles by some others calorimeters (LumiCAL, BeamCAL, LHCAL). These calorimeters have specific properties like radiation hardness, and are here to extend the solid-angle coverage to almost 4π, and to perform specific tasks like the luminosity measurement.

3.5 The Outer Part of the ILD

The outer part of the ILD consists of a superconducting coil surrounding the calorimeters and of an iron yoke which also serve as muon detector.

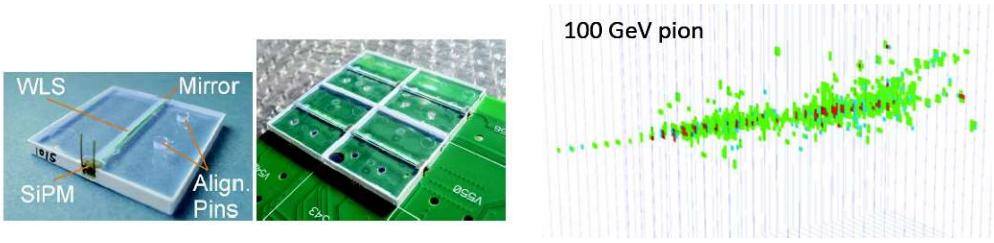

(a) (b)

Figure 3.8: (a) AHCAL scintillator-tiles with embedded SiPMs. (b) Shower left by a 100 GeV pion in the SDHCAL prototype.

The magnet of the ILD consists of a superconducting solenoid coil creating a magnetic field of 3.5 T. The overall size of the magnet is 6.88 m in diameter and 7.35 m in length. An iron yoke is also needed to return the flux of the solenoidal field and to keep the outside field low. The iron yoke will be the main mechanical structure of the ILD, and will also be used as absorber material for the muon detector.

The muon detector takes place outside of the solenoid coil and gives additional measurement to the trackers and the calorimeters to identify muons. It will also be used as a tail catcher to recover the energy which is leaking out of the HCAL. The two main options for the active material of the several layers of the muon system are scintillator strips read out with SiPMs and Resistive Plate Chambers, RPC.

Part II

The Silicon-Tungsten Electromagnetic Calorimeter

In this part of the thesis I will present the $R\&D$ of the Silicon Tungsten Electromagnetic Calorimeter of the ILD, the SiW-ECAL.

In Chapter 4 I will present the results obtained by the physics prototype of the SiW-ECAL. The goal of this prototype was to demonstrate the principle of a compact highly granular calorimeter. In Chapter 5 I will present the first results obtain with the technological prototype of the SiW-ECAL. The goal here was the study the engineering challenges of such a detector, and in particular the ones related to the electronics of the detector.

Chapter 4

The Physics Prototype of the SiW-ECAL

4.1 Presentation

The SiW-ECAL, as introduced in Section 3.4.1, is a highly granular calorimeter optimized for the PFA. The CALICE (CAlorimeter for a LInear Collider Experiment) collaboration [35] is driving the $R\&D$ for such a PFA calorimeter. In a first phase CALICE has built a physics prototype of the SiW-ECAL, to demonstrate the proof-of-principle of such a calorimeter.

In order to have a calorimeter that meets the PFA goals the choice has been made to use Silicon as active material and Tungsten as absorber material. Tungsten has the following properties, a radiation length $X_0 = 3.5\,\text{mm}$, a small Molière radius $R_M = 9\,\text{mm}$ and hadronic interaction length $\lambda_I = 96\,\text{mm}$. This leads to a very dense and compact calorimeter, but with an unprecedented amount of readout channels for such a prototype. Being able to operate and calibrate with efficiency is part of the challenge of the physics prototype.

The physics prototype has been operated in beam tests, at DESY, CERN, and at FNAL in different campaigns between 2006 and 2011, with low energy electrons and hadrons beam. The main purpose of these beam tests was to measure physics observables like the energy and angular resolution to validate the detector simulation used in the physics studies.

4.2 Design of the SiW-ECAL Physics Prototype

The SiW-ECAL prototype [36] is a compact and high granularity sampling calorimeter with tungsten as absorber and silicon with a pixel size of $1 \times 1\,\text{cm}^2$ as sensitive detector (see Figure 4.1). To contain high energy electromagnetic

showers, the longitudinal total thickness of the prototype is about $24X_0$ (20 cm). This ensures the containment of 99.5 % of a 5 GeV electron shower and more than 98 % of a 50 GeV one. Totally 30 layers are chosen to assure a high degree of longitudinal granularity. Three different absorber thicknesses are used for the layers:

- 10 layers of $0.4X_0$ (1.4 mm).
- 10 layers of $0.8X_0$ (2.8 mm).
- 10 layers of $1.2X_0$ (4.2 mm).

Each silicon layer has an active area of $18 \times 18\,\mathrm{cm}^2$, segmented into modules of 6×6 readout pads of $1 \times 1\,\mathrm{cm}^2$ each. The active volume of the physics prototype therefore consists of 30 layers of 3×3 modules, giving in total 9720 channels [36].

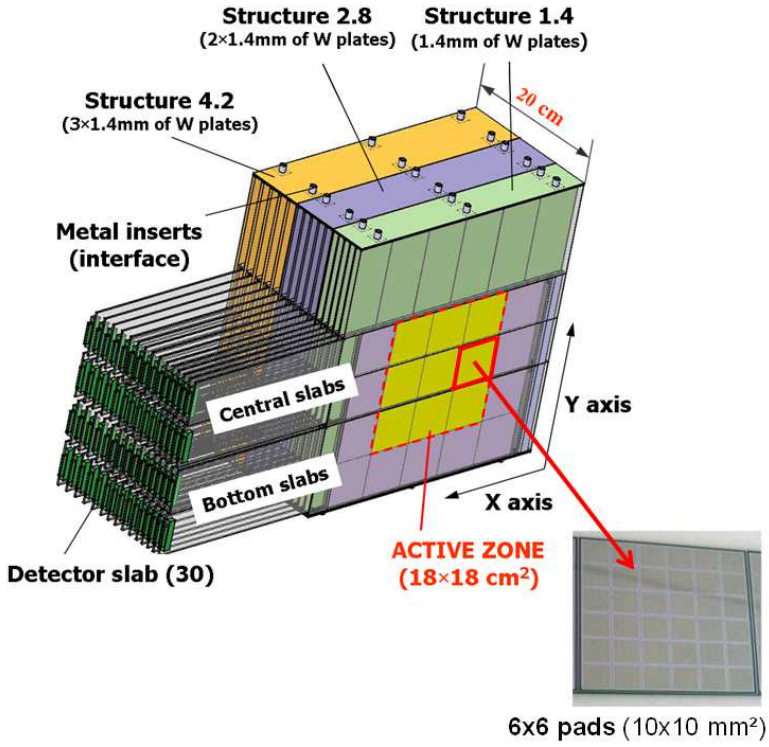

Figure 4.1: Sketch of the Calice SiW-ECAL prototype [36].

The silicon active medium has a thickness of 525 μm. A minimum ionizing particle (MIP) produces about 80 electron-hole pairs per μm, hence 42k electrons are obtained for the thickness of 525 μm [37].

The silicon wafers were glued to a printed circuit board (PCB) and two of them were mounted in H-shaped tungsten structure, with a tungsten layer between them to form an elementary detection unit called slab (see Figure 4.2). Each slab was

read out by the very-front-end ASICs called FLC_PHY3 placed on the outside of the detection area.

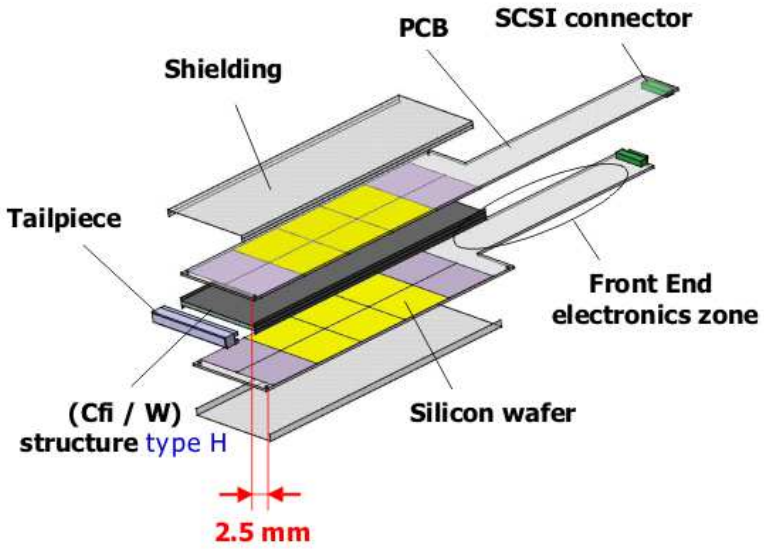

Figure 4.2: Schematic view of a slab [36].

4.3 Calibration and Results

The calibration process goals are to equalize the response of all the cells of the calorimeter to have the same signal for the same deposited energy, and to find the relationship between the measuring units and the physical units. The calibration procedure of the SiW-ECAL prototype consists of two steps:

- In a first step a MIP calibration is carried out. When a muon with momentum from a few hundreds MeV to a few tens GeV passes through the detector it loses its energy only through ionization, and has its energy loss rates close to the minimum. These muons are said to be minimum ionizing particles and are called a MIP. The mean energy loss of the muons in the active medium of a pad is defined as a MIP energy unit.
- In a second step an absolute calibration will be made by converting the unit of MIP to GeV, using electrons that deposit their energies completely into the prototype and where the energies of the electron beams are known.

4.3.1 The MIP Calibration Algorithm

The pedestal is the mean of the readout value in absence of a physics signal in a cell and is determined by details of the readout circuit. Subtraction of the pedestal from the readout signal gives the actual signal value. After this subtraction the resulting residual pedestal is checked for each channel. The noise peak is fitted with a Gaussian function and the mean of the Gaussian is taken as the residual pedestal and the width as the electronics noise. Then for each pad, a calibration constant is determined by fitting the hit energy distribution, of muon events, by a convolution of a Landau distribution with a Gaussian (see Figure 4.3). The Landau distribution describes the energy loss by the MIP while it is passing through the ECAL. The most probable value, MPV, of the Landau defines the calibration constant. The Gaussian distribution describes the uncertainty of the detector response due to the noise, and the sigma of the Gaussian defines the signal noise. This calibration constant gives the number of ADC counts for one MIP as illustrated in Figure 4.4, where the uniformity over the all prototype is emphasized. The calibration constant distribution allows to identify the layers glued at different manufacturers and at different times, shown by the different colors.

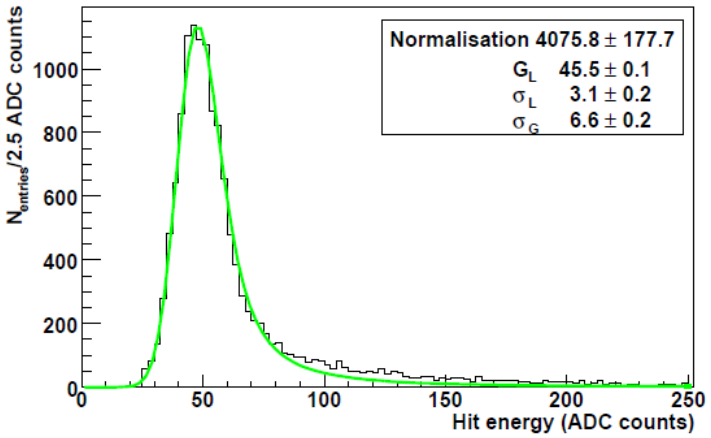

Figure 4.3: A typical fitting of the energy distribution of hits in muon events in a pad. The fit function is a convolution of a Gaussian and a Landau. G_L and σ_L refers to the MPV and the width of the Landau, and σ_G to the width of the Gaussian [37].

The stability in time has also been checked between the 2006 CERN beam tests and the 2008 FNAL beam tests with the good results of a correlation factor of more than 80 %, like shown on Figure 4.5. The stability of the calibration is

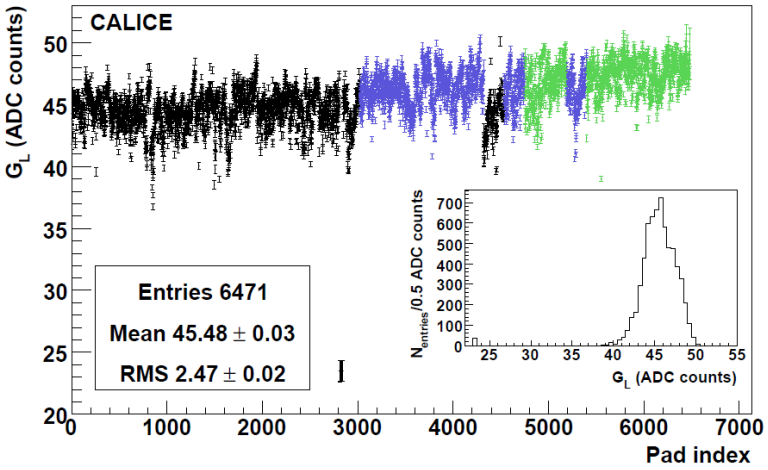

Figure 4.4: Calibration constant G_L for the energy deposit of a MIP for all the 6471 active channels of the prototype, obtained at CERN in October 2006 [37].

very important to operate a detector which at the end will comprise about 10^8 cells. The stability allows for the calibration in a test beam prior to installation and use this calibration during the physics data taking with only little monitoring effort.

A detail procedure of the calibration of the SiW-ECAL physics prototype for the beam test in FNAL in 2011 is given in Appendix.

4.3.2 Response of the Physics Prototype to Electrons

The results are based on data taken at CERN in 2006 with electron beams in the energy range of 6 to 45 GeV. Electron events, like the one in Figure 4.6, are selected and the performance of the SiW-ECAL are presented in terms of energy resolution, linearity of the response and angular resolution [38].

From the distribution of reconstructed energy of electrons at different energies one can parameterize the mean energy response and the measured energy:

$$E_{\text{mean}}(MIPs) = \beta E_{\text{beam}}(GeV) - \alpha; E_{\text{meas}}(GeV) = E_{\text{mean}} + \alpha \qquad (4.1)$$

where β is the second calibration factor, converting MIP to GeV, and α an offset partly due to the rejection of low energy hits. From the linear fit of the Figure 4.7 one find that the value of the conversion factor β is 266.5 ± 0.5 MIP/GeV. The residuals to the linearity of the measured energy are within the 1 % level, which is consistent with zero non-linearity.

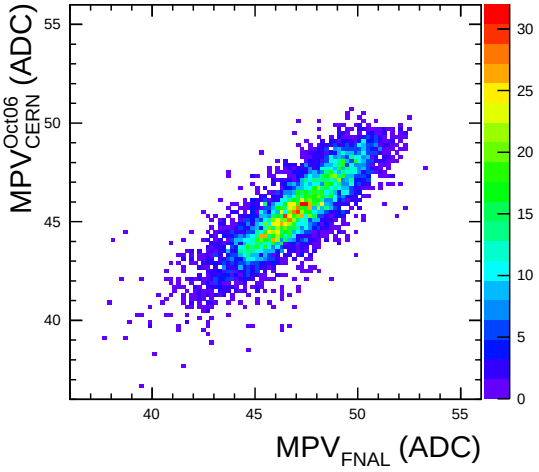

Figure 4.5: Correlation of calibration constants obtained from 2006 CERN muon runs with those obtained from 2008 FNAL muon runs [37].

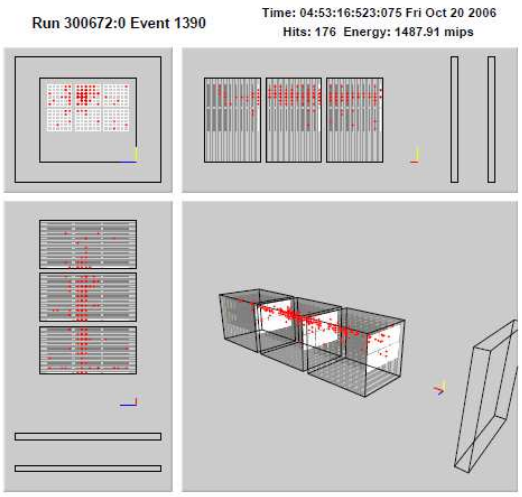

Figure 4.6: A typical 10 GeV electron shower in the ECAL. The colored cells have hit with energy higher than 0.5 MIPs [38].

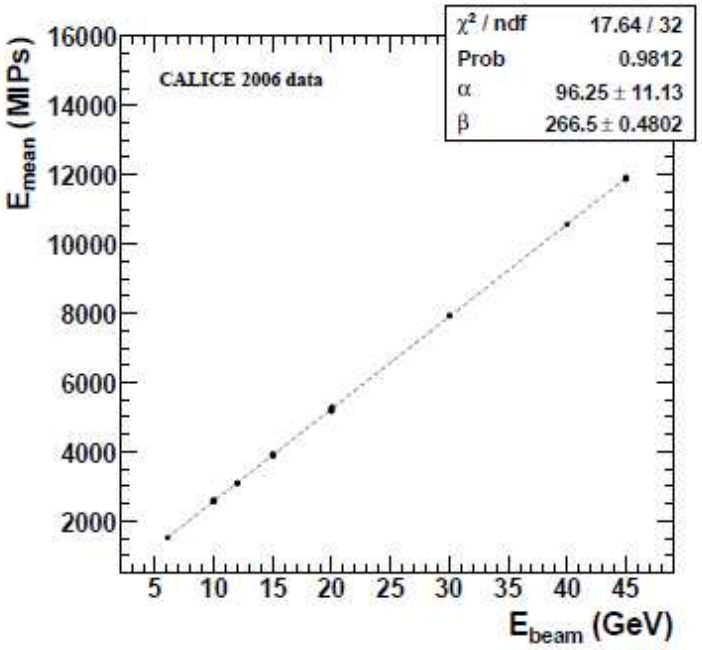

Figure 4.7: Energy responses of the SiW-ECAL prototype as a function of the beam energy [38].

The relative energy resolution $\Delta E_{\text{meas}}/E_{\text{meas}}$ is shown in Figure 4.8 and can be parameters by a quadratic sum of stochastic and constant terms:

$$\frac{\Delta E_{\text{meas}}}{E_{\text{meas}}} = \left(\frac{16.6 \pm 0.1}{\sqrt{E(GeV)}} \oplus (1.1 \pm 0.1) \right) \%, \tag{4.2}$$

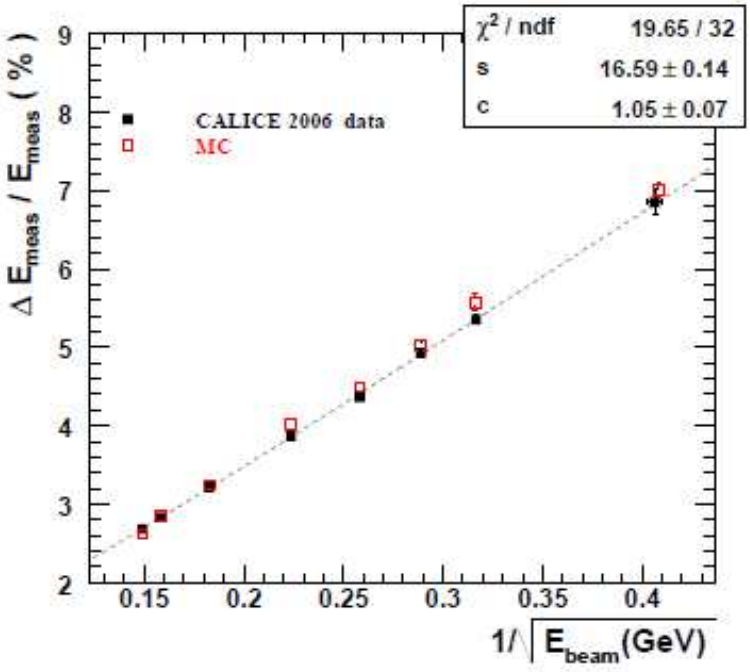

Figure 4.8: Relative energy resolution $\Delta E_{\text{meas}}/E_{\text{meas}}$ as a function of $1/\sqrt{E_{\text{beam}}}$, fitted by the usual parametrization function $s/\sqrt{E} \oplus c$ [38].

This is compatible with the value assumed in the full detector simulation of the ILD. A recent study with the data taken in 2008 at FNAL using 4 to 20 GeV positron beams confirmed this result [39].

The angular resolution has also been determined [40], using drift chambers behind the prototype to provide reference values. The results were found to be at the level of $100/\sqrt{E} \oplus 9$ mrad along the x and y directions.

Chapter 5

The Technological Prototype of the SiW-ECAL

5.1 Presentation

After the proof of principle by the physics prototype (see Chapter 4) the SiW-ECAL enters into the technological prototype phase [43]. The goal is to emphasize the engineering challenges of such a compact detector. The granularity is now four times higher than in the physics prototype with a pixel size of $5.5 \times 5.5\,\mathrm{mm}^2$. The design goal for the signal over noise ratio is 10:1. One of the main differences with the physics prototype is that now the readout electronics are placed inside the detector. This puts a lot of constraints on the size of the electronics and of the layers to keep the detector as compact as possible with the same radiation length. This requirement renders it impossible to integrate an active cooling system in the detector, so the electronics have to be as efficient as possible. The solutions used for the technological prototype have been tested in test beam with some layers close to a realistic design of the ILD ECAL.

5.2 General Design

Unlike the physics prototype, the design of the technological prototype has to be as close as possible to the one of the final ILD ECAL. It should prove the possibility to build a compact highly granular calorimeter.

5.2.1 The Mechanical Structure

The final size of the prototype will be 3/5 of a barrel module of the ILD detector to really face the challenges of a real scale detector on the mechanical point of

view. In this perspective a large mechanical structure made of tungsten-carbon reinforced epoxy (CRP) composite have been produced and tested with success (see Fig. 5.1). The structure has an alveolar form to be equipped with sensitive layer of the ECAL made of the silicon and the front-end electronics integrated inside the detector layers (see Fig. 5.2 and Fig. 5.3) to keep compactness. This choice results in a very compact structure with a minimal dead space. A leak-less water system for has also been developed for the technological prototype and tested successfully at an earlier mechanical demonstrator. Thin copper plates will ensure heat evacuation of residual heat from the inner parts of the detector layers to the outer part where a heat exchanger will be placed.

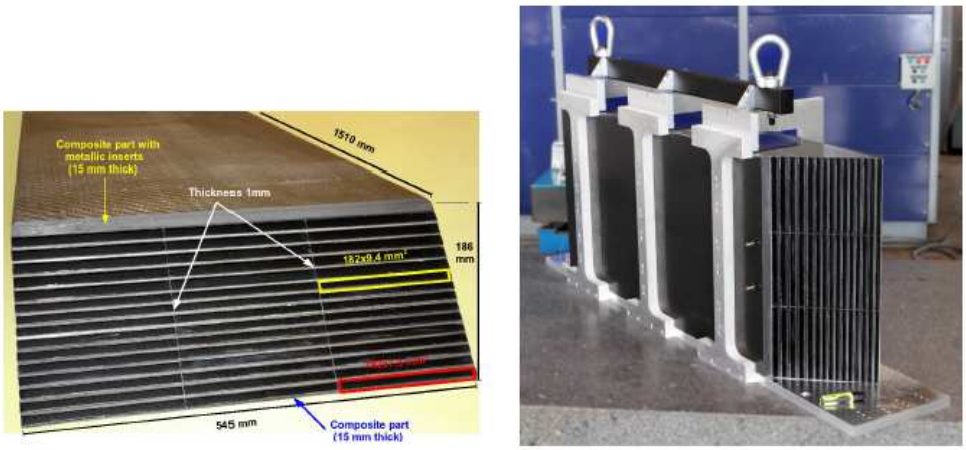

Figure 5.1: Left: Front view with dimensions of the alveolar structure which houses the sensitive layers of the SiW-ECAL prototype. Right: Side view of the completed structure and its mechanical protection [43].

5.2.2 The Active Sensors Unit

The sensitive parts of the detector, called a slab, which will be inserted inside the alveoli of the mechanical structure are composed of two detector layers, separated by one tungsten layer (see Figure 5.2). One detector layer is mainly composed of several Active Sensor Unit (ASU). An ASU is the entity formed by the readout Application-Specific Integrated Circuit (ASIC), an interface card (PCB) and the silicon wafer. A slab will have a height of about 6.8 mm, and should fit inside one alveolar of 7.4 mm leading to strict constraints on the flatness of the slabs and of the alveoli.

The silicon wafers are the active material of the detector (see Figure 5.4(b)).

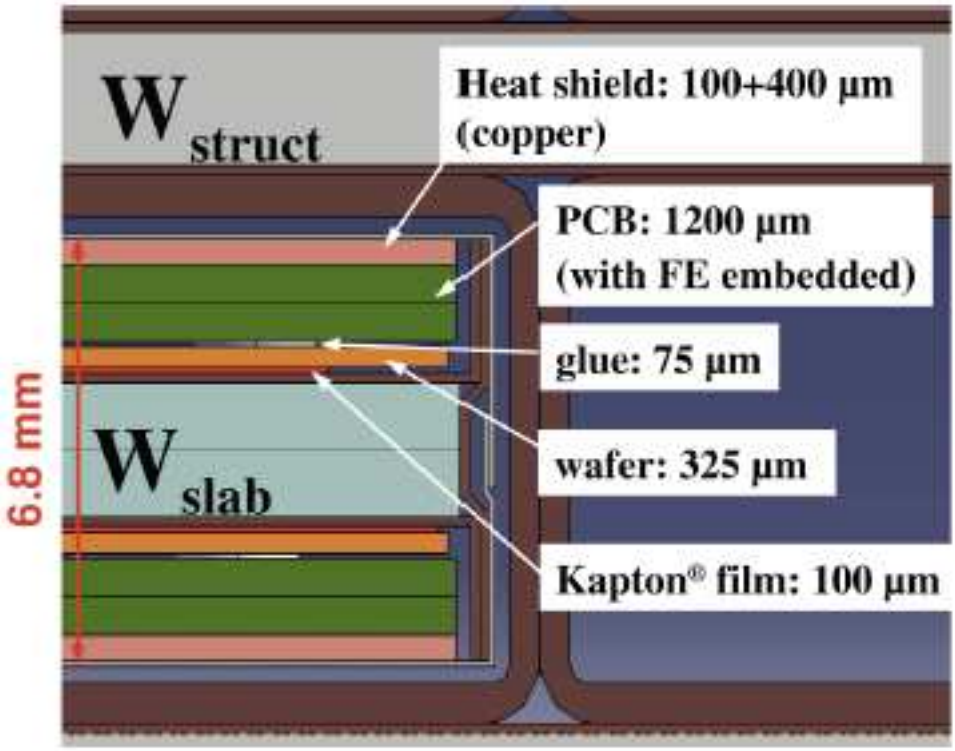

Figure 5.2: Cross section through one layer of the technological prototype [43].

For the prototype, Si wafers of $9 \times 9\,\mathrm{cm}^2$ with a thickness of $320\,\mu$m are used. The choice of the pixel size (5.5×5.5 mm^2) has been guided by optimization studies with PFA [44].

R&D on the silicon wafers is still ongoing, to fully characterize the wafers (I-V and C-V curves, V_{bias}, depletion voltage), but also to solve issues seen with the physics prototype. A crosstalk has been observed between the guard ring of the wafer and pixels at the edge of the wafer. This cross talk was visible by 'square events' in which all the pixels at the edge carried a signal. Studies have shown that segmented guard rings can reduce significantly this effect [36][78].

The PCB carries 4 silicon wafers and the SKIROC2 ASIC,the readout ASIC, and has to fit inside the mechanical structure (see Figure 5.2). This leads to constraints on the thickness (1.2 mm height) and the flatness (deviation from a flatness max of 0.5 mm) of the PCB. To reach these goals PCBs with encapsulated unpackaged ASICs are the current design baseline (see Figure 5.4(b)). Less challenging alternatives, with packaged ASICs, are also under study. Temporarily, PCBs with packaged ASICs and relaxed constraints on the thickness have been

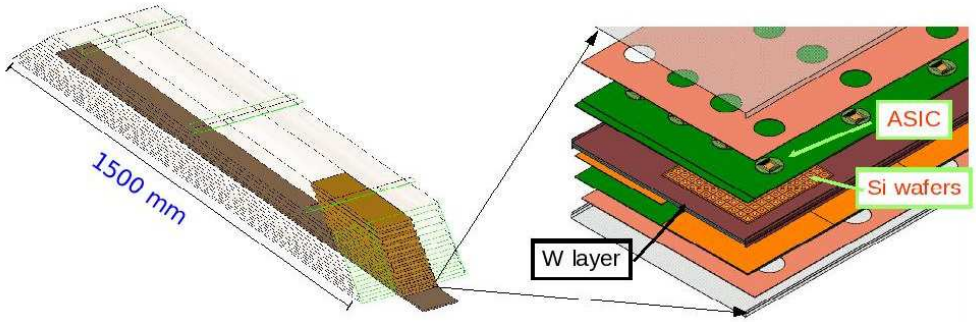

Figure 5.3: Left: Sketch of the layers inside the mechanical structure of the technological prototype.Right: Exploded image of one layer.

used for the test-beam presented in this thesis. The silicon wafers were glued onto the back of the PCB using the conductive glue EPOTEK-4110. For the gluing robotic techniques similar to those described in [43] are under investigation.

The SKIROC2 ASIC is designed to read out the silicon pin diodes of the Si-W ECAL and will be described in detail in the next section.

5.3 The SKIROC2 ASIC

One of the main changes between the physics prototype and the technological prototype is the front end electronics. In the physics prototype the FLC_PHY3 ASICs are located outside of the detection area at the end of each layer (see Figure 4.1), while in the technological prototype the front end electronics is integrated inside the detector layers, to minimize the non-equipped space in the detector.

The SKIROC2 ASIC (Silicon Kalorimeter Integrated Read-Out Chip) is a 64-channel very front end ASIC designed for the readout of silicon PIN diodes in AMS 0.35 μm SiGe technology [45][46]. It supports the design requirement of ILC detectors in terms of hermiticity by a high level of integration. To fit inside the slab the ASIC has a size of $7.2 \times 8.6\,\mathrm{mm}^2$. The acquisition chain, amplification, trigger decision, digitization and readout, are integrated into the ASIC. Each channel is made of a variable, high and low, gain charge preamplifier followed by a dual shaper to filter the charge measurement and a trigger chain. The measured charge is stored in a 15-depth buffer and sent to a 12-bit ADC to be read out.

The other important aspect of the integration of the ASICs inside the detectors is that its power consumption should be very low to limit the heat dissipation. In this way, in addition to a low power consumption of the ASIC by itself, it has been suggested to take advantage of the ILC spill structure. The ILC beam is not a continuous beam, but it will arrive in bunch trains with a length of around

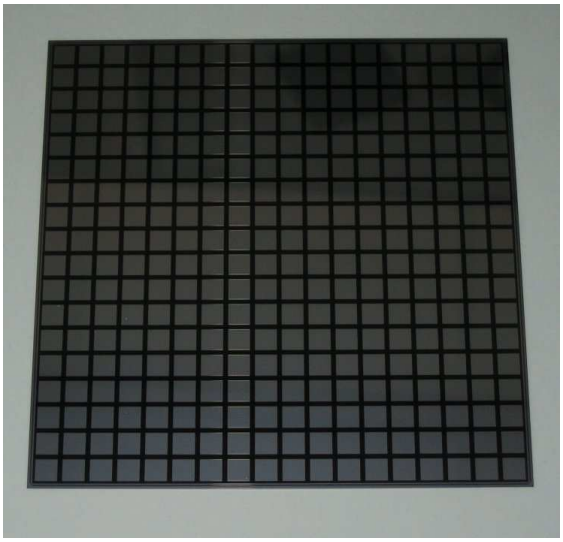

(a)

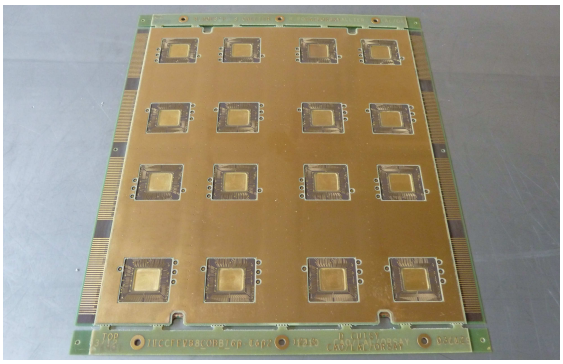

(b)

Figure 5.4: (a) Silicon wafer matrix. (b) PCB prototype for embedding the chips.

1 ms and a time gap between bunches of around 199 ms (see Figure 5.5). In other words, the detector is idle for 99 % of the time and the electronics doesn't need to be active. To take advantage of this ILC particularity each section of the ASIC can be deactivited independently when it is not needed (see Figure 5.5). This is called power-pulsing and can reduce the power consumption from 1.5 mW to 25 μW per channel.

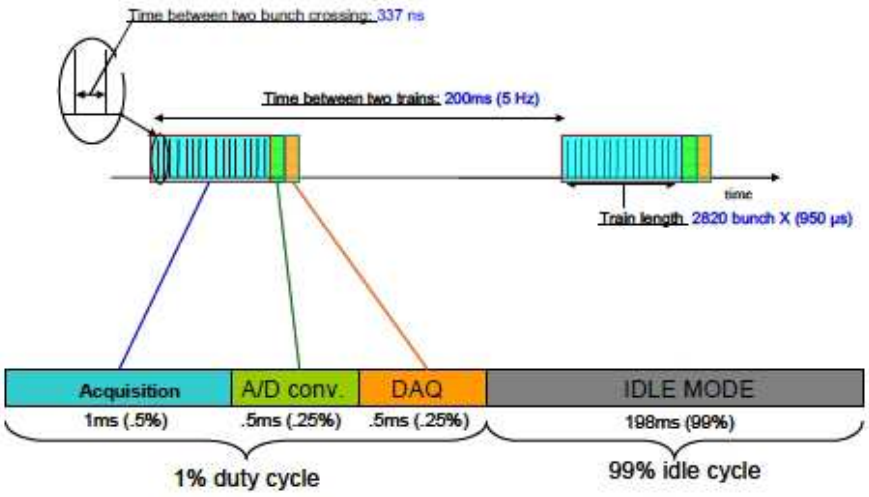

Figure 5.5: Schematic illustration of the power pulsing relation to the ILC spill structure.

The analog part (see Figure 5.6) has been designed to handle a dynamic range of charge depositions between 0.4 fC and 10 pC, where 4 fC is the charge deposition expected for a MIP, leading to a MIP dynamic range of 0.1 to around 2500 MIPs. Each channel is made of an input charge preamplifier, the red part in Figure 5.6. The gain of the preamplifier is adjustable by changing the feedback capacitor C_f.The gain varies logarithmically as a function of $1/C_f$. Each preamplifier is followed by a slow line for the charge measurement and by a fast line for the trigger decision. A bandgap ensures the stability with respect to supply voltage and temperature for all the requested references in the analogue core. An internal slow clock, with a frequency up to 5 MHz, is used for the time stamping of the events. This timestamp number uses the bunch crossing of the two beams as reference and is called Bunch Crossing Identifier (BCID).

As explained in Chapter 2 the ILC doesn't have an external trigger. This means that the ASICs have to record all the signals that they measure in their channels above a threshold, independant of the rest of the detector. For this purpose the SKIROC2 ASICs have the capability of self-triggering on the signal with an internal trigger or auto trigger. The goal is, for each channel, to be able

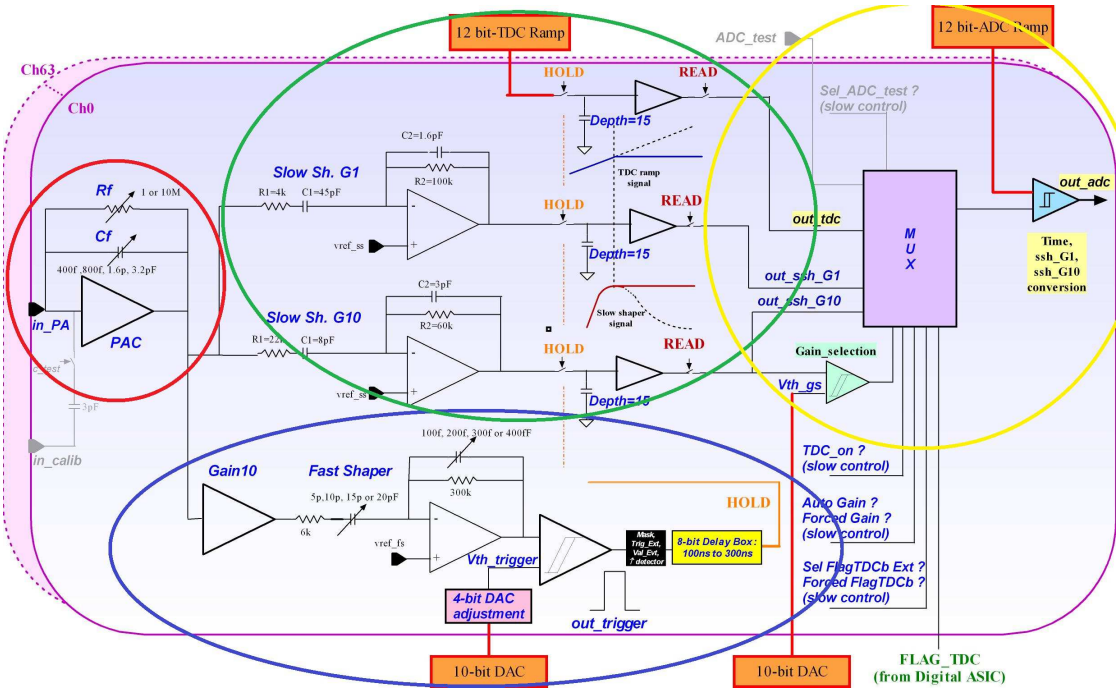

Figure 5.6: Simplified schema of the SKIROC2 analog part [45].

to trigger down to 0.5 MIP.

The fast line of the analog part is the auto trigger system, the blue part in Figure 5.6. It consists of a high gain variable CRRC shaper, with an adjustable integration time set to 30 ns, followed by a low offset discriminator to trigger down to 0.1 MIP. If the fast integrated signal is above the threshold of the discriminator the channel is seen as having a hit and the event is recorded in the channel and in all the other channels of the ASIC. The threshold of the 64 discriminators is supplied by a common 10-bit DAC but a supplementary 4-bit Digital Analog Converter (DAC) is implemented for the fine adjustment of the individual channel trigger thresholds. Each discriminator output is sent to an 8-bit delay cell to provide the hold signal for the slow line. The delay time can be varied between 100 and 300 ns.

The slow line, the green part in Figure 5.6, is made of a low gain and a high gain CRRC shapers to cover the large dynamic range. A track and hold cell is used to measure the signal at its peaking time. The measured signal from the two slow shapers are then stored in a 15 depth buffer line. The switched capacitor array (SCA) change instruction is validated at the first rising edge of the internal ASIC slow clock after the logical disjunction of the 64 channels triggers (OR64 signal). For all channels without hits, the hold signal is sent at this rising edge of the slow clock, measuring also a signal which is used to determine the position and width

of the pedestal. The charges stored in the SCA cells are then converted by a 12-bit Wilkinson ADC, the yellow part in Figure 5.6, and sent to an integrated 4 Kbyte memory.

5.4 The Test Beam Setup

The first layers of the SiW-ECAL technological prototype have been tested in beam in 2012 and 2013 [47][48]. The prototype was made of up to 10 layers, with a conservative design where the ASICs were packaged on the PCBs (see Figure 5.8). The sensitive part of the detector was an array of PIN diodes made of 320 μm thick high resistivity silicon of around $9 \times 9\,\mathrm{cm}^2$ and a pixel size of $5 \times 5\,\mathrm{mm}^2$. One PCB can be equipped with four of these silicon wafers, but only one per PCB were glued for the test beam. The wafers were glued to the 1.45 mm thick PCBs using a robotic procedure and each pixel were linked to the ASICs channels. Each PCB was equipped with four SKIROC2 ASICs, corresponding to 256 readout channels. The PCB and the ASICs were planned for wafers of 16 $\times$ 16 pixels, but wafers of 18 $\times$ 18 pixels had to be used for the test beam (for historical reasons). So like the number of pixels didn't met the number of channels, some of the channels were linked to more than one pixel. This mapping leads to very noisy channels, when they were linked to several pixels, and so the preamplifiers of these particular channels were disabled for the data taking. The mapping of the pixels of the sensor to the ASICs M1 to M4 within a layer is illustrated in Figure 5.7.

Each layer was mounted in a U-shaped carbon board, closed with a 300 μm aluminum cover (see Figure 5.8). The overall thickness of each layer was 7 mm, and has to be compared to the alveoli of the mechanical structure which are 7.4 mm height and should accommodate two detector layers and one tungsten layer. To test these first detector layers the mechanical structure demonstrator have not been used. The layers were inserted into a PVC support structure designed to house up to ten layers, shown on Figure 5.9. In the structure the distance between successive layer positions was 15 mm and a 2.1 mm-thick tungsten plate could be inserted in front of each layer.

Each layer is equipped with a Detector InterFace card (DIF) to ensure the link with DAQ system [49][50]. The ILC beam structure is emulated using a pulse generator which simulated spills of 1 ms duration at 100 ms or 200 ms intervals. In a run, each acquisition is flagged with a spill number which is a counter of the spill periods.

The detector was mounted on a movable stage, with the layers arranged perpendicularly to the beam direction. The beam test line at DESY provides electrons from 1 to 6 GeV. A carbon fiber is put in the electron/positron synchrotron DORIS II to produce a bremsstrahlung photon beam. The photons are then converted to

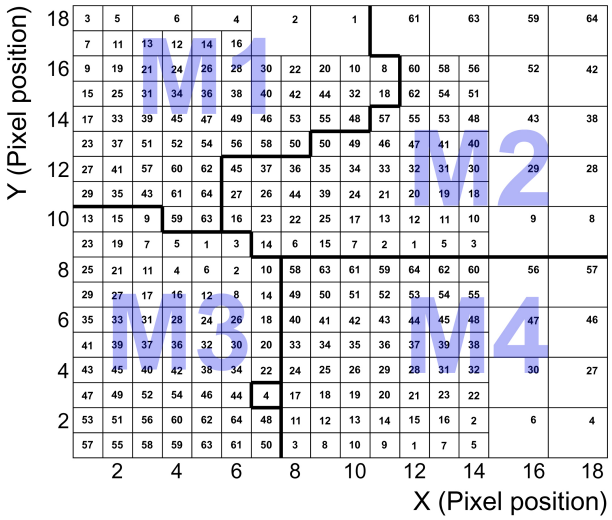

Figure 5.7: Mapping of the channels of one layer. The ASIC channels connected to sensor pixels are shown as a function of the pixel position. The broad lines represent the ASIC borders. Some ASIC channels are linked to several pixels (large boxes). The isolated channel 4 between M3 and M4 belonged to M2.

electron/positron pairs with a copper target. The beam energy is selected with dipole magnets and collimator. The layout of the DESY test beam is shown in Figure 5.10. The moving table allows to modify the position of the detector with respect to the beam. In the following the feedback capacitance of the SKIROC2 ASIC was set to $C_f = 1.2\,\mathrm{pF}$, to have a high gain in the preamplifier.

5.5 The Trigger Calibration

5.5.1 The Trigger Threshold

As explained in Section 5.3 the ASICs of the SiW-ECAL prototype has an auto trigger capability to record events without an external trigger. The implies that the first step of the calorimeter calibration is the selection of the threshold values for the ASIC channels. The goal of this calibration is to assure an optimal separation of signal from noise. The design of the SKIROC2 ASIC allows for a channel by channel adjustment of the value of the threshold, but it turned out that the range of the correction was too small to be useful for the test beam. Therefore a common threshold for the entire ASIC has to be set.

The method used to choose the threshold value was the one of the 'S-Curves'.

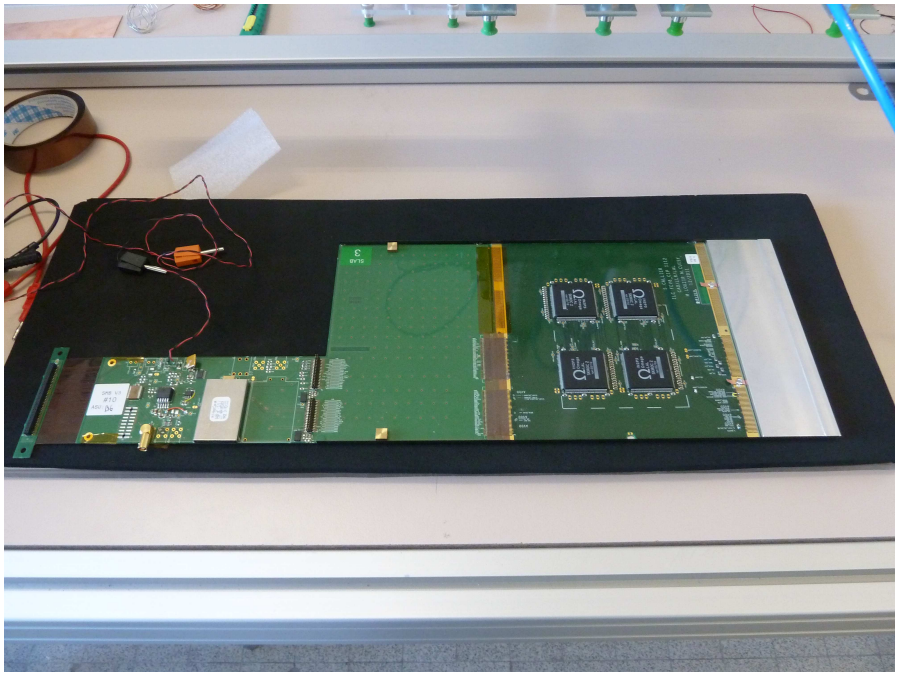

Figure 5.8: Picture of one layer without aluminum cover.

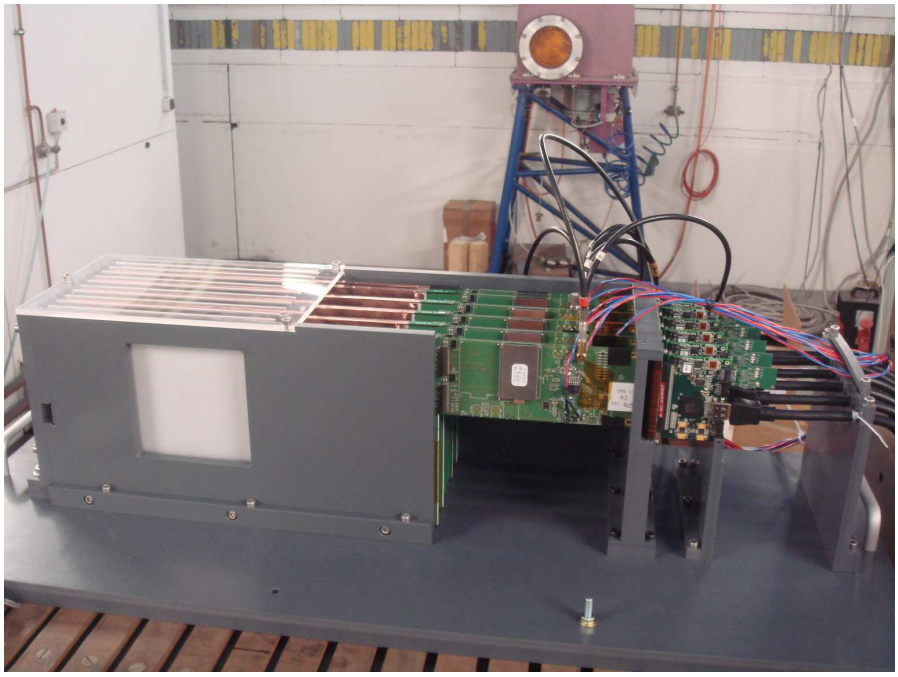

Figure 5.9: Picture of the experimental setup with 6 layers.

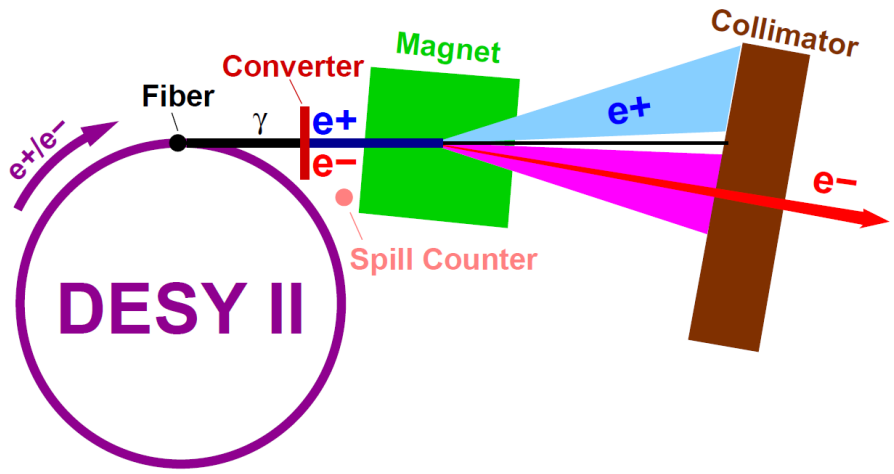

Figure 5.10: Schematic layout of the test beam at DESY.

By varying the trigger threshold the noise spectrum of all the channels has been scanned. The result is a curve with an S shape, where the number of hits is high when the threshold cut is below the pedestal position and approaches zero for higher values of the threshold, as illustrated on Figure 5.11. In one channel the threshold is defined as the value for which the number of hits is lower than 1 % of the number of hits in the plateau. The distribution of the value of the threshold found for each channel independently is shown in Figure 5.12. The common value of the threshold for the all ASIC channels is chosen as a compromise between the detection efficiency and the noise frequency level. The preamplifier of channels with a too high threshold value with respect to the ones of the other channels of the ASIC were disabled. Apart from those channels connected to four pixels, see above, another 9.5 % of the channels were disabled because of a too high noise due to a non optimal routing of the PCB. In fact some electrical lines were passing too close to the signal lines. With a better PCB routing and the channel to channel adjustment in place most of these disable channels can be used in a future version of the detector layers.

5.5.2 The Trigger Delay

The trigger signal is delayed to select the time at which the signal is read along the pulse as generated by the slow shaper. This optimal delay depends on the trigger threshold and should be at the maximum of the integrated signal, as illustrated on Figure 5.13. A scan of delay values, called holdscan, was performed during the test beam. For each channel, we measure one distribution of the number of hits with beam per delay value. The maximum position of each distribution

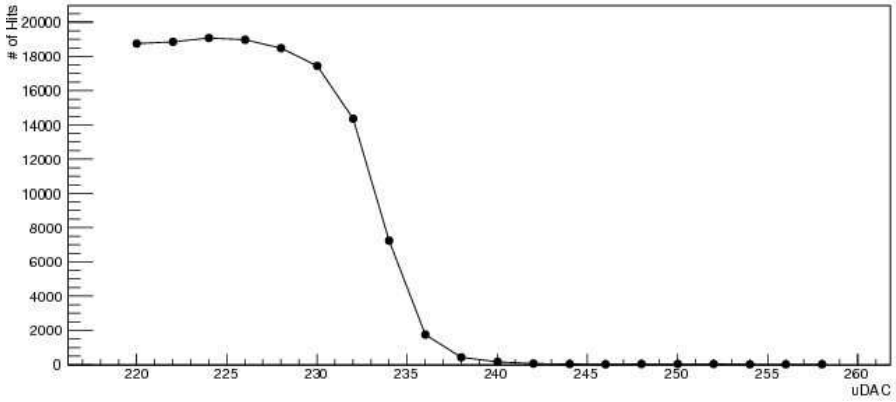

Figure 5.11: Number of events with hit in function of the trigger threshold, in unit of DAC, for the channel 2 of the ASIC M1.

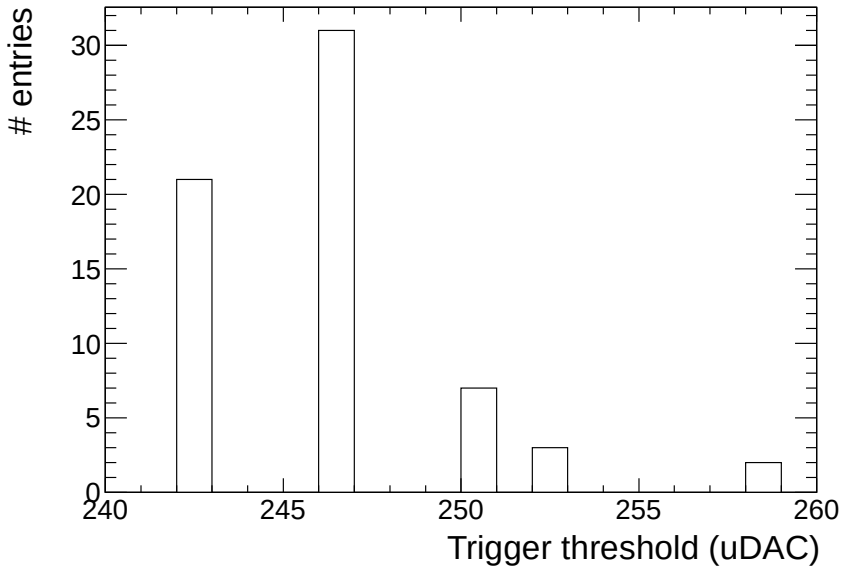

Figure 5.12: Distribution of the trigger threshold for all the channels of one ASIC.

is plotted as a function of the delay values for each channel, as for example in Figure 5.14. The chosen delay value corresponds to the maximum of the curve and is common to all the channels of one ASIC. The maximum of all channels is found in the range 120-140 DAC units and was set at 130 DAC unit, approximately 260 ns, for all ASICs during the test beam.

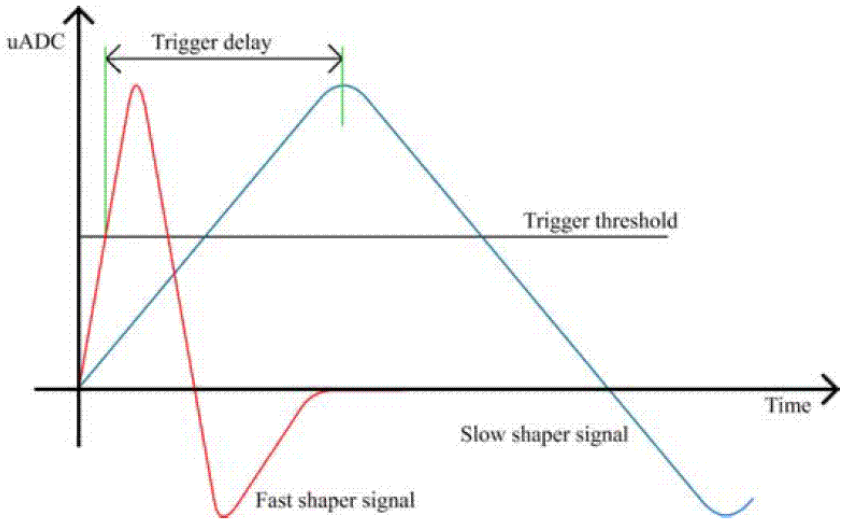

Figure 5.13: Illustration of the value of the hold and of the trigger threshold with respect to the integrated signal.

5.6 Results Without Power Pulsing

The goal of the first test beam was to check the performance of the detector layers and in particular that of the front end electronics. In a first step the power pulsing mode was not used and the ASICs were powered continuously to gain experience on the implementation of the detector. A first point was to establish a calibration procedure for all the channels, as outlined in the previous Section. To check the quality of the signal and its homogeneity the goal was to determine the signal over noise ratio of the detector. The signal over noise ratio is defined as the ratio between the distance pedestal - MIP and the sigma of the pedestal (see Figure 5.15).

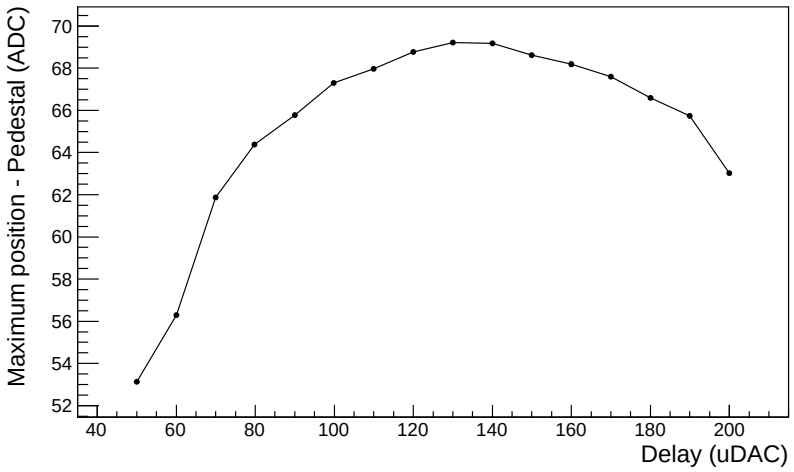

Figure 5.14: Maximum position of distributions measured with different delay values for the channel 61 of the ASIC M1. The position is plotted as a function of the delay values in unit of DAC.

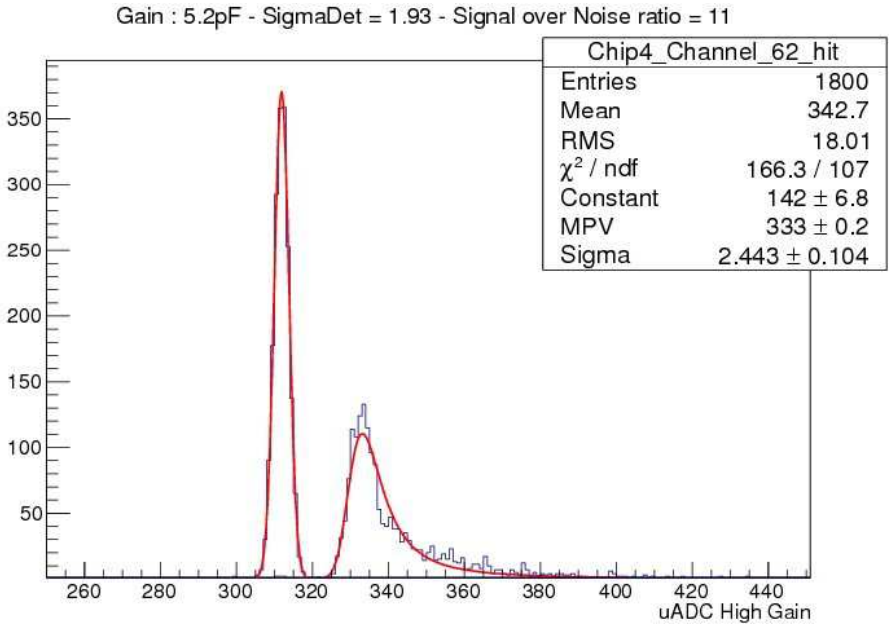

Figure 5.15: Pedestal and MIP distribution for one channel.

5.6.1 Pedestal and Noise Measurement

Each channel has an intrinsic noise generated from the electronic noise, which is different for all the channels. This effect takes the form of a different pedestal width for each of the channels and even for each of the 15 SCAs of a single channel. Also the position of the pedestal is different for each of the SCAs. To correct for this dispersion the value of the pedestal has to be subtracted of the measured value on a line by line basis within a buffer. To get the pedestal distribution of each channel the non-triggered events stored along with the hits were used. A pedestal event of a channel was defined as an event without a hit in the channel and in the neighboring ones. The resulting distribution is fit by a Gaussian distribution (see Figure 5.15), whose mean defines the pedestal, and the width defines the noise.

As mentioned before, the value of the pedestal depends on the SCA number. Therefore, pedestals have to be subtracted individually for each SCA number as illustrated by Figure 5.16 that shows the typical pedestal and noise as a function of the SCA number for one channel. On the other hand the noise level in the individual buffer lines is within 5 % of the mean of all the 15 buffer lines. Therefore the mean of these 15 buffer lines is a good approximation of the channel noise.

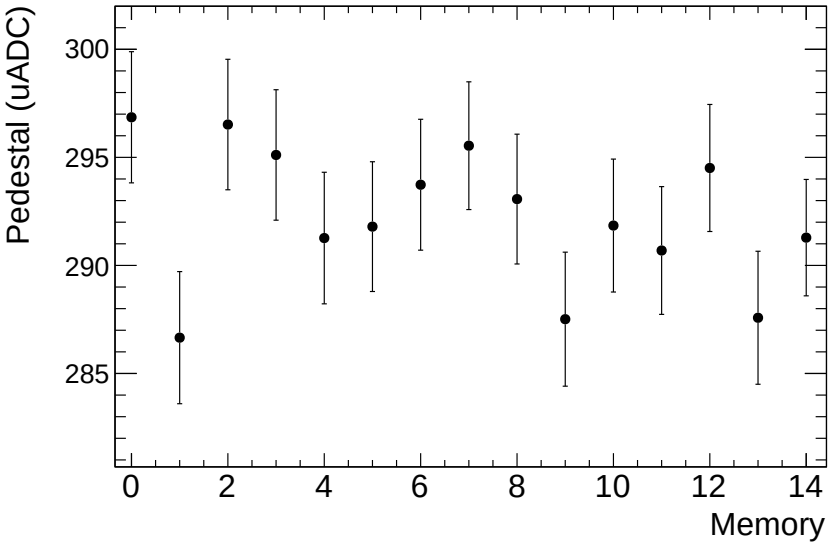

Figure 5.16: Pedestal as a function of the SCA number for one channel. The length of the error bars reflect the noise.

Figure 5.17 shows the map of the noise in one layer of the detector. The map has the same layout as Figure 5.7 and the white spots are the disabled pixels, with a noise value around 1.5 ADC counts. For the active channels there is a clear pattern that depends on the ASIC position, which repeats for all the layers. The

two left ASICs, M1 and M3, have a lower noise value, around 3.2 uADC, than the two right ones, M2 and M4 that have a mean noise value around 4.2 uADC. This effect can be explained by the PCB routing since the behavior is the same for all the layers. One important fact is the position of the ASICs on the PCB with respect to the silicon wafer. Depending on this position the passage-way between pixels and the ASIC is not the same for all the channels. In particular the lines of the ASICs M2 and M4 channels are longer than the ones of the ASICs M1 and M3. In Figure 5.18 the noise value of each channel is plotted against the electronic line length on the PCB, and the correlation between both demonstrate the strong influence of the PCB routing on the observed noise level.

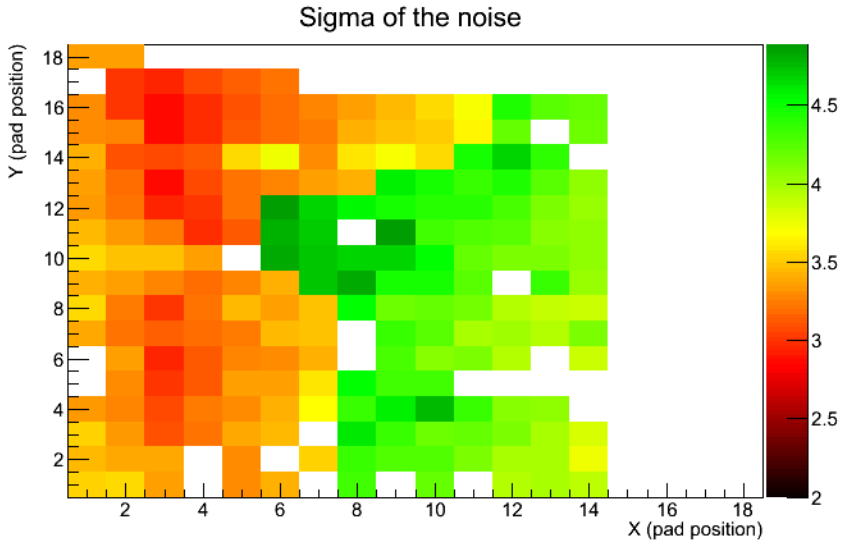

Figure 5.17: Map of the noise for one layer of the detector. The white spots are the switch off pixels.

5.6.2 Filtering the Events

During the data taking, we observed that some of the events were not caused by beam particles. We found two types of fake events: BCID+1 events and plane events, and that these fake events were due to the ASIC design [51]:

– BCID+1 events: the ASIC needs at least one triggered channel to validate and to store an event, but we observed events without hit in any channels. These events appeared one BCID after a valid event in the same ASIC. The reason was investigated and we found that it is caused by the event storage

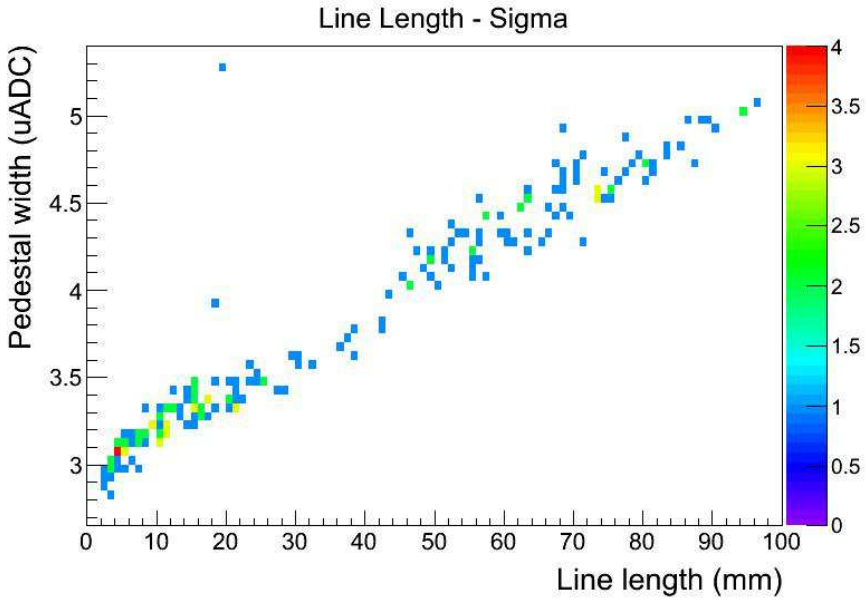

Figure 5.18: Dependence of the noise as function of the electric line length on the PCB.

sequence of the ASIC, see Figure 5.19. When one channel of the ASIC has a hit the acquisition starts, and the OR64 signal sends the instruction to record the event. The event is well recorded in the SCA, but it may happen that the rising edge of the slow clock falls during OR64 signal. In this case, after the rising edge of the slow clock, the OR64 signal is still active. Thus, at this new rising edge of the slow clock, the SCA change instruction is validated again, even if no trigger occurs in the slow clock period. The values stored in the next SCA correspond to the signal measured one clock period after the real event, with a BCID incremented by one compared to the real event. The frequency of such events is equal to the length of the OR64 signal divided by clock period. We calculated that around 13 percent of the physics events is followed by BCID+1 events, and this was confirm by the analysis of the data. One should note that this effect is due to the fact that the beam is not synchronous with the clock of the ASIC, while it will be the case for the ILC beam.

– Plane events: the ASICs have a high inrush current when a lot of channels are triggered or when several ASICs have triggered channels. The high inrush currents can lead to voltage dips in the power supplies of the ASIC, which are seen as a signal by the preamplifiers. Like the power supplies are common to the four ASICs of the PCB and to the 64 channels of the ASICs,

fake signals may appear arbitrarily in any ASIC of the layer. For the most impressive events, all the switched on channels of the layer are triggered, looking like an all plane events, see Figure 5.20 for example. This effect is self-sustained because, like a plane event has some triggered channels in the layer, it may create a subsequent plane events, even until all the ASIC SCAs are full. During test beam, the measured ratio between plane events and good events is in the range 0.3 to 3. The ratio depends on the beam position and the setup. For instance, with tungsten plates, the high number of triggered channels increases the probability to have plane events. To avoid plane events, the ASICs need a very stable analog power supply. Two improved setups have been tested on the test bench and in test beam. In the first setup, we increased the power supply stabilization capacitance. In the second setup, we modified the power supply lines to protect the analog power supply. We observed a reduction of the plane events by a factor 8 to 10 in the two setups as illustrated in Figure 5.21. We observed that these fake events appear mainly a few BCIDs after the previous event, so in this analysis, we cut an event if the BCID difference with the previous event in any ASIC of the layer is less than 5.

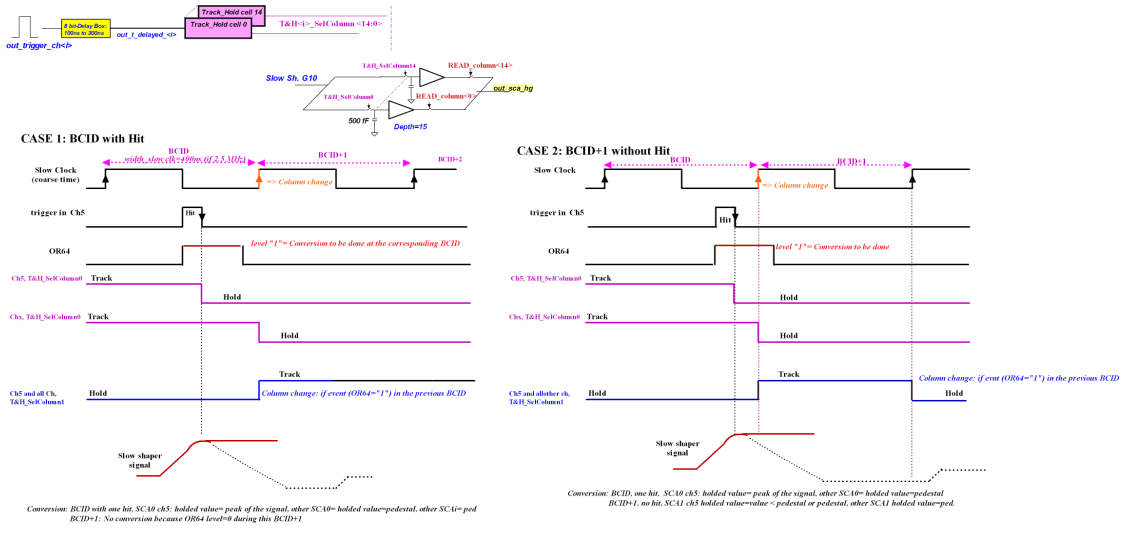

Figure 5.19: Logical diagram illustrating the BCID+1 effect.

In the following all the analysis is done with a off-line filter on these nonphysical events.

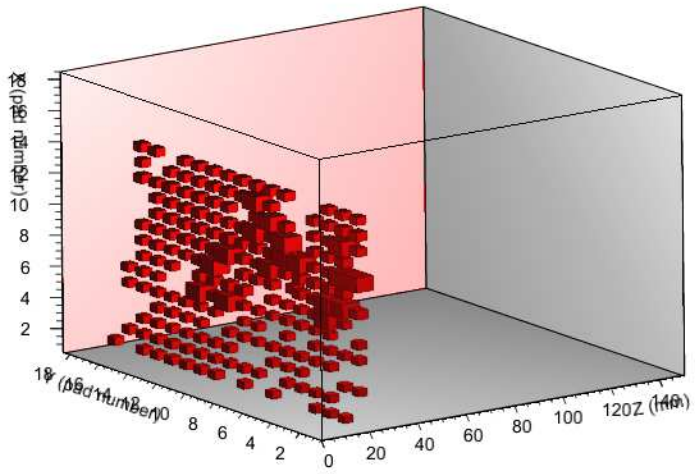

Figure 5.20: Example of a plane event in one layer of the detector. The size of the boxes are proportional to the energy deposition.

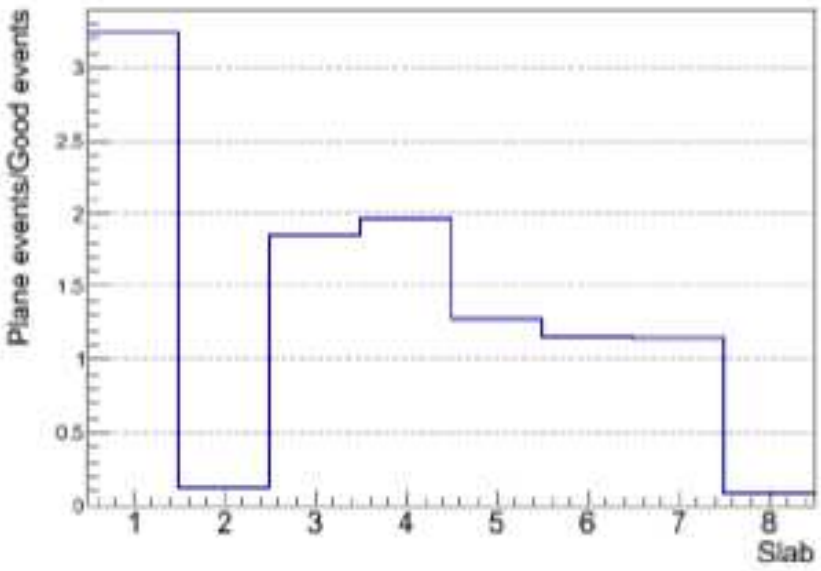

Figure 5.21: Frequency of plane events. The Slabs 2 and 8 were subject to patches explained in the text.

5.6.3 Signal Over Noise Ratio

The homogeneity of the first layers of the SiW-ECAL technological prototype was tested by performing an energy calibration over all the active pixels of the detector. For that, without tungsten absorber electrons can be considered in good approximation as MIP at the energy scale of a few GeV. The electron beam was scanned over the entire sensitive area of the detector. Figure 5.22 shows the beam spot in the detector, in the case when no tungsten plates were inserted between the detector layers. Like for the physics prototype the distribution was then fitted to a Landau function convoluted with a Gaussian (see Figure 5.23). The MIP calibration factor is given by the most probable value, MPV, of the Landau. The noise of the detector was determined from the width of the Gaussian. We checked that this value was the same than the one obtained in the fit of the pedestal. As both were at the same level, for practical reasons we fixed it in the convolution to the value measured in the pedestal studies. The map of the MIP calibration values for one layer, of the Figure 5.24, shows that the distribution of the MPV is much more uniform among the ASIC than the noise. Indeed the distribution of the MPV for all the active channels (see Figure 5.25) has a Gaussian shape with a mean value around 73 uADC and an RMS of 2.2 uADC. The measured signal depends on the trigger calibration, via the hold but also via the trigger threshold value, so one could expect an improvement of the homogeneity of the MPV distribution thanks to the individual channel trigger threshold adjustment.

Once the noise and the MIP calibration constant are measured for all the active channels it allows to measure the signal over noise ratio, S/N. This ratio is an indication of the detector capability to separate the signal from the noise and is very important in the context of an auto-trigger detector. S/N is defined as the ratio between the MIP calibration constant and the noise. The figure 5.26 shows the map of S/N for one layer of the detector. Here again there is a clear pattern depending on the ASICs position, that repeats for all the layers, because of the noise map patterns and of the uniformity of the MPV map.

One should note that on the map the S/N values are too optimistic with respect to the final detector configuration due to the feedback capacitance, C_f, value used. Indeed a C_f of 1.2 pF was used in a first step to have a higher gain preamplifier and a dynamic range more suited to the DESY test beam energy range, which is of course much lower than at the ILC. This gain is the one used in the previous results and permit to emphasize the different behaviors of the ASICs with respect to their position on the PCB. Later on several feedback capacitances were tested to check that the results with a lower gain, up to the design one of the ILD ($C_f = 6$ pF). Figure 5.27 shows S/N for different C_f values, with the double peak structure due to the noise pattern. The measured S/N was found to be better than the physics prototype one (7.5:1) and than the design goal of 10:1 for all the gain settings.

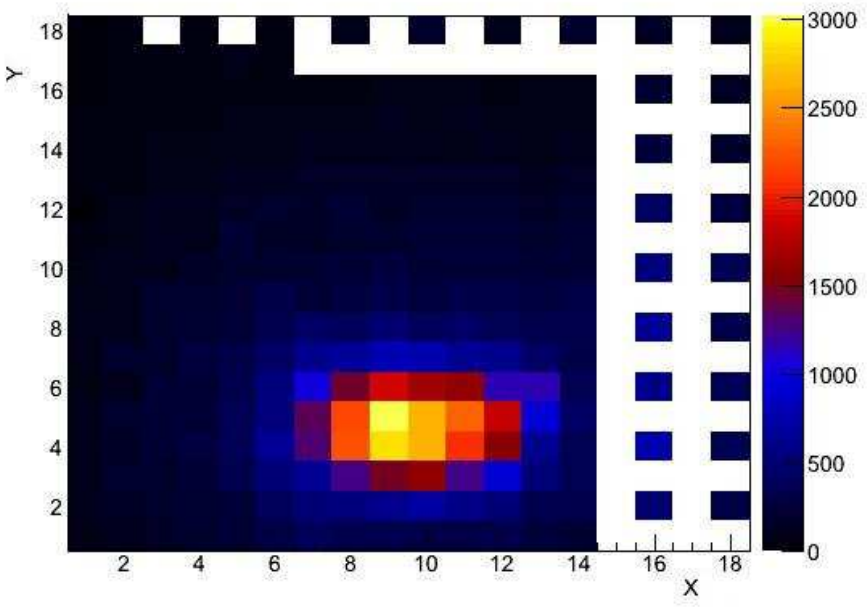

Figure 5.22: Beam spot in one layer of the detector.

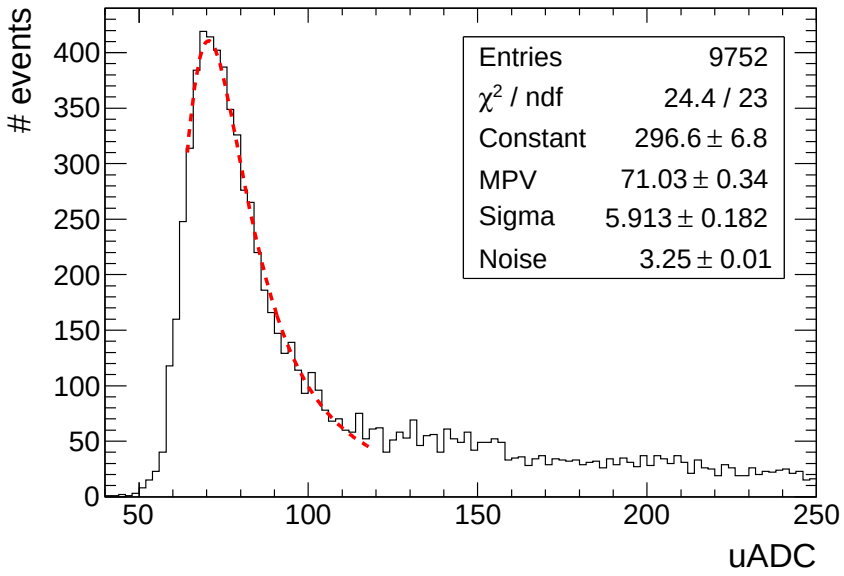

Figure 5.23: MIP distribution in one channel after pedestal subtraction. The distribution is fitted to a Landau function convoluted with a Gaussian.

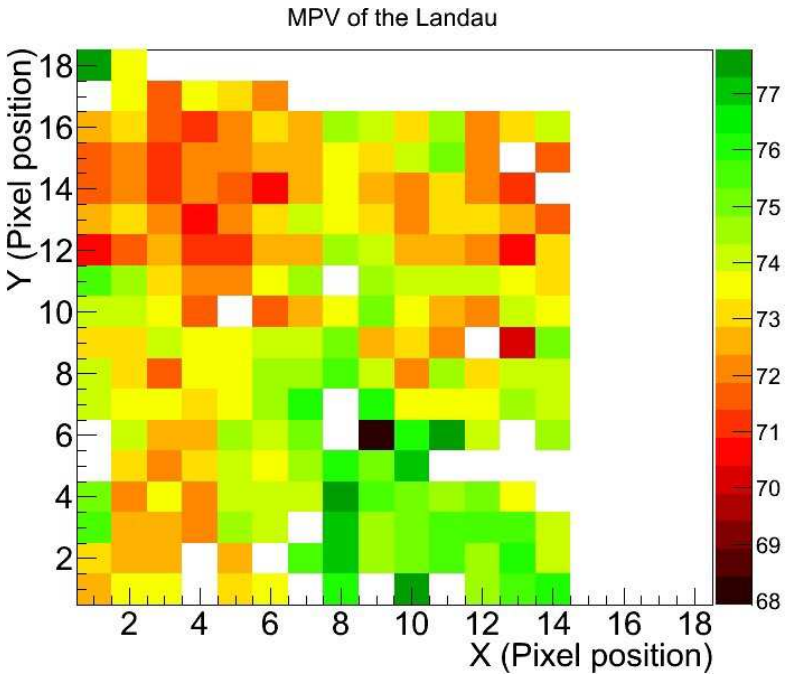

Figure 5.24: Map of the MPV of the Landau function for one layer of the detector. The white spots are the switch off pixels.

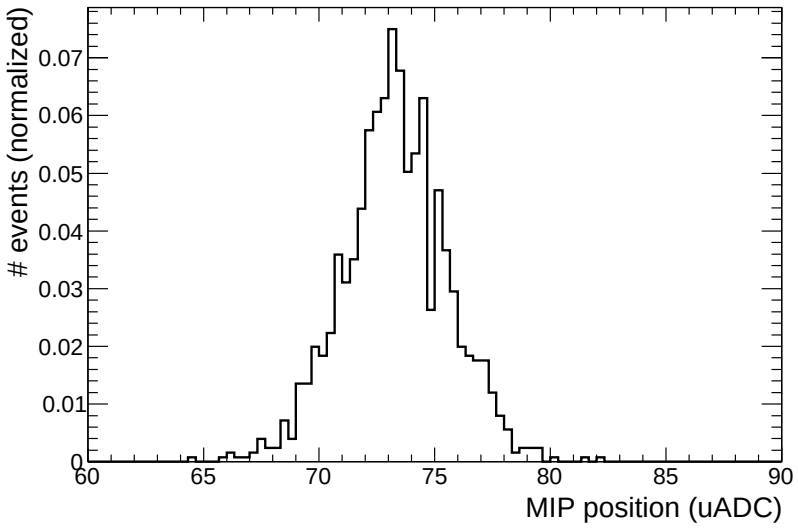

Figure 5.25: MPV of the Landau function for all active channels.

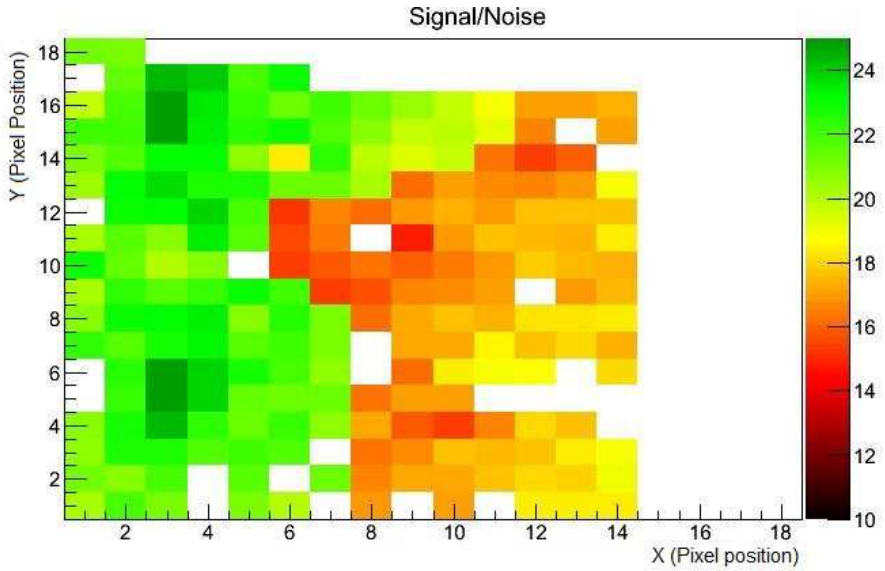

Figure 5.26: Map of the signal over noise ratio for one layer of the detector. The white spots are the switch off pixels.

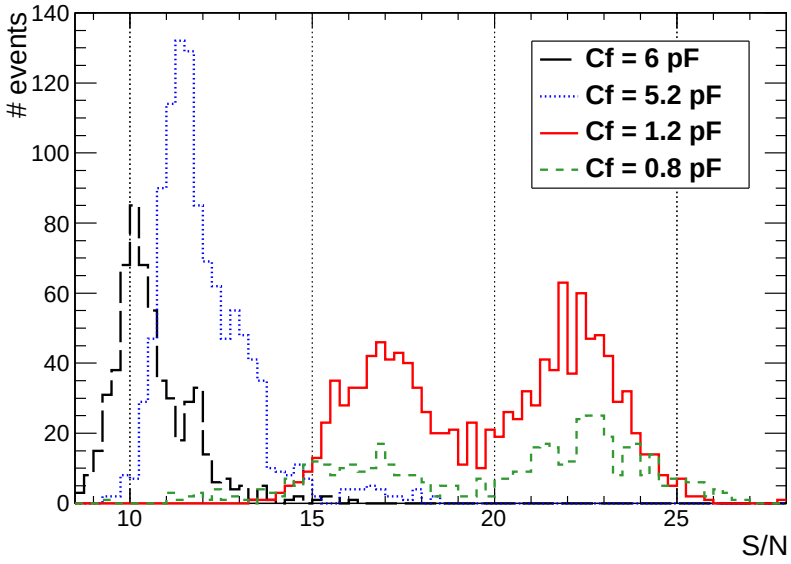

Figure 5.27: Signal over noise ratio for all active channels for several feedback capacitances. Long dashed black line corresponds to $C_f = 6\,\mathrm{pF}$, the designed value for the ILD.

5.7 Results With Power Pulsing

The studies without power pulsing were carried out to measure the characteristics of the detectors in optimal condition, and to gain experience in the use of the detector. The same kind of studies were repeated with the power pulsing mode of the front end electronics. On the ASICs when the power pulsing mode is activated, all the different parts were enabled only when they were needed. There are four power pulsing lines in the SKIROC2 ASICs, analog, conversion, DAC and digital. The four of them can be disabled individually by shutting down the bias currents while the voltage is always on. One consequence of the power pulsing is that the ASIC needs some time to stabilize its current when it is switched on again. Therefore the ASICs have to be enabled before the bunch train arrives. During the test beam the delay was measured to be around 600 μs [52]. The ILC bunch train structure was simulated with a pulse generator with 1 % duty cycle.

Figure 5.28 shows the comparison of the pedestal position between the continuous current mode and the power pulsing mode. It shows that there is a shift of 2-3 uADC between the continuous current pedestal value and the power pulsing one for each channel, but that the distribution of the pedestal shift is broader in the case of the ASICs M2 and M4. In Figure 5.29 the noise of some channels of the detector is plotted versus the pad index, corresponding to the position of the channel in the detector volume. One this plot two consecutive layers with four ASICs each are shown. The blocks of points in red represent the different ASICs in the continuous current mode. One can recognize in red the noise pattern with a lower noise for the ASICs M1 and M3 and a higher one for the ASICs M2 and M4. In the power pulsing mode, in black, the pattern is not the same anymore. For the ASICs M1 and M3 the noise level stays the same in power pulsing mode, while for the two other ASICs the noise level is higher and less uniform in case of power pulsing mode. This behavior is not yet understood, but indicates that the problems already seen in the continuous mode for the ASICs M2 and M4 may be even amplified by the power pulsing mode. The fact that for the ASICs M1 and M3 the noise level stays the same gives confidence that, once the PCB routing is done properly, it should be the same for the ASICs M2 and M4.

For the MPV the situation is different because, if there is a correlation between the two powering modes for the ASICs M1 and M3, this is not the case for the ASICs M2 and M4 (see Figure 5.30). In Figure 5.30(a) the correlated band corresponds to the ASICs M1 and M3, while the points under this band, with a lower MIP position in the power pulsing mode, correspond to the ASICs M2 and M4. The others isolated points are due to a bad trigger threshold adjustment. The plot of the Figure 5.30(b) shows clearly the spread of the shift of the MIP position between the two powering modes for the channels of the ASICs M2 and M4.

Figure 5.31 shows once again that the behavior of the ASICs M2 and M4 is

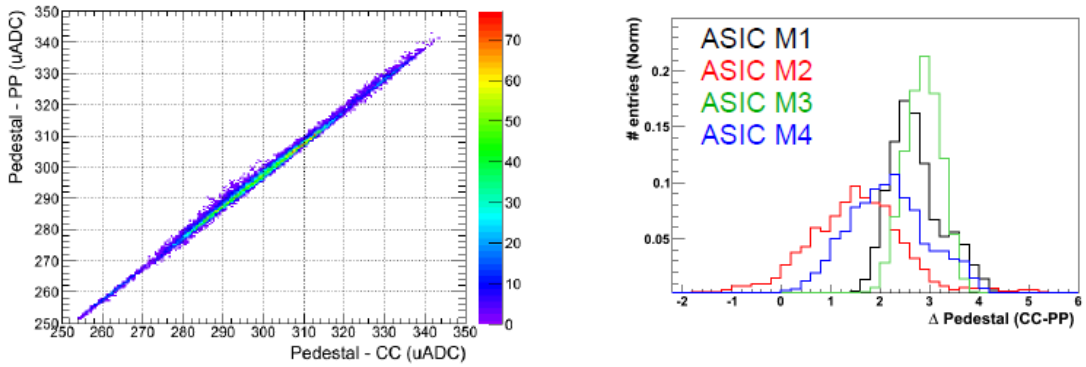

Figure 5.28: Left: correlation for the pedestal position between the two powering modes. Right: Difference of the pedestal position of the two powering modes for the four ASICs.

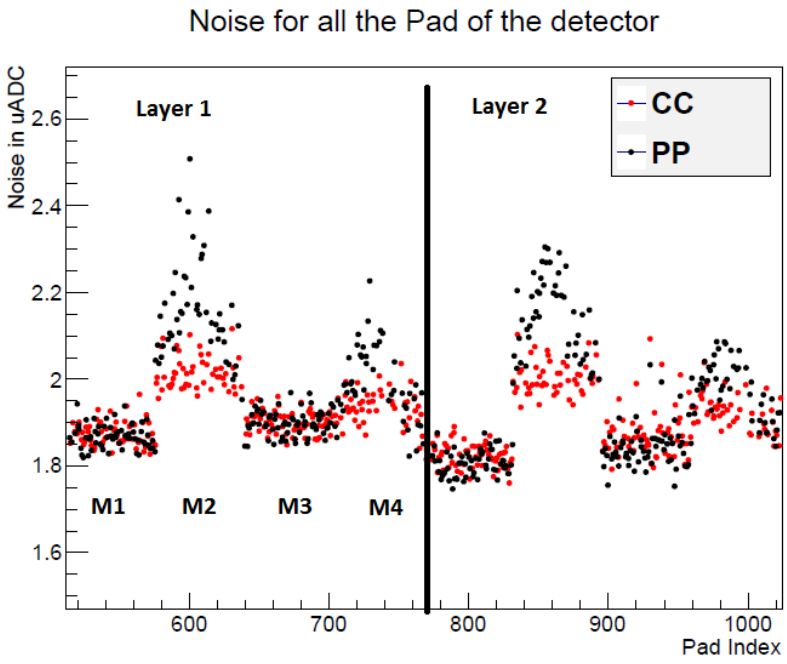

Figure 5.29: Noise of the channels of two layers of the detector in the two powering modes.

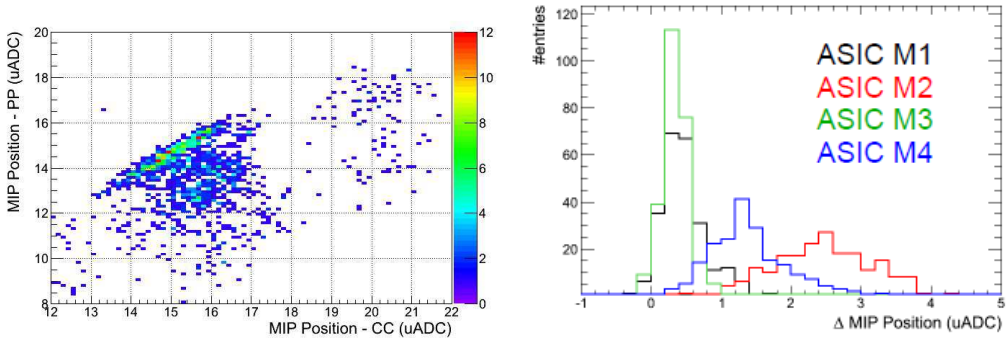

(a) (b)

Figure 5.30: (a) Correlation for the MIP position between the two powering modes. (b) Difference of the MIP position of the two powering modes for the four ASICs.

different with the power pulsing mode.

5.8 Conclusion

The first results of the SIW-ECAL technological prototype were very encouraging. The mean signal over noise ratio was above 10:1 for all preamplifier gains of the ASIC, even without the full trigger threshold adjustment capability. This value is to be compared with the *R&D* goal of 10:1, and also with the value of 7.5:1 achieved by the physics prototype under similar operating conditions. Further improvement can be expected once the noise sources that were identified in this analysis are eliminated. For example for the prototype, the excellent signal over noise ratio was compromised by too long connection lines on the interface card, a shortcoming that will be addressed in future versions of this card. A flaw of the current version of the SKIROC2 ASICs was the non-operational fine adjustment of the trigger thresholds. The individual channel trigger threshold adjustment and the improvement of the PCB routing are needed to reach 50% of the MIP position for all channels as required for the ECAL design.

The test of the power pulsing mode was also fruitful. From the behaviour of the ASICs M1 and M3 we learned that the power pulsing can work very well. But we also learned, from ASICs M2 and M4, that design details like the PCB routing play an important role for the power pulsing mode.

The next *R&D* step is to produce ASUs with four wafers read out by 16 ASICs. This step comprised the further studies of the PCB with respect to thickness and flatness. The deeper understanding of the SKIROC2 performance will result into

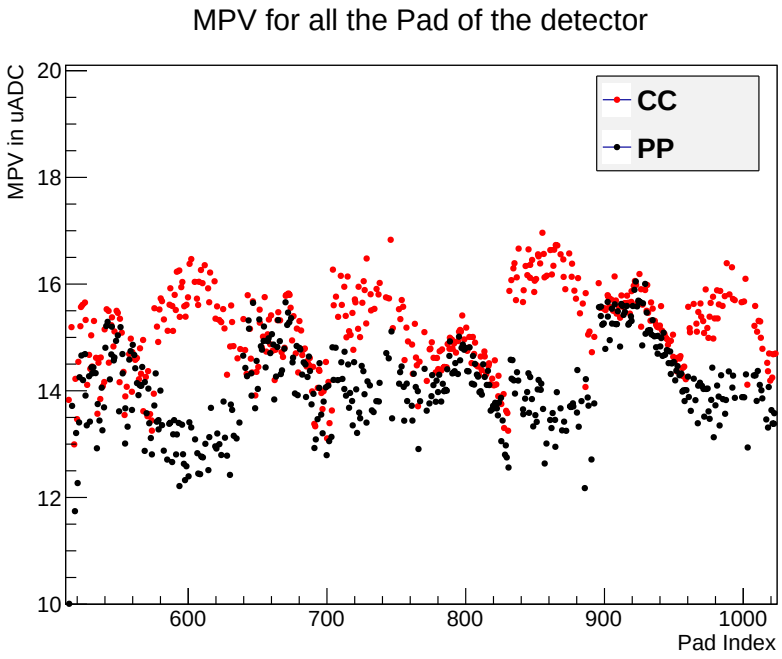

Figure 5.31: MIP position of the channels of two layers of the detector in the two powering modes. The separation between the layers and the ASICs is the same than in Figure 5.29.

a new development cycle of the ASIC (SKIROC2b). The length of ECAL detector modules will be up to 2.5 m, so such prototypes of long layers are going to be tested during 2014. Other test beams are also planned to continue to use some layers of the prototype in power pulsing mode. The $R\&D$ groups are now working to make possible the test of power pulsed layers place in a magnetic field in order to study the electrical and mechanical behavior.

Part III

Top Quark Production at the International Linear Collider

In this part of the thesis I will present the study of the top quark electroweak couplings at the ILC, via some observables like the forward backward asymmetry.

In Chapter 6 I will present the phenomenology of the top quark at the ILC. I will also present the different observable we are interested in, with some comparisons with the hadronic colliders. In Chapter 7 I will present the reconstruction methods for the semileptonic decay of the $t\bar{t}$ events. The reconstruction is done on generated events with the full simulation of the ILD detectors. In the Chapter 8 I will give the results of the analysis for the estimated accuracies on the top quark electroweak couplings.

Chapter 6

Phenomenology of the Top Quark at the ILC

As explained in the Section 1.4 the top quark is a very interesting component of the Standard Model because of its very high mass, comparable with the electromagnetic symmetry breaking scale. The electroweak couplings of the top quark are a good test of the Standard Model and could be a good probe to physics beyond the Standard Model. The goal of this study is to estimate the errors on the electroweak couplings that can be reached at the ILC. The study is carried out at $\sqrt{s} = 500\,\text{GeV}$ with an integrated luminosity of $500\,\text{fb}^{-1}$. In Chapter 2 we saw that the ILC will allow for polarized electron and positron beams, and so the t and $\bar{t}$ quarks oriented toward different angular regions in the detector will be enriched in left-handed or right-handed top quark helicity [53]. This means that it is possible to independently access to the left and right handed chiral parts of the top quark couplings to the Z^0 boson and the photon. To measure the six CP conserving form factors, F_{1V}, F_{1A} and F_{2V} for each helicity state, defined in Section 1.4, the analysis used the measurement of the cross section, the forward-backward asymmetry A_{FB}^t and the helicity asymmetry for two different polarization settings.

6.1 The Cross Section

6.1.1 $t\bar{t}$ Production with Polarized Beams

In case of polarized beams the form factors defined in Section 1.4 can be expressed in terms of the helicity of the incoming electrons [54]:

$$\begin{aligned} \mathcal{F}_{ij}^L &= -F_{ij}^\gamma + \left(\frac{-\frac{1}{2}+\sin\theta_W{}^2}{\cos\theta_W \sin\theta_W}\right)\left(\frac{s}{s-m_Z^2}\right) F_{ij}^Z \\ \mathcal{F}_{ij}^R &= -F_{ij}^\gamma + \left(\frac{\sin\theta_W{}^2}{\cos\theta_W \sin\theta_W}\right)\left(\frac{s}{s-m_{Z^0}^2}\right) F_{ij}^Z \end{aligned} \tag{6.1}$$

where $i = 1, 2$ and $j = V, A$. So measuring both $\mathcal{F}_{ij}$ factors with polarised beams will give access to the F_{ij} form factors. The cross section for $t\bar{t}$ production for electron beam polarization $I = L, R$ can then be derived in terms of these new form factors:

$$\sigma_I = 2\left(\frac{4\pi\alpha^2}{3s}\right) N_c\beta\left[(1+0.5\gamma^{-2})(\mathcal{F}_{1V}^I)^2 + (\beta\mathcal{F}_{1A}^I)^2 + 3\mathcal{F}_{1V}^I\mathcal{F}_{2V}^I\right] \tag{6.2}$$

where α is the electromagnetic running constant, N_c the number of quark colours, and γ and β the Lorentz factor and the velocity, respectively.

Like the ILC beams will not be fully polarized the cross section of the $t\bar{t}$ should be expressed for a given polarization of the electrons, $\mathcal{P}$ and of the positrons $\mathcal{P}'$. The cross section of any channel at the ILC in case of polarized beams reads [55]:

$$\sigma_{\mathcal{P},\mathcal{P}'} = \frac{1}{4}\left[(1-\mathcal{P}\mathcal{P}')(\sigma_{L,R}+\sigma_{R,L}) + (\mathcal{P}-\mathcal{P}')(\sigma_{R,L}-\sigma_{L,R})\right] \tag{6.3}$$

where the indices L and R indicate full polarization of the incoming beams with electrons and positrons of left-handed or right-handed helicity, respectively. The configurations $\sigma_{R,R}$ and $\sigma_{L,L}$ can be neglected due to helicity conservation at the electron vertex in the high energy limit, $m_e/E \to 0$, valid here since $E = 250\,\text{GeV}$.

The unpolarized cross section for Standard Model processes are shown in Figure 6.1 for different center of mass energies . The cross sections at the Born level of the signal process and the main Standard Model background processes at a center of mass energy of 500 GeV are then summarized in Table 6.1.

Channel	$\sigma_{unpol.}$ (fb)	$\sigma_{L,R}$ (fb)	$\sigma_{R,L}$ (fb)
$t\bar{t}$	572	1564	724
$\mu\mu$	456	969	854
$uu + cc + ss + dd$	2208	6032	2793
$b\bar{b}$	372	1212	276
γZ^0	11185	25500	19126
WW	6603	26000	150
Z^0Z^0	422	1106	582
Z^0WW	40	151	8.7
$Z^0Z^0Z^0$	1.1	3.2	1.22

Table 6.1: Unpolarized cross-sections and cross-sections at the Born level for 100 % beam polarization for signal and background processes.

Table 6.1 shows that the $t\bar{t}$ production is highly dependent on the polarization of the electrons and positrons beams. Also the Standard Model background

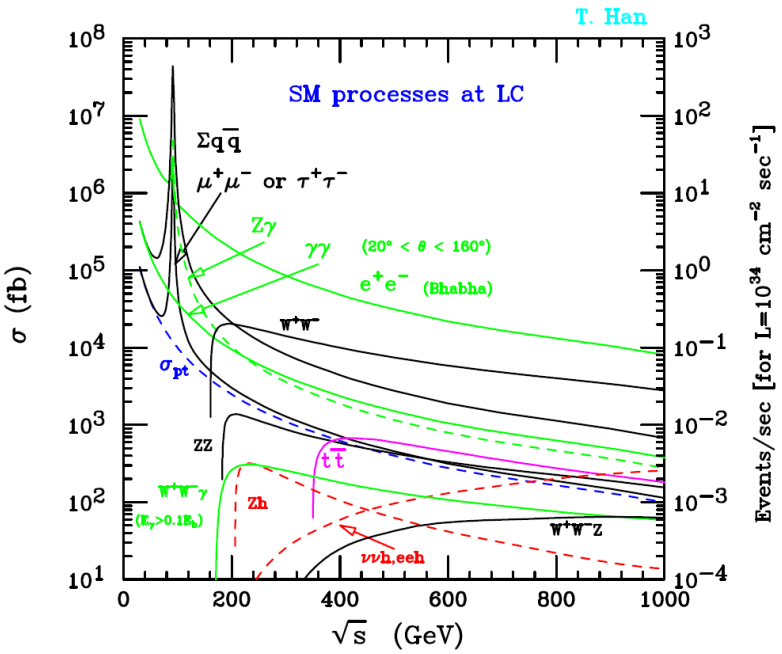

Figure 6.1: Cross sections of Standard Model processes at the ILC as a function of the energy in the center of mass $\sqrt{s}$.

contamination is not the same depending on the initial polarizations.

6.1.2 The Signal

For the final state of the $t\bar{t}$ production the fact that the $W^{\pm}$ bosons can decay either to light quarks (u,d,c,s) or to leptons leads to the following classification for the $t\bar{t}$ event decay:

- the fully hadronic decay: $t\bar{t} \to bq\bar{q}bq\bar{q}$ (46.2 % of the events).
- the semi leptonic decay: $t\bar{t} \to bq\bar{q}bl\nu_l$ (43.5 % of the events).
- the fully leptonic decay: $t\bar{t} \to bl^-\bar{\nu}_l bl^+\nu_l$ (10.3 % of the events).

The signal that we are interested here is the semi leptonic decay. The final state consists of four jets, including two b quark jets, one isolated lepton and missing energy carried away by the neutrino. We choose the semi-leptonic decay because this specific final state is very useful to isolate the signal, even from the background with a high cross section. The cross section is of the same order than the fully hadronic one but the presence of the lepton is an advantage to isolate the signal and to caracterize this one.

The Figure 6.1 shows that the $t\bar{t}$ production starts at 350 GeV, but we choose to work at 500 GeV to have a relatively high cross section and to be far enough

from the $t\bar{t}$ threshold effects.

6.1.3 The Standard Model Background

The cross sections of some of the main physical processes at the ILC which can be considered as background for the $t\bar{t}$ production are given in Table 6.1. The background should be removed as much as possible by the analysis procedure. To do so the final states of the background should be compared with the one of the signal to see how they can be distinguished.

The main background of the semi leptonic $t\bar{t}$ production analysis are the other decay mode of the top quark. All those modes have two b quarks in the final state and the separation is done on the isolated leptons. For the fully hadronic final state this could come from the contaminations of not isolated leptons, coming for example from bottom mesons decaying into a charged lepton plus additional particles. However they should be embedded in a jet rather than isolated like the lepton of the top decay. For the fully leptonic decay the situation seems to be clear with two isolated leptons and no other jet than the two b ones. But it may happen that only one lepton is found because for example of a tau lepton decaying hadronically. In these cases, the higher missing energy will lead to find incoherent W and top masses, to reject these events.

In the case of a left-handed electron beam, the single top production in association with a W boson and b quark leads to the same final state as top quark pair production and can't be easily separated from the signal.

The W pair background is the typical example of a background with a very different final state, but like its cross section is much larger than the one of the top pair production, it may contaminate a lot the samples. Its cross section is ten times higher than the one of the $t\bar{t}$ production so it has to be strongly suppressed, since any contamination at the 1 % level leads to 10 % impurities in the top events selected. Like for $t\bar{t}$, its semi-leptonic final state contains a lepton from a W boson but it can be strongly reduced, thanks to the absence of the two b jets.

The other backgrounds are much lower and can easily be removed. For example the $b\bar{b}$ channel can be removed by its simple topologies and the absence of an isolated lepton. The Z^0WW background with $Z^0 \to b\bar{b}$, has exactly the same final state than the semi leptonic $t\bar{t}$ production, but like the mass of the $b\bar{b}$ system is the one of the Z^0 boson it is easily identified.

6.2 The Forward Backward Asymmetry

The forward backward asymmetry, A^t_{FB}, counts the difference in the number of events in the two hemispheres of the detector and is defined by:

$$A_{FB}^{t} = \frac{\sigma(\cos\theta_t > 0) - \sigma(\cos\theta_t < 0)}{\sigma(\cos\theta_t > 0) + \sigma(\cos\theta_t < 0)} \tag{6.4}$$

with θ_t the top polar angle with respect to the initial direction of the electron beam. This measurement requires to know the charge of the top quark because an anti-top will have the opposite asymmetry than a top quark. In the semi-leptonic decay the charge of the quark is deduced from the lepton charge. To gain in statistics, a forward anti-top $\bar{t}$ (with $\cos\theta_{\bar{t}} > 0$) is changed into a backward top ($\cos\theta_t < 0$), and vice versa, by changing the sign of its $\cos\theta_{\bar{t}}$.

6.2.1 A_{FB}^{t} at Hadronic Machines

The top quark was discovered by the Tevatron experiments CDF and D0 [19][20]. These were also the first experiments to measure the forward backward asymmetry of the top quark. In hadronic collisions, there is a lot of background and it is much more difficult to measure the charge of a vertex. So the analyses at the Tevatron and at the LHC, are only possible for the semi-leptonic channel, where the identification of an isolated lepton is much easier. The average asymmetry reported by CDF is $0.201 \pm 0.065(\text{stat.}) \pm 0.018(\text{syst.})$ [56] and by D0 $0.196 \pm 0.060(\text{stat.})^{+0.018}_{-0.026}(\text{syst.})$ [57] are in agreement with each other. But if we compare these values with an asymmetry of about 0.07 predicted by the Standard Model from NLO QCD and electroweak effects it shows tensions with Standard Model predictions for the A_{FB} of the top quark.

The theoretical interpretation of this tension with the Standard Model in the top quark asymmetries is unclear. Many beyond the Standard Model theories predict effects in top quark physics, but it is also possible that the tension between theory and experiment can be resolved by more accurate QCD calculation.

Not like the Tevatron, which was a proton anti-proton collider, the LHC is a symmetric machine, a proton-proton collider, so the two hemispheres are intrinsically symmetric. Indeed, at the LHC at 7 TeV, only 15 % of the interactions arise from $q\bar{q}$ collisions, the other 85 %, from gg collisions, can have no intrinsic asymmetry. Still, in $q\bar{q}$ collisions at the LHC, it is likely that the q is a valence quark while the $\bar{q}$ is pulled from the sea. This implies that $t\bar{t}$ pairs produced in $q\bar{q}$ collisions are typically boosted into the direction of the q. This offers an alternative method to observe a forward backward asymmetry in $q\bar{q} \to t\bar{t}$, via a smaller asymmetry, called charge asymmetry, A_C in the variable $\delta|y| = |y_t| - |y_{\bar{t}}|$, where y is the rapidity. For this observable, CMS measures $A_C = 0.004 \pm 0.010(\text{stat.}) \pm 0.011(\text{syst.})$ [58] , which agrees with the Standard Model predictions within the relatively large uncertainties.

6.2.2 A^t_{FB} at the ILC

At the ILC it is possible to measure the forward backward asymmetry in both the semi-leptonic and in the fully hadronic channel thanks to the very clean environment. The fully hadronic channel has been treated in a second analysis. Thanks to the polarization capability of the ILC beams it is also possible to measure to different A^t_{FB} depending on the helicity of the electron beam. The forward backward asymmetry can be expressed in terms of the form factors defined in Equation 6.1:

$$(A^t_{FB})_I = \frac{-3\beta\mathcal{F}^I_{1A}(\mathcal{F}^I_{1V} + \mathcal{F}^I_{2V})}{2\left[(1+0.5\gamma^{-2})(\mathcal{F}^I_{1V})^2 + (\beta\mathcal{F}^I_{1A})^2 + 3\mathcal{F}^I_{1V}\mathcal{F}^I_{2V}\right]} \tag{6.5}$$

where I = L or R depending on the polarization of the incoming electron beam. The equation can be factorized by $\mathcal{F}^I_{1A}$, showing the importance of the A^t_{FB} measurement to get a good precision on this factor. In the Standard Model the two forward backward asymmetries take the values:

$$(A^t_{FB})_L = 0.38 \quad ; \quad (A^t_{FB})_R = 0.47 \tag{6.6}$$

6.3 The Helicity Asymmetry

The fraction of right-handed tops is given by the following expression:

$$(F_R)_I = \frac{(\mathcal{F}^I_{1V})^2(1+0.5\gamma^{-2}) + (\beta\mathcal{F}^I_{1A})^2 + 2\beta\mathcal{F}^I_{1V}\mathcal{F}^I_{1A} + \mathcal{F}^I_{2V}(3\mathcal{F}^I_{1V} + 2\beta\mathcal{F}^I_{1A}) - \beta\mathcal{F}^I_{1V}\Re(\mathcal{F}^I_{2A})}{2\left[(1+0.5\gamma^{-2})(\mathcal{F}^I_{1V})^2 + (\beta\mathcal{F}^I_{1A})^2 + 3\mathcal{F}^I_{1V}\mathcal{F}^I_{2V}\right]} \tag{6.7}$$

The fraction of right-handed tops is proportional to the form factors, so it gives another observable to access to the form factors. To measure the fraction of right-handed top we used the distribution of the helicity angle. In the rest frame of the top quark the helicity angle is the angle between lepton and the W boson. The slope of the distribution of the angle is proportional to the fraction of right-handed top via [59]:

$$\frac{1}{\Gamma}\frac{d\Gamma}{d\cos\theta_{hel}} = \frac{1+\lambda_t\cos\theta_{hel}}{2} = \frac{1}{2} + (2F_R - 1)\frac{\cos\theta_{hel}}{2} \tag{6.8}$$

where $\lambda_t = 1$ for t_R and $\lambda_t = -1$ for t_L. In practice there will be a mixture of the two helicities left and right and λ_t will have a value between -1 and 1 depending on the composition of the top quark sample and therefor on the polarization of the incoming beams. In the Standard Model the expected values are $(F_R)_L = 0.25$ and $(F_R)_R = 0.76$.

The Equation 6.7 contains also a CP violating term proportional to $\Re(\mathcal{F}_2 A^I)$ which can be precisely estimated using CP violating observables. These observables will be discussed later on, see Appendix B.

6.4 Event Generation

Signal and background events are generated with version 1.95 of the WHIZARD Monte Carlo event generator [60][61]. The events are classifed by the number of fermions in the final state, which means six for the signal, and two and four in the case of the Standard Model background. The most relevant background contributions are the fully hadronic and fully leptonic decays of $t\bar{t}$ pairs and the WW and $b\bar{b}$ final states. The generated events are then passed to the PYTHIA [62] simulation program to generate parton showers and subsequent hadronisation. In the case of the six fermions final states the events are flagged when the difference between the invariant masses of the three fermion systems forming a top from WHIZARD and the input top mass to WHIZARD of 174 GeV is smaller than $5\Gamma_t$, where $\Gamma_t = 1.5\,\text{GeV}$ is the total decay width of the top quark. But by this way only about 70 % of the events generated by WHIZARD are recognized as $t\bar{t}$ events and treated accordingly by PYTHIA. The different hadronisation of genuine $t\bar{t}$ events may introduce a systematic uncertainty, which will have to be estimated at a later stage, but the first check with the new WHIZARD version shows that it can be expected to be reasonably small.

The study has been carried out on a fully polarized sample, while the realistic values of the beam polarizations at the ILC at $\sqrt{s} = 500\,\text{GeV}$ are $\mathcal{P}, \mathcal{P}' = \pm 0.8, \mp 0.3$. This implies that the cross section and therefore its uncertainty has to be scaled with the polarization according to Equation 6.3. The observables A_{FB}^t and λ_t vary only very mildly with the beam polarization [63], but here again, the reduced cross section leads to a higher statistical error for non-fully polarized beams, and will be correctly taken into account in the uncertainty of the results.

Events corresponding to a luminosity of $250\,\text{fb}^{-1}$ for each of the polarization configurations were subject to a full simulation of the ILD detector within Mokka and subsequent event reconstruction using the version ILD_o1_v05 of the ILC software. All the ILD sub-detectors, described in Chapter 3, have been implemented in Mokka including as much as possible the engineering details, like the electronics, cabling and mechanical support. In the version ILD_o1_v05 of the Mokka models the ILD detector is simulated with the analogue HCAL and the SiW-ECAL.

6.5 Some Beyond the Standard Model Predictions

The Higgs field was introduced in the Standard Model (see Section 1.3) to generate the masses of gauge bosons and fermions, but an explanation for the masses hierarchy is still to be found. To solve this issue an extension of the Standard Model was proposed in 1999 by L. Randall and R. Sundrum [64]. By adding one space dimension with a so-called warped metric, it is possible to accommodate the bosonic hierarchies, and the fermionic hierarchy, from the Planck mass, down to the electroweak scale. In the original model of Randall-Sundrum there are additional massive gauge bosons in that assumed extra dimension. The model predicts increased couplings of the top quark, and perhaps also the b quark, to these Kaluza Klein particles. Randall Sundrum models also have the advantage to be able to fit the two anomalies observed in the forward backward asymmetry for b quarks, $A_{FB}^{0,b}$ at LEP1 (see Figure [**?**]) and for top quarks at the Tevatron (see Section 6.2.1) [65][66].

Various models implement the idea of Randall-Sundrum, like those by Djouadi [65], Hosotani [67], Gherghetta [68], Carena [69], Grojean [70]. All these models entail deviations from the Standard Model values of the top quark couplings to the Z^0 boson that will be measurable at the ILC. Figure 6.2 [71] shows the predictions for these deviations of the left and right couplings in these models.

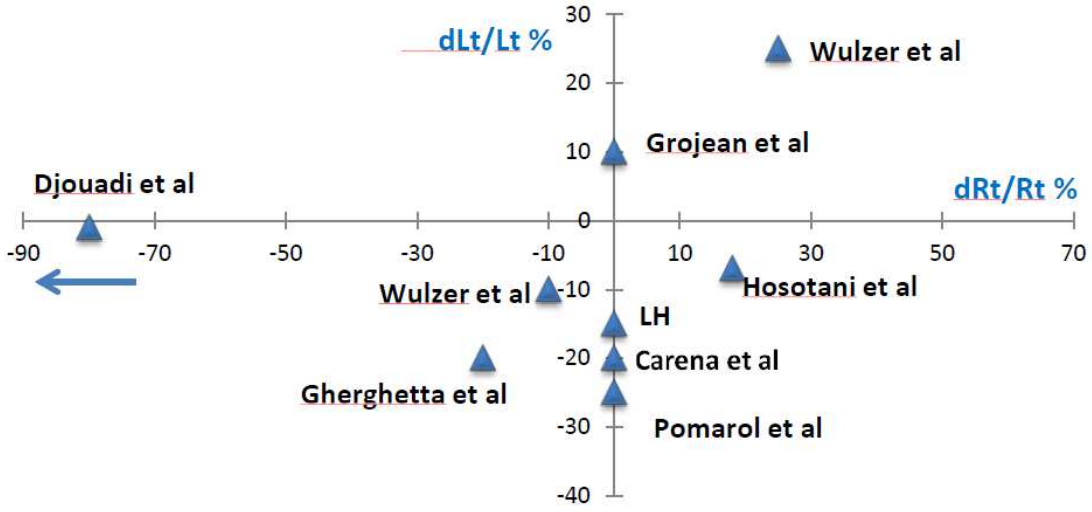

Figure 6.2: Plot showing the predicted deviations of Z^0 couplings to t_L and t_R in %. The Djouadi *et al.* prediction falls outside of the scale.

This picture clearly demonstrates the importance of the capability of the ILC to separate the $t\bar{t}Z$ couplings into their left and right components thanks to the

polarized beams. A precision at the per-cent level on both couplings would allow to separate among them unambiguously. This is a unique feature of the ILC because, from the $t\bar{t}Z$ cross section measurable at LHC one cannot separate L and R components and the accuracy is limited to the 10 % level [72].

Chapter 7

Analysis of the Semi-Leptonic Channel of $t\bar{t}$ Events

The goal of the analysis of the semi-leptonic channel of the $t\bar{t}$ events is to separate as much as possible signal event from the Standard Model background while preserving a high selection efficiency for the signal events. To do so the analysis used the main characteristics of the topology of the signal final state. The most important points are the presence of an isolated lepton and of two b jets in the signal final state. Another aspect of the analysis is the presence in the samples, at small angles, of background generated by beam beam interactions, so-called the $\gamma\gamma \to hadrons$ background.

7.1 Lepton Finder

The first step of the analysis is to identify an isolated lepton in the event. For that we used the LAL Lepton Finder described in [41]. The principle of the LAL Lepton Finder is to take advantage of the particular decay kinematic of the lepton. Indeed the lepton from the W boson decay is either the most energetic particle in a jet or has a sizeable transverse momentum with respect to neighboured jets. To identify these kind of leptons the jet clustering algorithm is forced to form four jets and the lepton is identified inside one of the jets with the following variables:

$$x_T = \frac{p_{T,\text{lepton}}}{m_{\text{jet}}} \tag{7.1}$$

where $p_{T,\text{lepton}}$ is the transverse momentum of the identified lepton with respect to its jet and m_{jet} is the mass of the jet, for the case of lepton with a sizeable transverse momentum as illustrated in Figure 7.1(a), and:

$$z = \frac{E_{\text{lepton}}}{E_{\text{jet}}} \tag{7.2}$$

which corresponds to the fraction of the energy of the lepton in the jet in the case of a leading lepton as illustrated in Figure 7.1(b).

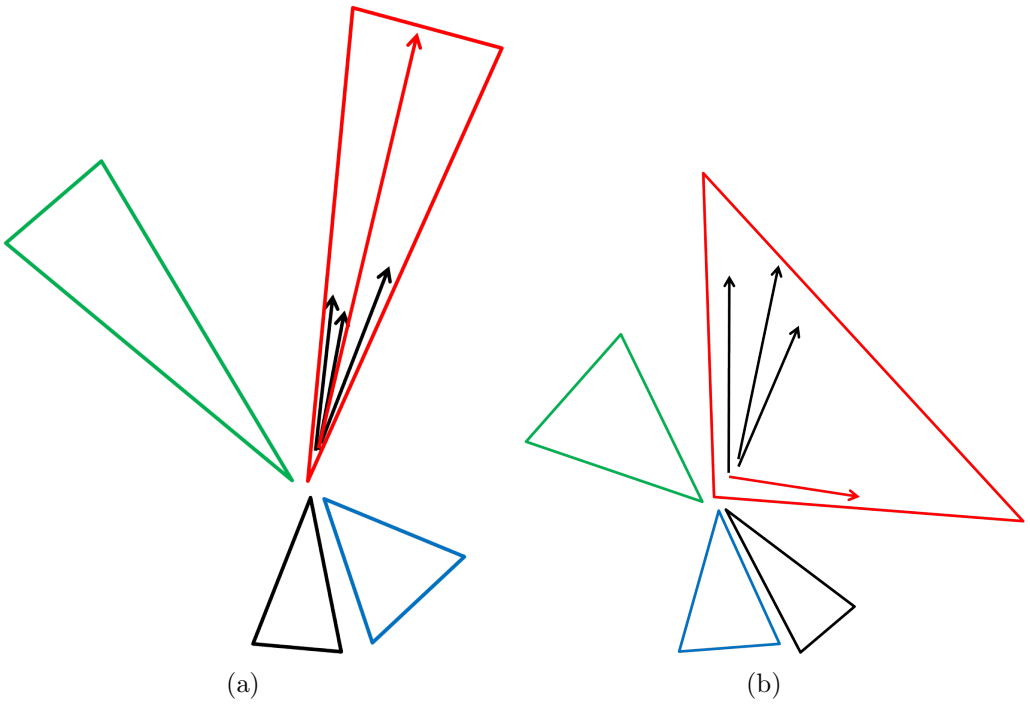

(a) (b)

Figure 7.1: The two cases for an isolated leptons (red arrow) from semi-leptonic decay after creating four jets (triangles): (a) Definition of a leading lepton in a jet. (b) Definition of a lepton with large transverse momentum with respect to the axis of the jet.

The lepton finder identified electrons and muons with an energy higher than 5 GeV. The samples with tau leptons are also included in the analysis to identified them in the case of a leptonic decay of the tau. The distribution of the two variables is shown in Figure 7.2 for leptons in semi-leptonic and fully hadronic $t\bar{t}$ events.

The leptons present in the fully hadronic top channel are mainly coming from the decays of B mesons, and are not isolated as illustrated on Figure 7.2. To select only isolated leptons the following isolation criteria has been chosen:

$$x_T > 0.25 \text{ or } z > 0.6 \tag{7.3}$$

The decay lepton in case of e and μ can be identified with an efficiency of about 85 %, where the selection has a tendency to reject low momentum leptons. The τ

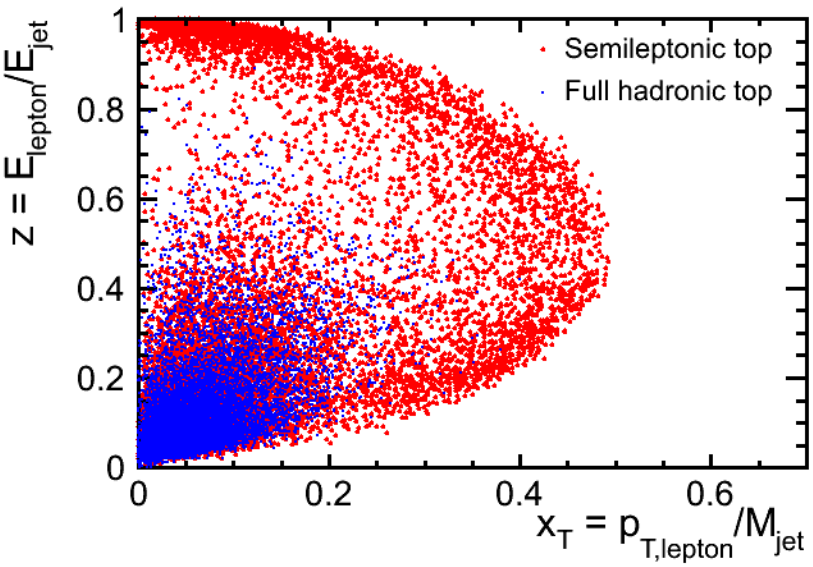

Figure 7.2: Distribution of the isolation variables for leptons from semi-leptonic, in red, and fully hadronic, in blue, $t\bar{t}$ events.

leptons decay into e or μ, which are collinear with the produced τ but have lower momentum than primary decay leptons. Taking into account the τ leptons, the efficiency to identify the decay lepton is about 70 %.

7.2 $\gamma\gamma \rightarrow hadrons$ Background

An important source of background overlay is the processes known collectively as multi-peripheral $\gamma\gamma \rightarrow hadrons$ events. These types of events yield to a small number of additional particles, typically 1.7 low-multiplicity events per bunch crossing for the ILC at 500 GeV [28]. Particles from $\gamma\gamma \rightarrow hadrons$ have a polar angle distribution markedly forward and tend to be hard enough to reach the outer layers of the detector and affect the overall detector performance, in particular jet reconstruction. These particles are similar to beam remnants as present in hadron collisions. It is therefore intuitive to employ a jet algorithm used in hadron collisions that separate the beam jet from the hard interaction. In the present study the best results are obtained with the the longitudinally invariant k_t algorithm [73]. This is demonstrated in Figure 7.3. The Figure shows the reconstructed polar angle distribution of the hadronically decaying W boson from $t\bar{t}$ pairs compared with the generated distribution. The result is shown for the "traditional" Durham algorithm [74] and for the longitudinally invariant k_t algorithm

with a jet radius of $R = 1.5$. The improvement achieved by the longitudinally invariant k_t algorithm is obvious. After the removal of the hadrons background the event is processed further by the Durham algorithm. Further beam induced background such as electron-positron pairs have not been studied in the present article but a detailed study presented in [75] demonstrates that the induced number of background hits in the vertex detector and the TPC as well as the related neutron fluxes are uncritical for the detector performance.

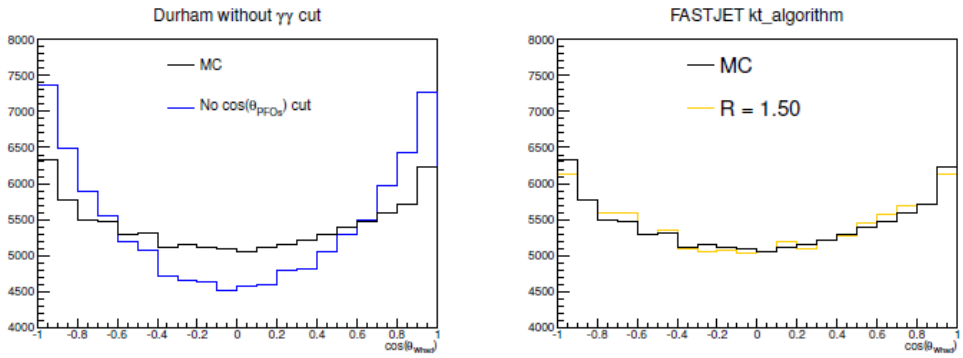

(a) Durham (b) k_t, $R = 1.5$

Figure 7.3: The polar angle distribution of the hadronically decaying W boson for two different jet algorithms with the $\gamma\gamma \rightarrow hadrons$ background.

7.3 B-tagging

The presence of two b jets in the final state of the semi-leptonic channel of the $t\bar{t}$ events is the second important characteristic of the signal. So the b jets identification capability of the ILD is an essential feature for the analysis. A detailed study has been done in [41] for the LOI, and the goal here was mainly to check the results with the new simulation of the ILD detectors and the new package LCFIPlus.

7.3.1 The LCFIPlus Package

LCFIPlus[76] is a software package of Marlin targeted for multi-jet events and used in the reconstruction for the vertexing, flavour tagging, vertex charge reconstruction and the jet reconstruction. It is based on the LCFIVertex [77] software package which had been developed in the context of the LOI for vertexing, flavour

tagging and vertex charge reconstruction with an ILC vertex detector. LCFIVertex was originally developed for Z-pole physics and designed to find the vertex and tag the flavour of a jet, thus its algorithm was applied after reconstruction of a jet in an event. On the opposite in LCFIPlus, the vertices in an event are reconstructed before jet reconstruction so as to use the vertex information for jet reconstruction. The flavour tagging is made with the help of TMVA (Toolkit for Multivariate Data Analysis with ROOT) and in addition to the standard variables, user specific variables for tagging can be easily introduced depending on the needs for the analysis.

The primary and secondary, when available, vertices are reconstructed using the track information of the detectors and a χ^2 minimization. The tracks with a low p_t are removed and the sum of the charge of the remaining tracks is used to measure the charge of the vertex. Informations like the number of tracks, the impact parameter or the decay length are then used in a neural network to give the b-likeness or b-tag. The b-tag is a value between 0 and 1 which gives the probability for the jet linked to this vertex to be a b jet or not. Finally a jet clustering is done and the different jets are linked to their vertex. The standard jet algorithm is the Durham one, but it is possible to use another jet algorithm, for example to reject the $\gamma\gamma \to hadrons$ background.

7.3.2 Results

For the semi-leptonic analysis we have done the trainning of the neural network of the flavour tagging on 4 jets samples at 500 GeV. The trainning of the TMVA was done on 4b/4c/4q samples but also on 2 and 6 jets samples at different center of mass energies. Studies have shown [76] that the b-tag performances are more affect by the number of quarks than by the energy in the weight files. So latter on we used the DBD standard weight files for 6 jets at 500 GeV. Figure 7.4 shows the value of the b-tag for different jets with respect to the polar angle of the jet. For the jets with the higher b-tag, the value is typically 0.92 while the second highest one is still around 0.65. Both values are clearly distinct from those obtained for jets from light quarks, where the b-tag value is around 0.14. These values are nearly independent of the polar angle of the jet but drop towards the acceptance limits of the detector. This clear separation in the b-tag value shows that the detector and software performance allows for a good identification of the b jets of the events.

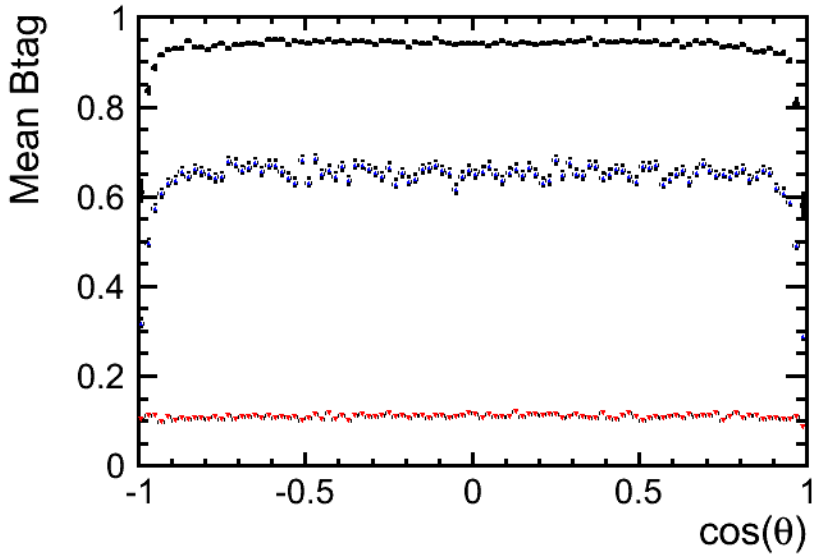

Figure 7.4: The b-tag values as a function of the polar angle of the jets. The two highest b-tag values (black and blue dots) are associated to b quark jets. The third set of values (red dots) is obtained for jets from light quarks.

7.4 Top Reconstruction and Background Rejection

The last step of the $t\bar{t}$ event reconstruction, once the isolated lepton and the two b jets are found, is to associate one of the two b jets with the two remaining jets. These two remaining jets are the ones coming from the W bosons which had decayed hadronically. To choose the best combination of the b jets and the W boson one tests the two possibilities and selects the one that minimizes the following criteria:

$$d^2 = \left(\frac{m_{\text{cand.}} - m_t}{\sigma_{m_t}}\right)^2 + \left(\frac{E_{\text{cand.}} - E_{\text{beam}}}{\sigma_{E_{\text{beam}}}}\right)^2 + \left(\frac{p_b^* - 68}{\sigma_{p_b^*}}\right)^2 + \left(\frac{\cos\theta_{bW} - 0.23}{\sigma_{\cos\theta_{bW}}}\right)^2 \tag{7.4}$$

where $m_{\text{cand.}}$ and $E_{\text{cand.}}$ are the invariant mass and the energy of the top quark candidate decaying hadronically, respectively, and m_t and E_{beam} the input top mass of 174 GeV and the beam energy of 250 GeV. The two last variables are the momentum of the b quark in the centre-of-mass frame of the top quark, p_b^* (see Equation 7.5 and Figure 7.5), which should take the value of 68 GeV, and the angle between the b quark and the W boson (see Figure 7.6). The measured

values are compared with the expected ones and the denominator is the width of the measured distributions.

$$p_b^* = p_W^* = \frac{\left[(m_t^2 - (m_b + m_W)^2)\,(m_t^2 - (m_b - m_W)^2)\right]^{1/2}}{2m_t} = 68\,\text{GeV} \qquad (7.5)$$

The results of the reconstruction are one top quark candidate decaying hadronically and on the other side one isolated lepton whose charge gives the sign of the top quark decaying leptonically. To illustrate the reconstruction the mass distribution of the top quark candidates is shown on Figure 7.7.

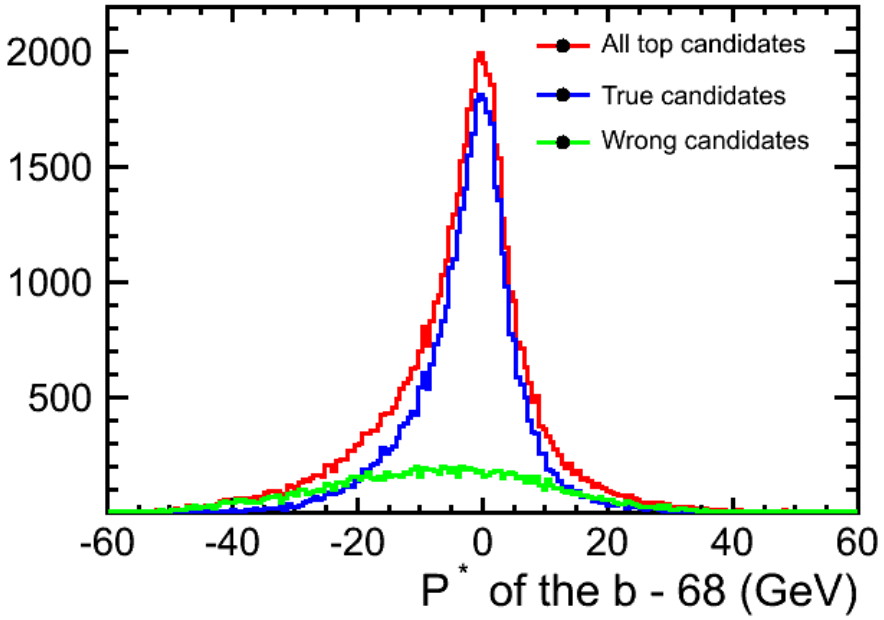

Figure 7.5: Distribution of the p_b^* of the reconstructed top quark candidates decaying hadronically. The true and wrong flags are based on the Monte Carlo informations.

The Standard Model background rejection has been studied in detail in [41] for the LOI. The same cuts were used for the DBD simulation and the results are summarized in table 7.1:

The table 7.1 shows the results of the signal and background cut efficiency for the left-handed electron beam polarisation, $\mathcal{P}, \mathcal{P}' = -0.8, +0.3$. The entire selection retains 54.4 % signal events for this configuration and 55.9 % for the right-handed electron beam polarisation configuration, $\mathcal{P}, \mathcal{P}' = +0.8, -0.3$. The

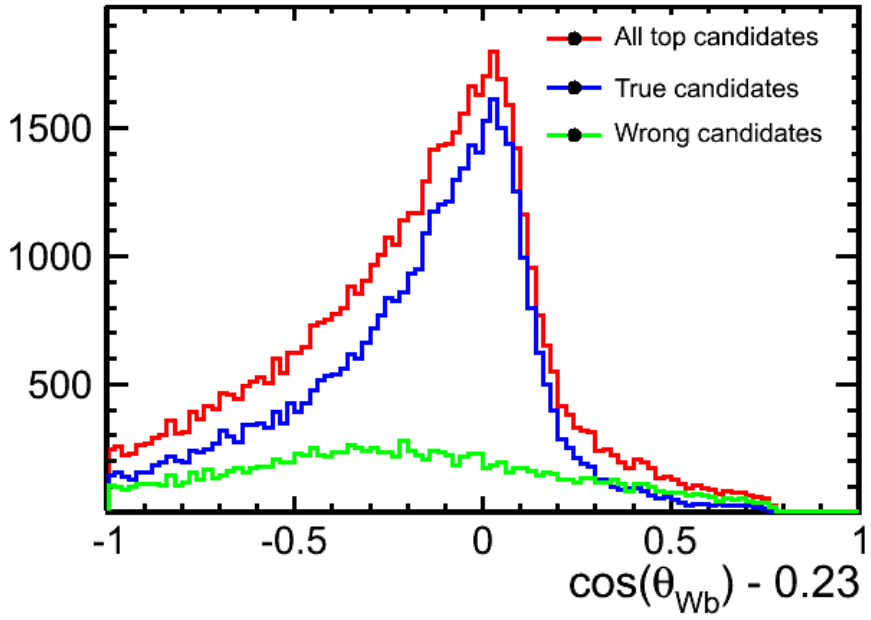

Figure 7.6: Distribution of the angle between the b quark and the W boson of the reconstructed top quark candidates decaying hadronically. The true and wrong flags are based on the Monte Carlo informations.

Process	$t\bar{t}$ Semi-Lep.	$t\bar{t}$ Fully-Lep.	$t\bar{t}$ Fully-Had.	WW Semi-Lep.	bb
Sigma (fb)	409.02	96.85	434.41	6618.63	718.0
Factor for $\mathcal{L} = 250\,\text{fb}^{-1}$	0.99	0.868	1.08	3.74	0.64
Initial Numbers	102255(100 %)	24212(100 %)	108602(100 %)	1654657(100 %)	179520(1
Nb lepton = 1	68510(67 %)	9685(40 %)	3422(3.15 %)	986684(59.6 %)	17126(9.
$b - tag_1 > 0.8 or b - tag_2 > 0.3$	62354(61 %)	8853(36.6 %)	2953(2.72 %)	20234(1.22 %)	13231(7.
Thrust < 0.9	61901(60.5 %)	8450(34.9 %)	2948(2.72 %)	3247(0.196 %)	1840(1.0
Hadronic mass	60688(59.4 %)	5228(21.6 %)	2205(2.03 %)	1438(0.0869 %)	512(0.28
m_W and m_t	55637(54.4 %)	2498(10.3 %)	1809(1.67 %)	698(0.0422 %)	284(0.15

Table 7.1: Efficiency of the different cuts for the signal and the background for the left-handed electron beam polarisation.

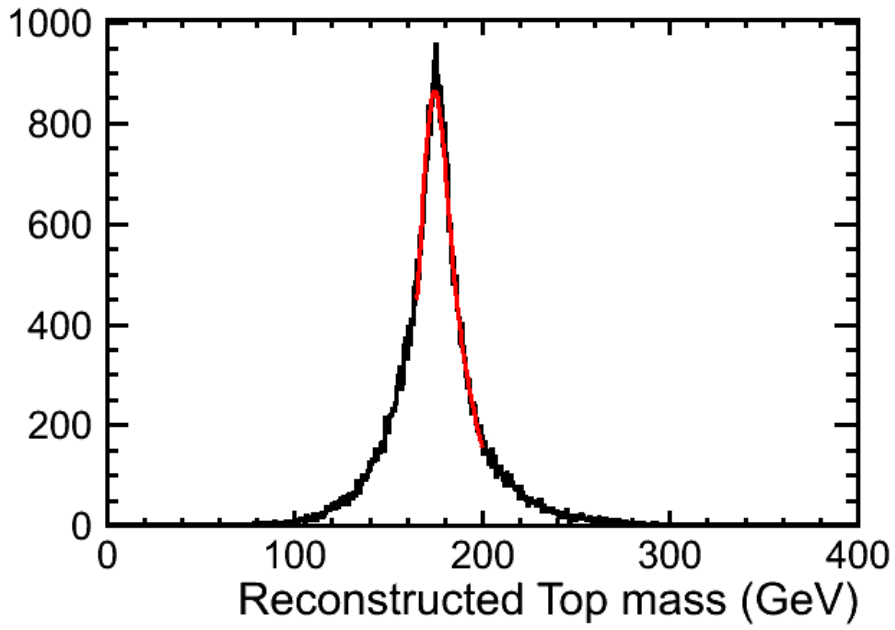

Figure 7.7: Distribution of the mass of the top quark candidates decaying hadronically.

fraction of distinguishable background events in the final sample is between 7.2 % for $\mathcal{P}, \mathcal{P}' = +0.8, -0.3$ and 9 % for $\mathcal{P}, \mathcal{P}' = -0.8, +0.3$. This background is predominantly composed of events from non-semileptonic decays of the $t\bar{t}$ events.

7.5 The Forward Backward Asymmetry

For the determination of the forward backward asymmetry A^t_{FB}, the number of events in both hemispheres of the detector with respect to the polar angle θ_t of the top quark are counted:

$$A^t_{FB} = \frac{N(\cos\theta_t > 0) - N(\cos\theta_t < 0)}{N(\cos\theta_t > 0) + N(\cos\theta_t < 0)} \tag{7.6}$$

In the analysis, the polar angle of the top quark is calculated from the decay products in the hadronic decay branch. In the case of a reconstructed anti-top quark, its polar angle is changed form $\theta_{\bar{t}}$ to $\theta_{\bar{t}}+\pi$ to come back to the top quark case. The analysis is carried out separately for a left-handed polarised electron beam and for a right handed polarised beam. The distribution for both polarisations of the electron beam is shown in Figure 7.8 for generator and reconstructed events.

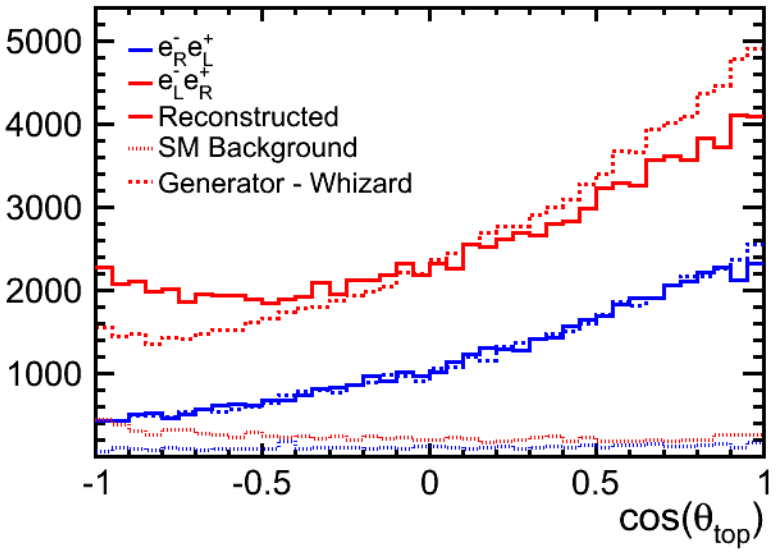

Figure 7.8: Reconstructed forward backward asymmetry compared with the prediction by the event generator WHIZARD for two configurations of the beam polarisations.

The reconstructed distribution of the polar angles of the top quark in the case of right-handed electron beams, in blue on Figure 7.8, is in good agreement with the generated one. For the left-handed case, in red in Figure 7.8, the distribution of $\cos\theta_t$ suffers from considerable migrations of events passing from the forward hemisphere to the backward one. The migration effect depends clearly on the electron beam polarisation, and can be explaine by kinematics:

- In case of a right-handed electron beam the sample is expected to be enriched with top quarks with right-handed helicity [53]. Due to the V-A structure of the Standard Model an energetic W boson is emitted into the flight direction of the top quark, and then decays into two energetic jets. The b quark from the decay of the top quark are comparatively soft, see Figure 7.9. Therefore, the direction of the top quark is essentially reconstructed from the direction of the energetic jets from the W boson decay. This scenario is thus insensitive towards a wrong association of the jet from the b quark decay to the jets from the W boson decay
- In case of a left-handed electron beam the sample is enriched with top quarks with left-handed helicity. In this case the W boson is emitted opposite to the flight-direction of the top quark and gains therefore only little kinetic energy. In fact for a centre-of-mass energy of 500 GeV the W boson is produced nearly at rest. On the other hand the b quarks are very energetic and will therefore dominate the reconstruction of the polar angle of the top quark, see Figure 7.9. In this case a wrong association of the jets from the W boson decay with that from the b quark can flip the reconstructed polar angle by π giving rise to migrations in the polar angle distribution of the top quark.

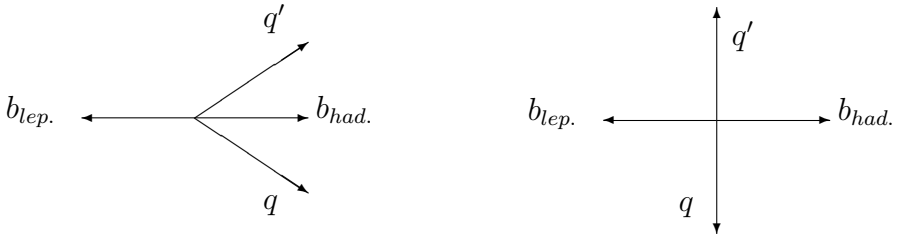

Figure 7.9: In case of a t_R decay,on the left, the jets from the W dominate the reconstruction of the polar angle of the top quark. In case of a t_L, on the right, the W is practically at rest and jets from the b quark dominate the reconstruction of the polar angle of the top quark.

So the measurement of $\cos\theta_t$ depends a lot, in the left-handed case, on the correct association of the b quark jet to the jets of the hadronic W boson decays.

This migration effect will deteriorate the precision on the measurement of the observable, mainly by introducing systematic effects. Like the effect comes from an uncertainty in the association of the b jet with the W boson, it can be solved by a better selection of the events or by knowing also the charge of the b jet.

7.5.1 The χ^2 Method

One solution to reduce the migration effect is to select only the best reconstructed events to have a clearer identification of which b jet goes with the W boson. The quality of the reconstructed events is estimated by the following quantity:

$$\chi^2 = \left(\frac{\gamma_t - 1.435}{\sigma_{\gamma_t}}\right)^2 + \left(\frac{p_b^* - 68}{\sigma_{p_b^*}}\right)^2 + \left(\frac{\cos\theta_{bW} - 0.23}{\sigma_{\cos\theta_{bW}}}\right)^2 \tag{7.7}$$

where p_b^* and $\cos\theta_{bW}$ have already been introduced in Equation 7.4. The defined χ^2 comprises in addition the Lorentz factor $\gamma_t = E_t/m_t$ of the final state top quark, which is shown in Figure 7.10. For each variable, the distribution in both cases of a good or a bad combination of the jets from b quarks to that from the W boson are checked with the Monte Carlo truth information, as illustrated in Figure 7.10 for the variable γ_t. For the events in which this association went wrong, labelled as bad combination in Figure 7.10, lead to a distorted distribution in these observables, and these events will be discarded by a cut on the maximum value allowed for the χ^2.

For $\chi^2 < 15$ the reconstructed spectrum agrees very well with the generated one, but the reconstruction efficiency falls down to 28.5 %. Figure 7.11 demonstrates the improved agreement between the reconstructed and generated distribution of the top quark polar angle in the case $\mathcal{P}, \mathcal{P}' = -1, +1$ for the beam polarisation. It shows also that the residual Standard Model background is very small, less than 2 % in the case $\mathcal{P}, \mathcal{P}' = -1, +1$, prone to be more affected by the background. The forward backward asymmetry A_{FB}^t can be derived from these angular distributions, see Chapter 8.

7.5.2 The B Charge Method

The golden way to clean up the combination ambiguity is to measure the charge of the b jets. Indeed with one know both, the lepton charge and the b jets charge, there is no more doubt on which b jets should be combined with the two jets from the W boson. The B charge measurement method is inspired by the fully hadronic analysis [78].

The b quark charge Q_b at the vertex is reconstructed, by LCFIPlus, as the sum of the charge of all the tracks with a $p_t > 100\,\text{MeV}$, related to this vertex. To

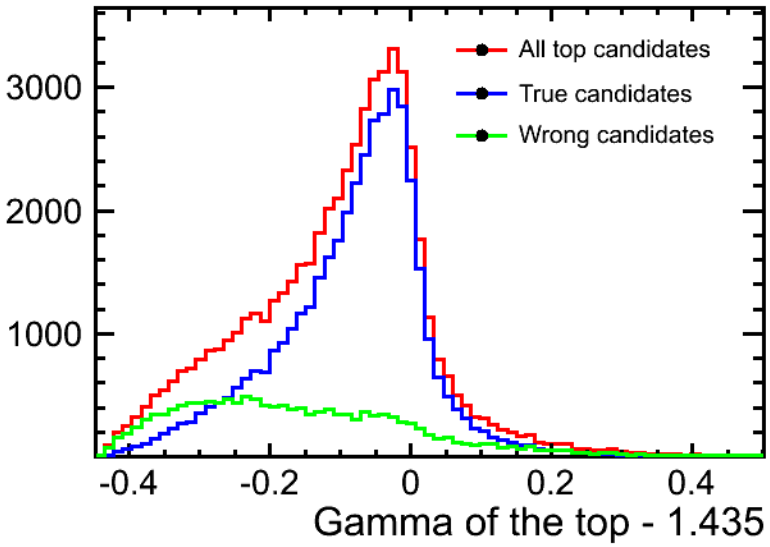

Figure 7.10: Lorentz factor of the top quark, γ_t, used in the χ^2 for the selection of well reconstructed events in case of $\mathcal{P}, \mathcal{P}' = -1, +1$ beam polarisation.

identify the b and the $\bar{b}$ quarks the event charge $C = Q_{b_0} - Q_{b_1}$ is defined, $Q_{b_{0,1}}$ is the charge of the $b_{0,1}$ jets. The Figure 7.12 shows the distribution of the event charge, and the subdistribution using the Monte Carlo truth information in the case of a t or $\bar{t}$ event. As expected, most of the events have a non-zero C value, which implies that we can distinguish between a top and an anti-top quark using the following reasoning:

- If $C = 0$, one can not concluded so the event is discarded.
- If $C < 0$, the jet b_0 is assumed to be produced in the decay of a top quark.
- If $C > 0$, the jet b_0 is assumed to be produced in the decay of an anti-top quark.

Once the charge of the b jets are identified, they are compared to the charge of the lepton to check if the combination choice was the good one. The first case, when $C = 0$, doesn't give any additional information and represents 25 % of the events. In the case where $C \neq 0$ the lepton charge is in agreement with the b jet charge in 52 % of the events and in disagreement in 23 % of the events. The solution to cure the migration effect with is to classified the events depending on the charge agreement and to select only the best ones. An additional cut on γ_t, as suggested by Figure 7.10, is also used to enrich the sample with good combination events. The final selection cut is:

- $(\gamma_t - 1.435) > -0.2$ for $t\bar{t}$ events with the good event charge - lepton charge agreement.

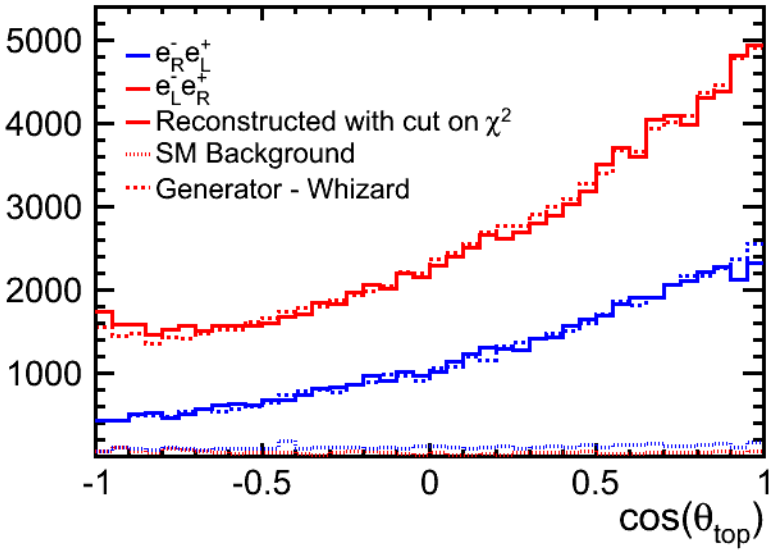

Figure 7.11: Reconstructed forward backward asymmetry together with residual Standard Model background compared with the prediction by the event generator WHIZARD after the application of a cut on $\chi^2 < 15$ for the beam polarisations $\mathcal{P}, \mathcal{P}' = -1, +1$ as explained in the text. Note that no correction is applied for the beam polarisations $\mathcal{P}, \mathcal{P}' = +1, -1$

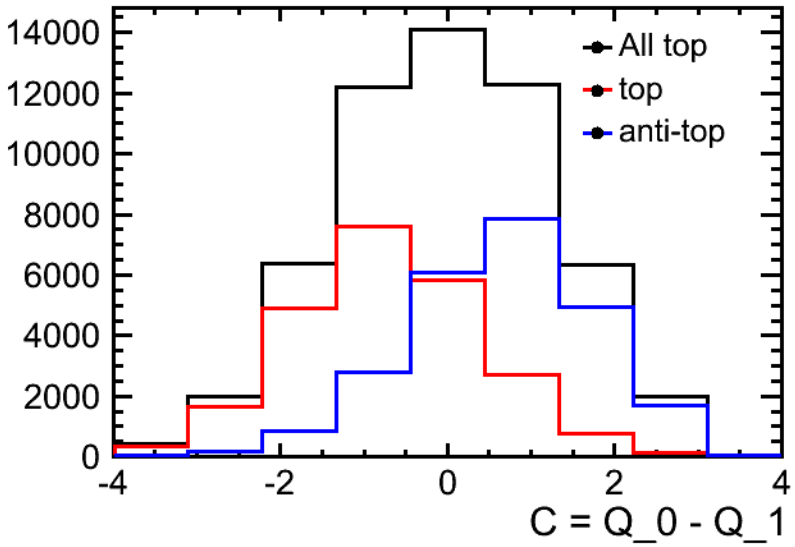

Figure 7.12: Distribution of the event charge $C = Q_{b_0} - Q_{b_1}$ variable. The two subdistribution used the Monte Carlo truth information to know if its a top or an anti-top event.

– $(\gamma_t - 1.435) > -0.1$ for $t\bar{t}$ events with a null event charge.

Figure 7.13 demonstrates the improved agreement between the reconstructed and generated distribution of the top quark polar angle in the case $\mathcal{P}, \mathcal{P}' = -1, +1$ for the beam polarisation. With this cut selection the efficiency falls down to 30.8 %.

One should note at this point that the LCFIPlus package is not yet optimised for the charge measurement, so further improvement can be expected in the future. During the vertex reconstruction low p_T tracks are dropped without keeping the information about their role in the total vertex charge. Access to the tertiary vertex will also help the vertex charge measurement. In case of a B^0 meson no charge can be measured at the secondary vertex, but like the B^0 mesons decay to D mesons, which in turn decay to leptons the charge measurement is possible at the tertiary vertex. This will help to improve the efficiency and the purity of the vertex charge measurement.

To improve the vertex charge measurement it is also possible to use the semileptonic decay of the B meson instead of the sum of the charge of the tracks at the vertex. In that case the charge of the vertex is simply the charge of the lepton coming from the decay of the B meson. This was the method used at LEP and SLC [79]. A first study of this method [80] shows a small improvement of the efficiency, around +2.5 %.

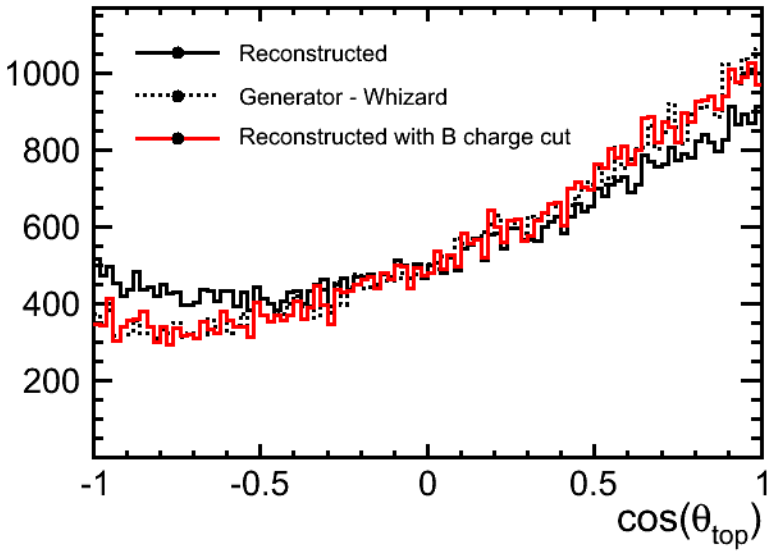

Figure 7.13: Reconstructed forward backward asymmetry compared with the prediction by the event generator WHIZARD before and after the application of a cut selection using the b jets charge information for the beam polarisations $\mathcal{P}, \mathcal{P}' = -1, +1$ as explained in the text.

7.6 The Helicity Angle Distribution

The helicity angle, $\theta_{\text{hel.}}$ is measured in the rest frame of the top quark with the z-axis defined by the direction of motion of the top quark in the laboratory. As discussed in [53] this definition of $\theta_{\text{hel.}}$ is not unique but some detailed investigations have shown that the choice of [59] seems optimal. The observable $\cos\theta_{\text{hel.}}$ has to be computed from the momentum of the top quark from which the W boson decayed leptonically into a lepton and a neutrino. Like the reconstruction of this top quark is not possible with enough precision, due to the presence of the neutrino, one can use the energy momentum conservation of the $t\bar{t}$ events. By neglecting the initial state radiation effects one can deduce the energy-momentum of the top quark from which the W boson decayed leptonically, from the energy-momentum of the top quark from which the W decayed hadronically, and which is reconstructed in the analysis. A Lorentz transformation boosts the lepton into the rest frame of the top quark, and gives access to a very precise knowledge of $\cos\theta_{\text{hel.}}$. To determine the helicity angle only the angle of the lepton needs to be known, and in the case of a τ lepton, which significantly contribute to this analysis (10- 15 %), the charged lepton and the τ lepton are approximately collinear and therefore the method remains valid.

Based on the cut selection against the background, the angular distribution of the decay lepton in the rest frame of the top quark, is shown in Figure 7.14 together with the residual Standard Model background for fully polarised beams. The background is small relative to the signal and to a good approximation flat, and has therefore only a minor influence on the slope of the signal distribution and will be neglected in the following.

The distribution exhibits a drop in reconstructed events towards $\cos\theta_{\text{hel.}} = -1$. This drop can be explained by the event selection which suppresses leptons with small energies, as illustrated in Figure 7.15. The plot shows that the leptons with $\cos\theta_{\text{hel.}} < -0.6$ have a lower energy and are therefore not well isolated in the jet. These leptons are so more difficults to identified and doesn't always pass the isolation cuts, leading to the hole in the distribution. Outside this region and in contrast to the forward backward asymmetry the reconstructed angular distribution agrees very well with the generated one. This means that this observable suffers much less from the migration effect and it is therefore not necessary to tighten the selection in the same way as for A_{FB}^{t}. The reason for the bigger robustness of the angular distribution can be explained by kinematics.

The parameter λ_t can then be derived from the slope of the helicity angle distribution that is obtained by a fit to the linear part of the angular distribution.

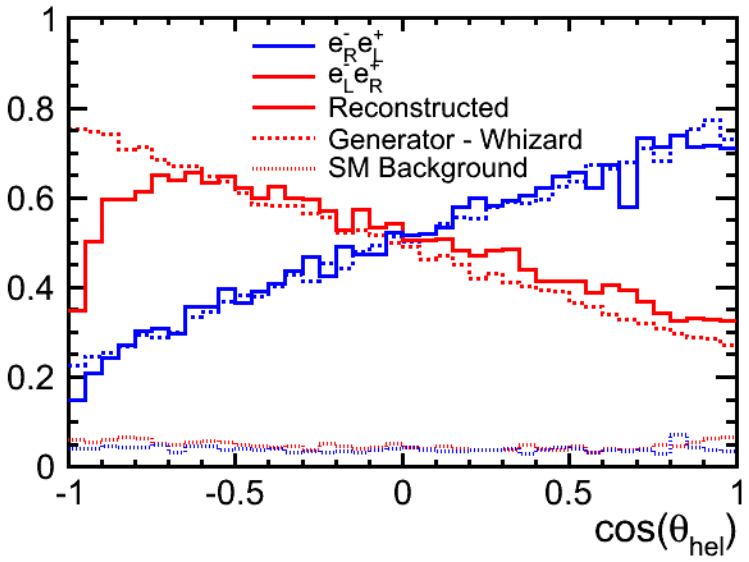

Figure 7.14: Helicity distribution: polar angle of the decay lepton in the rest frame of the top quark.

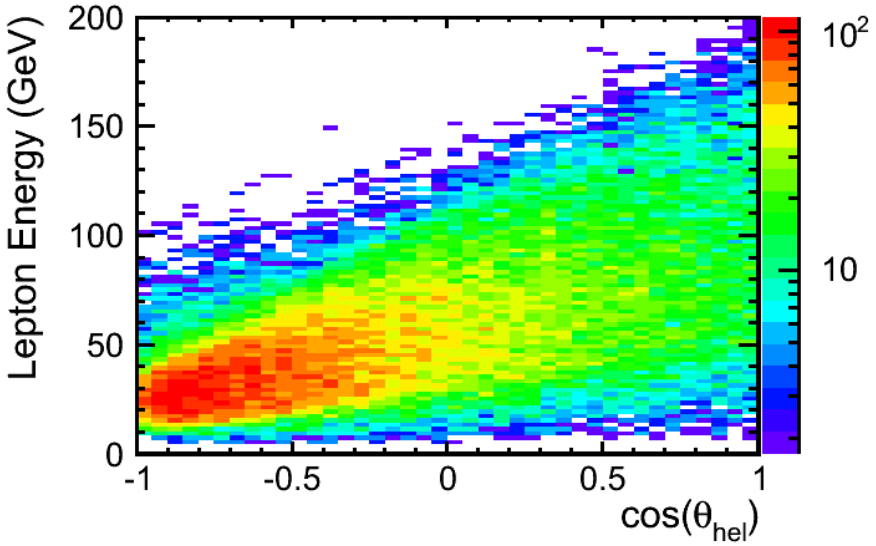

Figure 7.15: Energy distribution of the lepton with respect to its polar angle in the rest frame of the top quark.

Chapter 8

Reachable Accuracies on the Top Quark Electroweak Couplings

Once the analysis is done, the statistical errors are calculated for the different observables, based on the signal selection efficiency and on the polar angle distribution. These errors, together with the systematic and theoretical errors, give the accuracies on the top quark couplings that can be reached at the ILC with the full simulation of the ILD detector.

8.1 The Statistical Errors

8.1.1 The Cross Section

To measure the cross section, one has to count the final number of $t\bar{t}$ events selected in the analysis, and to know the luminosity $\mathcal{L}$ and efficiency ϵ to select the signal. The cross section σ is given by the following formula:

$$\sigma = \frac{N}{\epsilon \mathcal{L}} \tag{8.1}$$

with N being the final number of $t\bar{t}$ events selected after the cuts against background presented in Table 7.1. The cross section is measured in both beam polarization configuration, $\mathcal{P}, \mathcal{P}' = \pm 0.8, \mp 0.3$. The corresponding errors on the cross section is given by:

$$\left(\frac{\Delta\sigma}{\sigma}\right)^2 = \left(\frac{\Delta N}{N}\right)^2 + \left(\frac{\Delta\mathcal{L}}{\mathcal{L}}\right)^2 \tag{8.2}$$

with $\Delta N/N = 1/\sqrt{N}$. The expected precision on the luminosity at the ILC, given in [81] is $\Delta\mathcal{L}/\mathcal{L} = 0.1\,\%$.

The statistical uncertainty is then estimated taking into account the efficiencies determined in Chapter 8 and using the born level cross given in Table 6.1 of the Chapter 6, scaled to the realistic polarisation with Equation 6.3. The result gives a statistical uncertainty of 0.47 % in the case of a left-handed initial electron beam and 0.63 % in the case of a right-handed electron beam. In reality these numbers may be somewhat worse given the fact that in particular for e_L the generated sample is contaminated by single top events.

8.1.2 The Forward Backward Asymmetry

In the case of A^t_{FB}, the statistical uncertainty on such an asymmetry is given by:

$$\delta_{A^t_{FB}} = \sqrt{\frac{1-(A^t_{FB})^2}{N}} \tag{8.3}$$

where N is the number of reconstructed $t\bar{t}$ events.

The numerical results are given in Table8.1 and compared with the generated value. The statistical error is corrected for the realistic beam polarizations $\mathcal{P}, \mathcal{P}' = \pm 0.8, \mp 0.3$. It shows that for the standard luminosity statistical precisions of better than 2 % can be expected. The cut selection against the migration effect is applied only for the left-handed electron beam. With the χ^2 methods the reconstructed $A^t_{FB} = 0.326$ with an efficiency of 28.5 %, while with B charge methods the reconstructed $A^t_{FB} = 0.316$ with an efficiency of 30.8 %. Both methods leads to the same $\delta_{A^t_{FB}}/A^t_{FB}$. If one takes, by convention, the systematic error due to the ambiguities as half the difference between the reconstructed A^t_{FB}, it is expected to be smaller than the statistical error, around 0.5 %.

$\mathcal{P}, \mathcal{P}'$	$(A^t_{FB})_{\text{gen.}}$	A^t_{FB}	$(\delta_{A^t_{FB}}/A^t_{FB})_{\text{stat.}}$ %
-1,+1	0.339	0.326	1.8 (for $\mathcal{P}, \mathcal{P}' = -0.8, +0.3$)
+1,-1	0.432	0.420	1.3 (for $\mathcal{P}, \mathcal{P}' = +0.8, -0.3$)

Table 8.1: Statistical precisions expected for A^t_{FB} for the two different beam polarizations. The χ^2 method is used here for the left-handed electron beam case.

8.1.3 The Helicity Angle Distribution

The parameter λ_t corresponds to the slope of the helicity angle distribution, see Equation 6.8. The slope of the distribution is obtained by a fit to the linear part

in the range $\cos\theta_{\text{hel.}} = [-0.6, 0.9]$ for $\mathcal{P}, \mathcal{P}' = -1, +1$ and $\cos\theta_{\text{hel.}} = [-0.9, 0.9]$ for $\mathcal{P}, \mathcal{P}' = +1, -1$.

The numerical results are given in Table 8.2 for the two initial beam polarisations, $\mathcal{P}, \mathcal{P}' = \pm 1, \mp 1$, but with the statistical errors corrected for the realistic beam polarizations $\mathcal{P}, \mathcal{P}' = \pm 0.8, \mp 0.3$. The results are compared with the values of λ_t as obtained for the generated sample. For the systematic studies the fit was repeated for different fitting ranges and the result changes by about 1 % when changing the fit range to $\cos\theta_{\text{hel.}} = [(-0.4, 0.5), 0.9]$ for $\mathcal{P}, \mathcal{P}' = -1, +1$. A quarter of the shift between the generated and the reconstructed value is also taken into account. For the systematic error of the measurement, the errors on the slope from the variation of the fit range and that from the difference between generated and reconstructed slope are added in quadrature.

$\mathcal{P}, \mathcal{P}'$	$(\lambda_t)_{\text{gen.}}$	λ_t	$(\delta\lambda_t)_{\text{stat.}}$	$(\delta\lambda_t)_{\text{syst.}}$
-1,+1	-0.484	-0.437	0.011 (for $\mathcal{P}, \mathcal{P}' = -0.8, +0.3$)	0.013
+1,-1	0.547	0.534	0.013 (for $\mathcal{P}, \mathcal{P}' = +0.8, -0.3$)	0.006

Table 8.2: Results on λ_t derived from the slope of the helicity angle distribution for the two different beam polarizations.

8.2 The Systematic and Theory Errors

With the level of statistical errors reached, of the order of the percent, the systematic and theory uncertainties should be carefully studied, and they should be at least at the same level of precision. A first attempt to identify and quantify systematic uncertainties, which may influence the precision measurements, was realized and resumed here:

- As shown in Section 8.1.1 the luminosity is a critical parameter for cross section measurements and can be controlled to 0.1 % according to the study [81].
- The polarisation is a critical parameter for all analyses, it enters directly in the cross section measurements. The studies done for the DBD using W pair production [82] lead to an uncertainty of 0.1 % for the polarisation of the electron beam and to an uncertainty of 0.35 % for the polarisation of the positron beam. This translates into an uncertainty of 0.25 % on the cross section for $\mathcal{P}, \mathcal{P}' = -0.8, +0.3$ and 0.18 % on the cross section for $\mathcal{P}, \mathcal{P}' = +0.8, -0.3$. The uncertainty on the polarisation can be neglected with respect to the statistical uncertainty for A_{FB}^t and λ_t.
- The mutual influence of the electromagnetic fields of the colliding bunches provokes radiation of photons known as Beamstrahlung. This Beamstrahlung

modulates the luminosity spectrum by moving particles from the nominal energy to smaller energies. At the ILC, for the center of mass energy of 500 GeV, about 60 % of the particles are expected to have 99 % or more of the nominal energy [28]. The beam energy spread, the RMS of this main luminosity peak, is 124 MeV for the electron beam and 70 MeV for the positron beam [28]. Both effects play a role at the $t\bar{t}$ threshold [83] but can be neglected at energies well above this threshold.

- The migrations, presented in Section 7.5, have to be taken into account for the measurement of A_{FB}^t, in the $\mathcal{P}, \mathcal{P}' = -0.8, +0.3$ beam polarisation configuration. These migrations are reduced either by stringent requirements on the event selection using a χ^2 analysis, or by the measurement of the b jets charges. This in turn leads to a penalty in the efficiency, and to additional experimental uncertainties in the top quark reconstruction. The fact to have two different methods to deal with the migration problems will help to control the systematics.
- There is a number of other experimental effects such as acceptance, uncertainties of the b tagging or the influence of passive detector material. The LEP experiments quote a systematic uncertainty on R_b of 0.2 % a value which may serve as a guideline for values to be expected at the ILC, which on the other hand will benefit from far superior detector resolution and b tagging capabilities. In general the experimental effects can be estimated from the experience gains with the LEP experiments.

8.2.1 The Theory Aspects

On the theory aspects, the state-of-the-art calculations are not at the same level for the QCD and the electroweak corrections. For the QCD part, the corrections to the $t\bar{t}$ production are known up to N^3LO [84], and the ones to A_{FB}^t up to N^2LO [85]. These lead to an uncertainty of the per mil level for the cross section, and smaller than 1 % for A_{FB}^t, which are of the same order than the experimental ones. For the electroweak corrections on the other side, the corrections are calculated only at the one-loop level. This leads to a correction to the total cross section of approximately 5 %, and to A_{FB}^t of approximately 10 % [86][87]. These corrections are large with respect to the expected experimental errors of the ILC, and we don't know so far the errors on these corrections. So further work is needed to estimate the size of the two-loop correction. Discussions of theory groups are ongoing to address these aspects.

Some others theory aspects are:

- Single top production at the ILC in association with a W boson and bottom quark (through WW^* production) leads to the same final state as top quark pair production. It forms a sizable contribution to the six fermion final state

and must be taken into account in the results. This is left for a future study.
– Possible beyond Standard Model effects may affect the signal as well as the various components of the background, in particular the $t\bar{t}$ induced background. This will therefore require a careful tuning of our generators, but seems feasible without a significant loss of accuracy.

As a summary it can be concluded that the total systematic uncertainties should not exceed the statistical uncertainties, if the electroweak corrections are addressed. The systematic uncertainties, however, requires an excellent control of a number of experimental quantities on which the results depend.

8.3 Precision of Form Factors

The results on the reconstruction efficiency, A_{FB}^t and λ_t presented in Section 8.1 are transformed into precisions on the form factors $\tilde{F}_i$, using only the statistical errors. The form factors $\tilde{F}_i$ are used instead of the from factors F_i for historical reasons, to be able to compare with LHC results of Snowmass 2005. The results are summarised in Table 8.3 and Figure 8.1 and are compared with results of earlier studies for a linear e^+e^- collider as published in the TESLA TDR [33] as well as with precisions obtained in a simulation study for the LHC. In the LHC and TESLA studies only one form factor was varied at a time while in the present study the two $\tilde{F}_2$ or the four $\tilde{F}_1$ form factors are varied simultaneously. Indeed, at a center of mass of 500 GeV, there is a bad separation between F_{1V} and F_{2V}. So to get a good precision on F_{2V} we choose to calculate them apart from the four F_1 form factors. The disentangling of vectorial and tensorial couplings is only possible at large center of mass energies.

The comparison of the numbers shows the capability of precision of an electron positron collider, which lead to a spectacular improvement of more than an order of magnitude. The precisions which can be obtained at the LHC used here are based on simulations and have to be revisited with the real LHC data. A first result on associated production of vector boson and $t\bar{t}$ pairs is published in [88][72]. The results for the $t\bar{t}Z$ cross section on the basis of 5 fb^{-1} is $\sigma_{t\bar{t}Z} = 0.28^{+0.14}_{-0.11}(\text{stat.})^{+0.06}_{-0.03}(\text{syst.})$ pb while the NLO prediction gives $\sigma_{t\bar{t}Z} = 0.137^{+0.012}_{-0.016}$ pb. So far the statistical errors are of course very high, but it gives the first indication of the LHC capability, and one can reasonably expect an error of 13 % on this quantity [71][72].

The expected high precision at a linear e^+e^- collider allow for a test of the Standard Model and to detect effects of new physics. The findings can be confronted with predictions in the framework of Randall-Sundrum models and/or compositeness models such as the ones presented in Section 6.5 or Little Higgs models as [89]. All these models entail deviations from the Standard Model values of the top quark couplings to the Z^0 boson that will be measurable at the ILC.

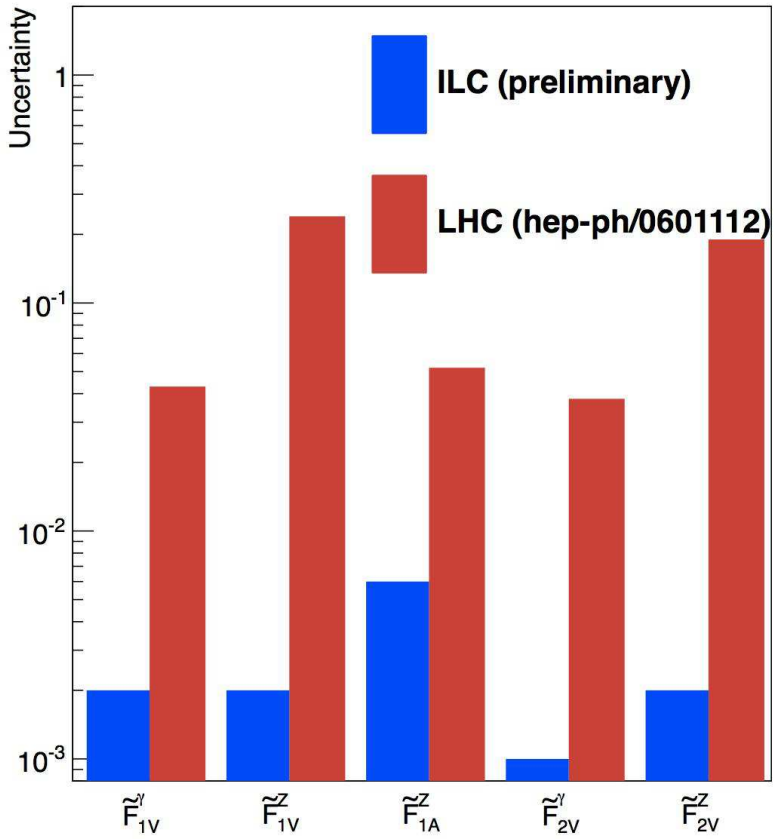

Figure 8.1: Comparison of statistical precisions on CP conserving form factors expected at the LHC [90] and at the ILC. The LHC results assume an integrated luminosity of $\mathcal{L} = 300\, fb^{-1}$. The results of the ILC assume an integrated luminosity of $\mathcal{L} = 500\, fb^{-1}$ at $\sqrt{s} = 500\,\text{GeV}$ and a beam polarization $\mathcal{P}, \mathcal{P}' = \pm 0.8, \mp 0.3$.

Coupling	Standard Model value	LHC [90] $\mathcal{L} = 300\, fb^{-1}$	e^+e^- [33] $\mathcal{L} = 300\, fb^{-1}$ $\mathcal{P}, \mathcal{P}' = -0.8, 0$	e^+e^- ILC DBD $\mathcal{L} = 500\, fb^{-1}$ $\mathcal{P}, \mathcal{P}' = \pm 0.8, \mp 0.3$
$\Delta\tilde{F}^{\gamma}_{1V}$	0.66	$+0.043$	$-$	$+0.002$
		-0.041	$-$	-0.002
$\Delta\tilde{F}^{Z}_{1V}$	0.23	$+0.240$	$+0.004$	$+0.002$
		-0.620	-0.004	-0.002
$\Delta\tilde{F}^{Z}_{1A}$	-0.59	$+0.052$	$+0.009$	$+0.006$
		-0.060	-0.013	-0.006
$\Delta\tilde{F}^{\gamma}_{2V}$	0.015	$+0.038$	$+0.004$	$+0.001$
		-0.035	-0.004	-0.001
$\Delta\tilde{F}^{Z}_{2V}$	0.018	$+0.270$	$+0.004$	$+0.002$
		-0.190	-0.004	-0.002

Table 8.3: Sensitivities achievable at 68.3 % CL for CP conserving form factors $\tilde{F}^{X}_{1V,A}$ and $\tilde{F}^{X}_{2V}$ at the LHC and at linear e^+e^- colliders. In the LHC studies and in earlier studies for a linear e^+e^- collider as published in the TESLA TDR study, only one coupling at a time is allowed to deviate from its Standard Model value. In the present study, denoted as ILC DBD, either the four form factors $\tilde{F}_1$ or the two form factors $\tilde{F}_2$ are allowed to vary independently. The sensitivities are based on statistical errors only.

Conclusion

This thesis presents the analysis of the $t\bar{t}$ production in the semi-leptonic decay channel at the ILC. Results are given for an integrated luminosity of $\mathcal{L} = 500\, fb^{-1}$ and a centre-of-mass energy of $\sqrt{s} = 500\,\text{GeV}$. Using the electrons and positrons beam polarization capability of the ILC, the analysis is done with two beam polarizations configurations, $\mathcal{P}, \mathcal{P}' = \pm 0.8, \mp 0.3$. The goal of the analysis was to estimate the precision on the top quark couplings to the photon and the Z^0 boson. For that, the statistical errors were measured on three different observables, $\sigma_{t\bar{t}}, A^t_{FB}$ and λ_t, using generated events passing through the full simulation of the ILD detector.

Semi-leptonic events, including those with the W boson decaying in τ leptons, can be selected with an efficiency of about 55 %. The cross section of the semi-leptonic channel of $t\bar{t}$ production can therefore be measured to a statistical precision of about 0.5 %. For the forward backward asymmetry A^t_{FB}, it was pointed out that for the left-handed polarization of the initial electron beam the V-A structure of the electroweak theory leads to migrations, which distort the angular distribution of the $t\bar{t}$ events. These migrations can be remedied by two different methods, either tightening the selection criteria of the events via a χ^2 cut, or measure the charge of the b jet. Taking into account this correction, A^t_{FB} can be determined to a precision of better than 2 % for both beam polarisations. Finally, with the slope of the helicity angle distribution we measured the fraction of top quarks of a given helicity in the event sample. This variable is very robust against the migration effects and can be measured to a precision of about 4 %. These results have been published in an arXiv note [91] and a journal publication is ongoing. They have also played a central role in the top quark section of the DBD [28] and of the Snowmass proccess [92].

The observables together allow for a largely unbiased disentangling of the individual couplings of the top quark to the Z^0 boson and the photon. These couplings can be measured with high precision at the ILC, more than one order of magnitude better than it will be possible at the LHC, and would allow for the verification of a great number of models for physics beyond the Standard Model.

But, such a level of precision requires excellent detector. The ILD detector is one of the two detector concepts for the ILC, based on the Particle Flow Algorithm. The Particle Flow Algorithm builds upon highly granular calorimeters for detectors to be operated at a future linear electron positron collider. Therefore the $R\&D$ for a highly granular SiW-ECAL is on-going. After the proof of principle with the physics prototype, a technological prototype is constructed and tested,especially to study the engineering aspects of the project. Some first test beam with idealized setup have been done at DESY in 2012 and 2013 and gives encouraging results with a signal over noise ratio better than for the physics prototype. The power pulsing

mode of the prototype had also been tested with encouraging results. These results have been presented in the peer-reviewed proceedings of the Vienna Conference on Instrumentation [47] and a journal publication is ongoing. Further $R\&D$ is now needed to continue to test the power pulsing of the electronics, and the other real scale detector challenges.

Appendix A

Calibration of the SiW-ECAL Physics Prototype

Calibration of the ECAL

The calibration of the SiW ECAL establishes a relationship between the electronic signal(in ADC units) and another unit, more physical, here in MIP units. The final goal of the calibration is to have a relationship between ADC unit and the energy unit. The calibration process of the SiW-ECAL physics prototype presented in Chapter 4 will be done in this appendix.

The calibration process goals is to equalize the response of all the cells, because each cell should gives the same signal for the same energy deposited by the particle, and to find the relationship between the measuring units and the physical units. In our case we want to find the relationship between the electronic signal as delivered by the CALICE DAQ (in ADC units) and the energy units. The calibration procedure of the SiW ECAL prototype consists of two steps:

- In the first step we done what is called a MIP calibration. The energy unit used here is a MIP. When a muon with momentum from a few hundreds MeV to a few tens GeV passes through the detector it loses its energy only through ionization, and has its energy loss rates close to the minimum. These muons are said to be minimum ionizing particles (MIP). The mean energy loss of the muons in the active medium of a pad is defined as a MIP energy unit.
- In a second step an absolute calibration will be made by converting the unit of MIP in GeV, using electrons that deposit their energies completely into the prototype and where the energies of the electron beams are known.

This appendix will only describe the MIP calibration.

The pedestal is the mean value of the readout signal without beam, this signal comes from electronics noise. Subtraction of the pedestal from the readout signal

gives the actual signal value. After this subtraction the resulting residual pedestal is checked for each channel. The noise peak is fitted with a Gaussian function and the mean of the Gaussian is taken as the residual pedestal and the width as the noise. We after have to check if the residual pedestal and pedestal noise are stable with respect to all the pad.

The result from Hengne LI's Thesis for the previous beam test period at FNAL in 2008 gives an average residual pedestal over all channels of -0.058 ± 0.003 ADC counts, with a RMS of 0.281 ± 0.002 ADC counts and an average pedestal noise of 5.930 ± 0.003 ADC counts, with a RMS of 0.330 ± 0.002 ADC counts.

As we have said the MIP calibration uses muons. So we should select events with muon. The MIP muons passes through the ECAL as a straight line. This event is selected by requiring:

- The hits should be fit as a straight line.
- The number of hits in the straight line must be greater than 10.
- The distance between two hits in consecutive layers must be less than 2 cm.
- Then we have to optimise these selection criteria depending on the results.

To have enough statistic we need ≈ 1000 muons/cell.

For each pad, the calibration constant is determined by fitting the hit energy distribution by a convolution of a Landau distribution with a Gaussian (see Figure A.1). The Landau distribution describes the energy loss by the MIP muon while it is passing through the ECAL. The most probable value of the Landau defines the calibration constant. The Gaussian distribution describes the uncertainty of the detector response due to the noise. The sigma of the Gaussian defines the signal noise.

After some corrections, on dead pads for example, explained in [37] we can find the value of the calibration constant. This calibration constant gives the number of ADC counts for one MIP.

The result from Hengne LI's Thesis for the previous beam test period at FNAL in 2008 gives an average of the calibration constants over all pads of 47.61 ADC counts, with a RMS of 2.06 ADC counts and an average of the signal noise of 7.22 ADC counts, with a RMS of 1.00 ADC counts. These values give a ratio signal over noise of 6.6 to compare with 10 as alternative goal.

Figure A.2 shows the distribution of the χ^2/Ndf for all the pads. The mean value of 1 shows that the fit works fine.

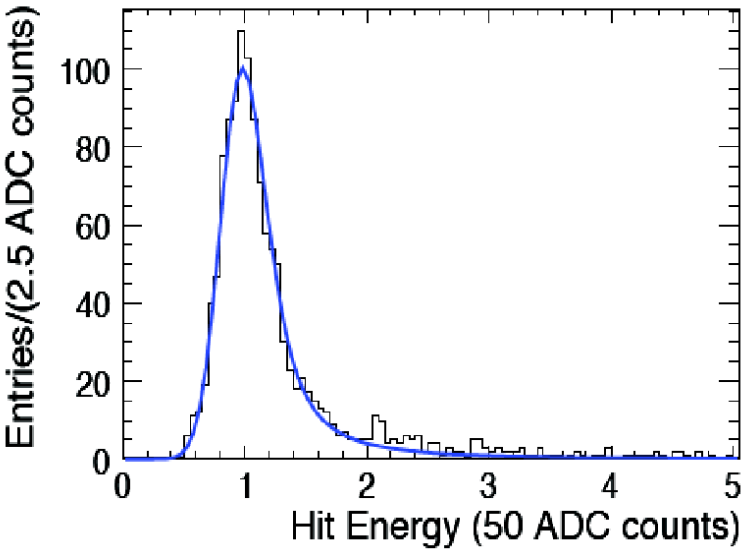

Figure A.1: A typical fitting of the hit energy distribution of a pad to extract the calibration constant.

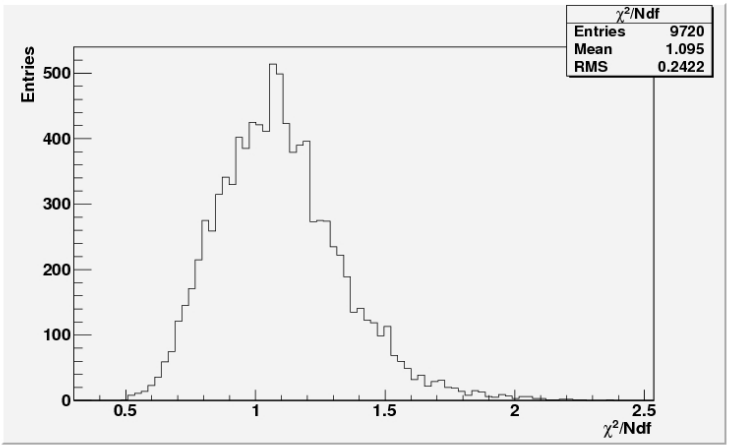

Figure A.2: Distribution of the χ^2/Ndf for all the pads.

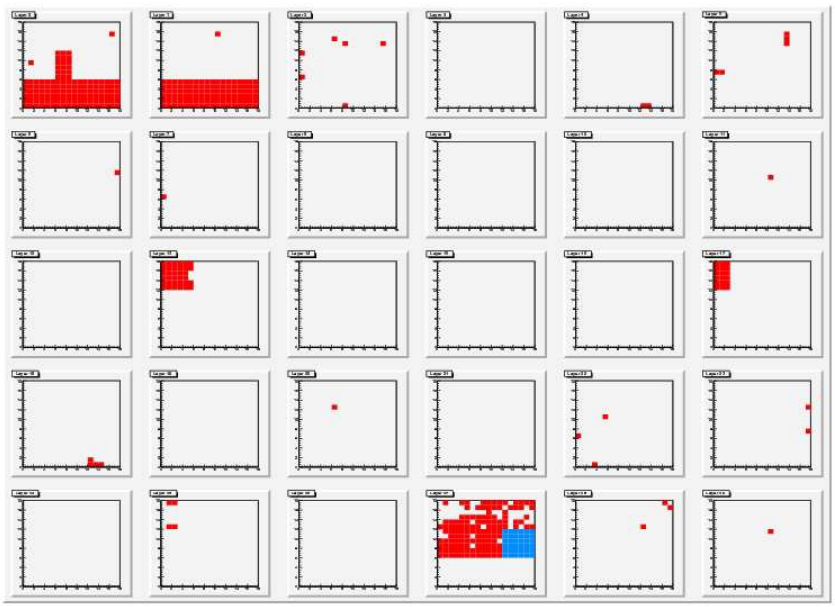

Figure A.3: Map of the dead pads for each of the 30 layers.

Results

Dead Pads Study

For the calibration study I have used the 9 runs from Run630020 to Run630028. This represents ≈ 1225000 events. The first study I have done is to see if there are dead pads with respect to the fit results. After being fit a pad is said to be dead if it doesn't respect one of the following criteria:

- The MPV value is between 27.5 and 53.5 ADC counts.
- The error on the MPV is less than 3 ADC counts.
- The noise value is between 2 and 14 ADC counts.
- The χ^2/Ndf is between 0.5 and 3.

In Figure A.3 there is a map of the dead pads (in red) for each of the 30 layers. In layer 28 there is one wafer in blue which will be discussed in detail later. In total there are 486 dead pads (≈ 5% of the pad) mainly because they don't respect the fitting criteria. For example the first two bottom slabs give some results but with a MPV value too high, around 70 ADC counts, which doesn't respect the fitting criteria.

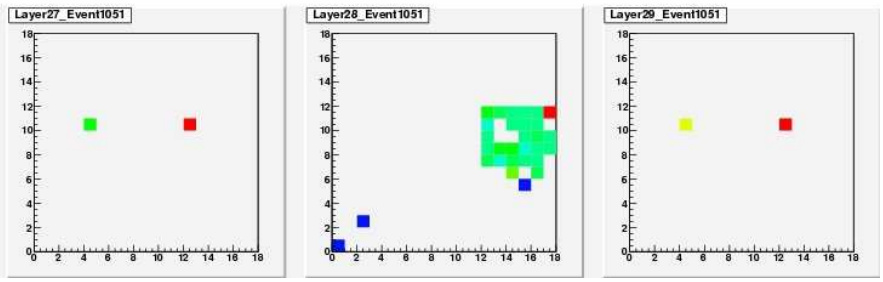

Figure A.4: Example of event with hits in the layer 27 28 and 29. In this example the bad wafer of layer 28 have almost all its pads on.

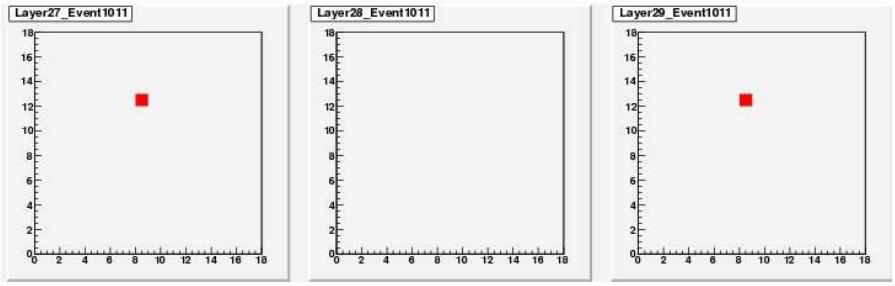

Figure A.5: Example of event with hits in the layer 27 and 29 and not in the layer 28.

The layer 28 is a particular layer with many dead pads. I study it in detail to see if we can try to find some reasonable calibration constant to be able to work with it. First by looking to the number of hits in each layer it appears that this layer gives an unusual high number of hits. This is because on of the wafer (the blue one in Figure A.3) has event with almost all its pads on (see Figure A.4).

There is another feature for this layer 28, sometimes we can found hits in the previous and the next layer but not in the layer 28 (see Figure A.5). In this case there is still a normal level of noise in the layer 28 but no pad with enough energy to be considered to have a hit. This appends in almost 13% of the events, but this number goes up to 25% if we remove the bad wafer of the layer 28. So this effect reduces the MIP statistics for the layer 28.

Taking into account all these effects we tried to find cuts in order to be able to find a value for the calibration constants of the layer 28.

The cuts that are applied are:

– remove the bad wafer in the MIP finder algorithm.
– The energy in the layer should be less than 400 ADC counts.

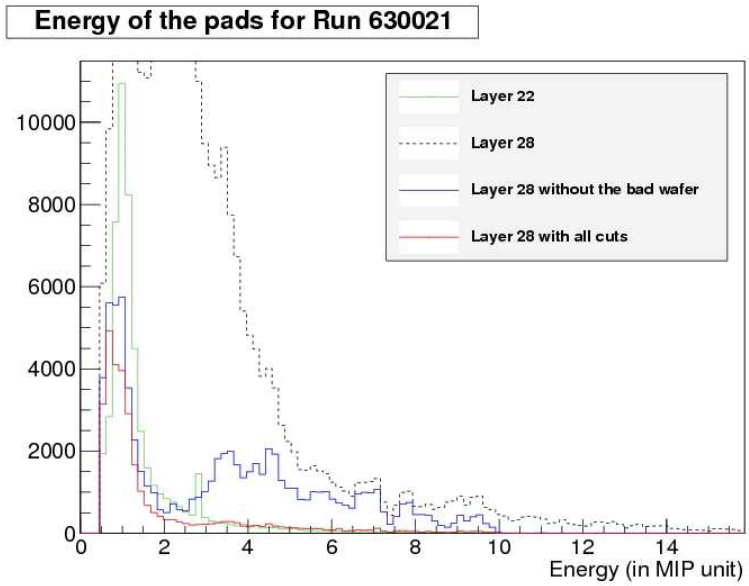

Figure A.6: Distribution of the energy of the pads in the layer 28. Different levels of cuts are shown.

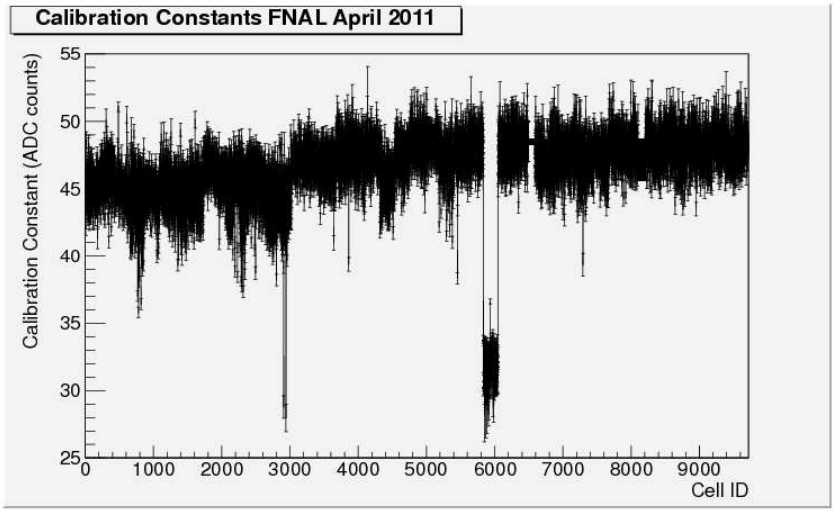

Figure A.7: Results of the calibration constants for all the pads.

– The event should not have hits only in the layer 28.

Figure A.6 shows that removing the bad wafer reduce a lot the number of hits in the layer 28. After this first cuts (blue curve) we still had some events with a too high energy compared to what we had in a normal layer (green curve). So we made the two other cuts to reduce this number. Finally we have a good energy distribution for the layer 28, but with a shift to the lower energy compared to the other layer.

The Calibration Results

The Figures A.7 and A.8 show respectively the calibration constant and the noise for each pad of the detector depending on its pad ID. We see here that the energy in the layer 28 is lower resulting in calibration constants around 30 ADC counts for the pads of this layer. The result for this beam test period at FNAL in April 2011 gives an average of the calibration constants over all pads of 46.48 ADC counts, with a RMS of 2.97 ADC counts and an average of the signal noise of 7.03 ADC counts, with a RMS of 0.95 ADC counts. These values give a ratio signal over noise of 6.6. These values are very similar to the one obtained by Hengne LI for the previous beam test period at FNAL in 2008.

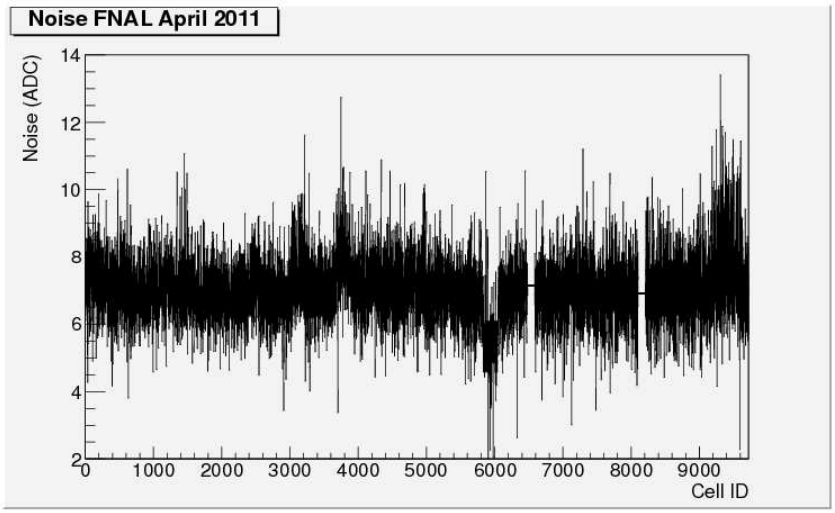

Figure A.8: Results of the noise for all the pads.

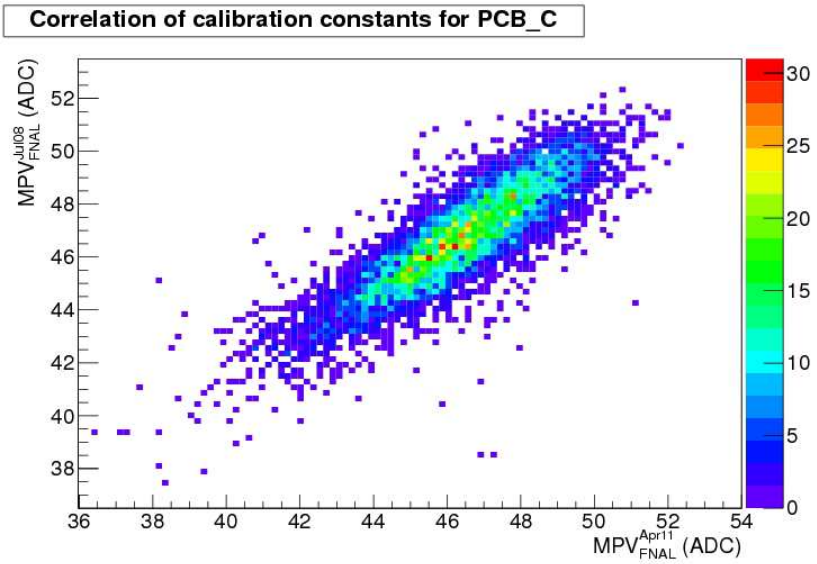

Figure A.9: Correlation of the calibration constants for the central PCBs of the two test beam periods.

The comparison between the two test beam periods is shown in Figure A.9. The plot shows the correlation for the calibration constants of the central PCBs. The correlation factor is 86% which is very good, and very important for operating a detector which at the end will have 10^8 cells.

Conclusion

A prototype of SiW ECAL for the ILC detector was tested. Data have been taken at FNAL in April 2011 and the Mip calibration of this data have been done and compare to previous test beam period. With this we show that the prototype Mip calibration is stable with respect to the pad and the time. The result for this beam test period at FNAL in April 2011 gives an average of the calibration constants over all pads of 46.48 ADC counts, with a RMS of 2.97 ADC counts and an average of the signal noise of 7.03 ADC counts, with a RMS of 0.95 ADC counts, giving a signal over noise ratio of 6.6.

Appendix B

CP Violating Couplings

Basics

The current at the $t\bar{t}X$ vertex, defined in Section 1.4, can be written [22]:

$$\Gamma_{\mu}^{t\bar{t}X}(k^2, q, \bar{q}) = ie\left\{\gamma_{\mu}\left(F_{1V}^{X}(k^2) + \gamma_5 F_{1A}^{X}(k^2)\right) + \frac{\sigma_{\mu\nu}}{2m_t}(q-\bar{q})^{\mu}\left(iF_{2V}^{X}(k^2) + \gamma_5 F_{2A}^{X}(k^2)\right)\right\} \tag{B.1}$$

with k^2 the four momentum of the exchanged boson, q and $\bar{q}$ the four vectors of the t and $\bar{t}$. The form factors F_{1V}, F_{1A} and F_{2V} are Charge and Parity symmetry, CP, conserving form factors and have been studied in detailed in Part III of the thesis. The form factor F_{2A} violates CP and will be described here. The CP violation is made possible by the introduction of a complex phase in the CKM matrix, which is posible thanks to the third quarks generation, or via higher order loops in the Feynman diagrams. The from factors $F_{2A}^{\gamma,Z}$ are related to the electric and weak dipole form factors $d_{\gamma}(s)$ and $d_Z(s)$ which may be represented by the effective interaction from [93]:

$$\mathcal{L} = -\frac{i}{2}d_{\gamma}\bar{t}\sigma_{\mu\nu}\gamma_5 t F^{\mu\nu} - \frac{i}{2}d_Z\bar{t}\sigma_{\mu\nu}\gamma_5 t Z^{\mu\nu} \tag{B.2}$$

This form factors $d_{\gamma,Z}(s)$ can have imaginary parts. The real part $Re(d_{\gamma,Z}(s))$ induces a difference into the top and anti-top polarizations orthogonal to the scattering plane of reaction. Non-zero absorptive parts $Im(d_{\gamma,Z}(s))$ lead to a difference in the top and anti-top polarizations along the top direction of flight. Since these form factors may develop an imaginary part, there are in reality 4 form factors to extract. The way to extract these form factors is to construct asymmetries that are CP violating in the case of the semi-leptonic top decay.

A well known example is the asymmetry of the lepton with respect to the production plane [94]:

$$O_+^{Re} = (\hat{q}_+^* \times \hat{q}_{\bar{X}}) \cdot \hat{e}_+ \qquad O_-^{Re} = (\hat{q}_-^* \times \hat{q}_X) \cdot \hat{e}_+ \tag{B.3}$$

where $\hat{q}_\pm^*$ are the unit momenta of the lepton in the corresponding top rest frame, $\hat{q}_{\bar{X},X}$ the unit momenta of the hadronic system from top decay, and $\hat{e}_+$ the direction of the positron beam. So one can demonstrate that $\mathcal{A} = O_+ - O_-$ is proportional to F_{2A}(see Equation B.5). The O^{Re} observables are the projection of the vector normal to the decay plane of the top quarks on the direction of the positron beam. A difference in these two projection is a sign of CP violation.

For the imaginary part of the form factor, one has to build observables of the type:

$$O_+^{Im} = -\left[1 + \left(\frac{\sqrt{s}}{2m_t} - 1\right)(\hat{q}_{\bar{X}} \cdot \hat{e}_+)^2\right] \hat{q}_+^* \cdot \hat{q}_{\bar{X}} + \frac{\sqrt{s}}{2m_t} \hat{q}_{\bar{X}} \cdot \hat{e}_+ \hat{q}_+^* \cdot \hat{e}_+ \tag{B.4}$$

The observable O_-^{Im} is defined to be the CP image of O_+^{Im}. It is obtained from O_+^{Im} by the substitutions $\hat{q}_{\bar{X}} \to -\hat{q}_X, \hat{q}_+^* \to -\hat{q}_-^*$.

In [94] is shown that one can design fully optimized observables O of this type which would allow to extract $Re[F_{2A}^{\gamma,Z}]$ and $Im[F_{2A}^{\gamma,Z}]$ with the best possible analyzing accuracy. What is also needed is full disentanglement. This seems possible since there are two asymmetries available for each polarization.

A reasonable approximation to write these CP violation asymmetries is [95]:

$$\begin{aligned} A_{\gamma,Z}^{Re} &= \langle O_+^{Re} \rangle - \langle O_-^{Re} \rangle = c_\gamma \left[PRe(F_{2A}^\gamma) + KZRe(F_{2A}^Z) \right] \\ A_{\gamma,Z}^{Im} &= \langle O_+^{Im} \rangle - \langle O_-^{Im} \rangle = d_\gamma \left[Im(F_{2A}^\gamma) + PKZIm(F_{2A}^Z) \right] \end{aligned} \tag{B.5}$$

where $c_\gamma = 0.35, P = \pm 1$ (e^- polarization), $KZ = -0.6$ and considering $d_\gamma \approx c_\gamma = 0.35$. Measuring these observables for two polarizations one can very easily isolate each $F_{2A}^{\gamma,Z}$ term. This leads to the possibility to separate the contribution of the photon from the one of the Z boson.

Results

The analysis has been carried out on the same data sample than for the CP conserving couplings with full simulation of the ILD. The events generated with WHIZARD are restricted to the physics of the Standard Model so $F_{2A}^{\gamma,Z}$ form factors are all zero and the asymmetries defined in Equation B.5 should be zero too.

Figures B.1 and B.2 show the distribution of $O_\pm^{Re,Im}$ observables for both electron beams polarization. These distributions are indeed centered on the zero value

but with some asymmetries for the imaginary part, see Figure B.2. These asymmetries are due to the fact that the initial state of the system is not CP conserving by itself because of the different polarization of the electron and the positron beams.

Observable	Generated	RMS	Reconstructed	RMS
$\langle O_+^{Re} \rangle$	0.0032	0.46	0.0029	0.47
$\langle O_-^{Re} \rangle$	-0.0021	0.46	-0.0015	0.47
$\langle O_+^{Im} \rangle$	-0.083	0.50	-0.042	0.50
$\langle O_-^{Im} \rangle$	-0.081	0.50	-0.031	0.49
$A_{\gamma,Z}^{Re}$	0.0053	-	0.0044	-
$A_{\gamma,Z}^{Im}$	-0.0022	-	-0.011	-

Table B.1: Mean value and RMS of the $O_\pm^{Re,Im}$ observables for left handed electron beam.

Observable	Generated	RMS	Reconstructed	RMS
$\langle O_+^{Re} \rangle$	-0.0037	0.46	-0.0029	0.47
$\langle O_-^{Re} \rangle$	-0.0011	0.46	0.0073	0.47
$\langle O_+^{Im} \rangle$	0.094	0.50	0.10	0.50
$\langle O_-^{Im} \rangle$	0.094	0.50	0.11	0.49
$A_{\gamma,Z}^{Re}$	-0.0025	-	-0.010	-
$A_{\gamma,Z}^{Im}$	0.0001	-	-0.0083	-

Table B.2: Mean value and RMS of the $O_\pm^{Re,Im}$ observables for right handed electron beam.

As shown in Table B.1 and B.2 the asymmetries value are compatible with the zero value, as expected for the Standard Model. The related errors on the form factors are given in Table B.3 [95]:

A study has also started to add non-zero CP violating terms in the framework of fast simulation [96]. These first studies show that the CP violating form factors can be fully disentangled at the ILC, with polarized beams, using optimized observables. The first results on the errors give an idea of the discriminating power of the ILC for the models of physics beyond the Standard Model.

In terms of dipole moment the precision is around $d_{top} \approx 10^{-19}\, e$.cm. However typical values for dipole moments are $d_e < 10^{-27}\, e$.cm for the electron and $d_n < 2.9 \times 10^{-26}\, e$.cm for the neutron. Therefore the order of magnitude better precision at the ILC with respect to the LHC may not be enough in terms of dipole moment, even if one may find stronger effects for the top quark. A potential source of CP

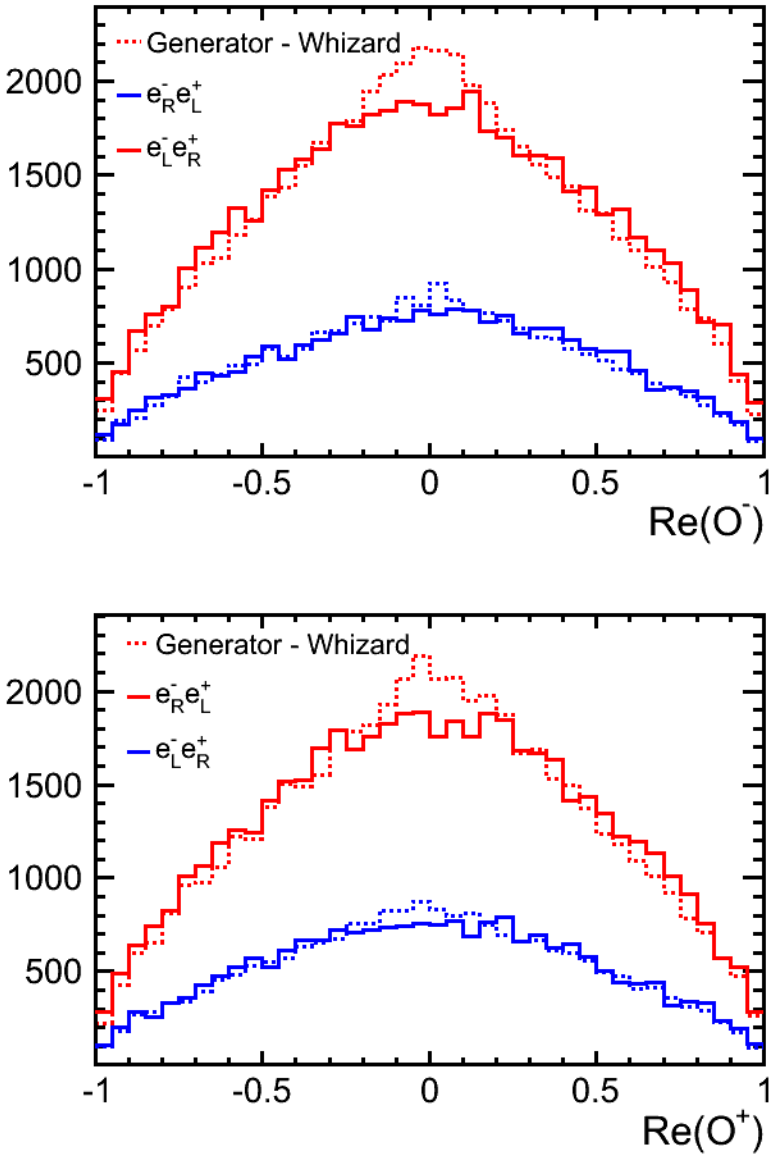

Figure B.1: Distribution of the real part of O for lepton charge $\pm$.

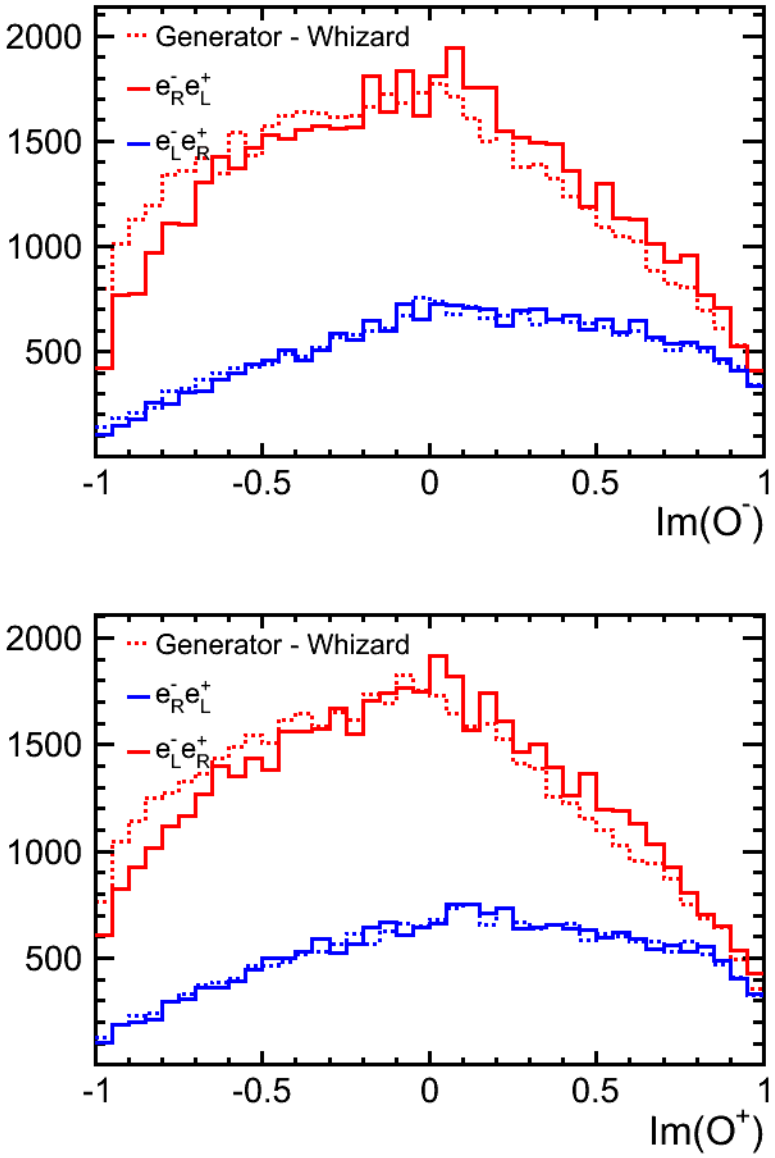

Figure B.2: Distribution of the imaginary part of O for lepton charge ±.

Form Factors	Standard Model value	LHC 300 fb^{-1}	TESLA 300 fb^{-1}	ILC 300 fb^{-1}
$Re(F_{2A}^{\gamma})$	0	± 0.17	± 0.007	± 0.004
$Re(F_{2A}^{Z})$	0	± 0.28	± 0.008	± 0.006
$Im(F_{2A}^{\gamma})$	0	± 0.17	± 0.008	± 0.006
$Im(F_{2A}^{Z})$	0	± 0.28	± 0.010	± 0.010

Table B.3: Errors on the CP violating form factors for the LHC, TESLA project and the ILC.

violation is the virtual Higgs exchange in $e^+e^- \to t\bar{t}$. This Higgs sector of the electroweak interaction can be CP violating and the cross section for the virtual exchange is larger near the $t\bar{t}$ threshold [94][95]. So the study should also be done near the $t\bar{t}$ threshold to evaluate the precisions that can be achieved here.

Appendix C

Résumé en français

Introduction

L'ILC

Un collisionneur linéaire électron-positon, pouvant atteindre une énergie dans le centre de masse d'au moins 500 GeV, devrait être le prochain grand projet de physique des particules. Il y a deux propositions pour un collisionneur linéaire : l'ILC (International Linear Collider) et CLIC (Compact Linear Collider) avec une énergie de centre de masse pouvant atteindre 3 TeV. L'ILC est un projet international pour un collisionneur linéaire e^+e^- avec une énergie dans le centre de masse pouvant aller jusqu'à 1 TeV (figure C.1).

Pour l'ILC, l'accélération sera effectuée par 16 000 cavités accélératrices supraconductrices basées sur la technologie de radiofréquence, tandis que CLIC est basé sur un concept d'accélération à deux faisceaux. Ce prochain collisionneur linéaire devrait être un complément au LHC (Large Hadron Collider) du CERN. En effet, à la différence du LHC où les collisions s'effectuent entre les protons, qui sont des particules composites, les électrons et les positrons sont des particules ponctuelles. Cela présente de nombreux avantages, comme la connaissance de l'état initial. Dans le cas du proton, l'énergie est partagée entre ses différentes composantes. Dans le cas des électrons, l'énergie est concentrée en un point.

L'objectif scientifique du futur collisionneur linéaire sera d'étudier en détail le boson de Higgs, nouvellement découvert au LHC en juillet 2012. Le collisionneur linéaire permettra également d'étudier le quark top, la matière noire et la nouvelle physique au-delà du modèle standard. Les objectifs du collisionneur linéaire en terme de physique exigent une excellente résolution d'énergie des jets et identification des particules dans l'état final multihadronic. Par conséquent, une nouvelle génération de détecteurs est développée pour cet accélérateur. Cette bonne résolution en énergie des jets est obtenue par l'algorithme de Particle Flow

(PFA), qui exige des calorimètres hautement granulaires. La collaboration de CALICE (CAlorimetry for the LInear Collider Experiments) étudie des concepts de calorimètres hautement granulaires pour les détecteurs du futur collisionneur linéaire. Les technologies employées sont également utiles pour des expériences non-ILC (comme PAMELA et PHENIX) et pour les applications au-delà de la physique des particules, telles que celles du médical.

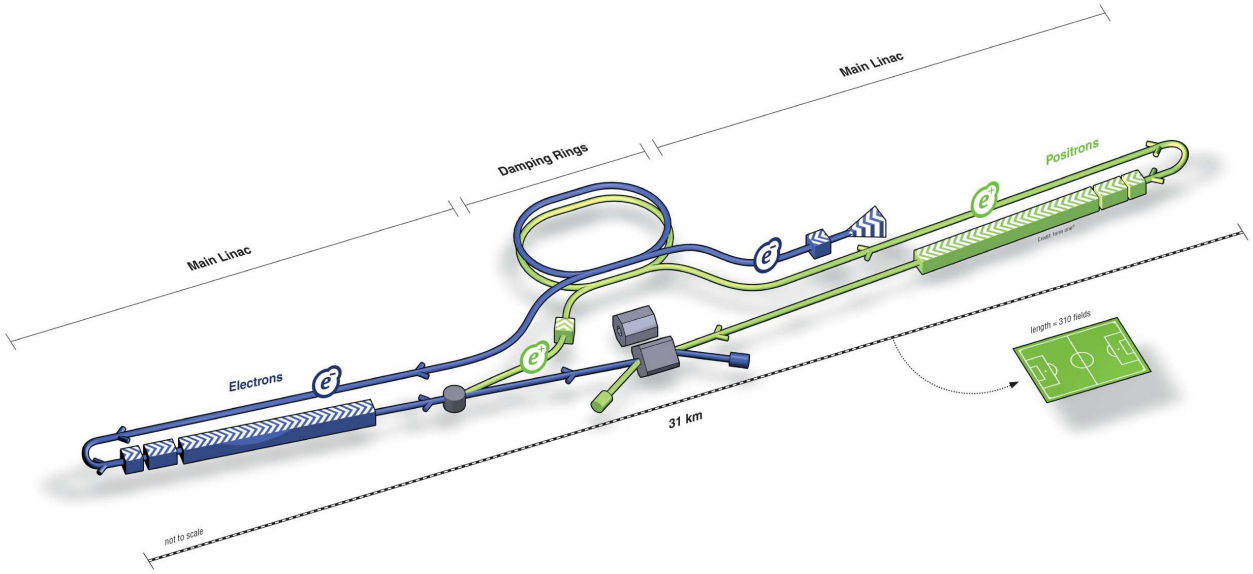

Figure C.1: Vue schématique de l'ILC.

L'ILD

L'ILC devrait avoir deux détecteurs qui vont fonctionner de manière alternative pour assurer la vérification des résultats. Le détecteur SiD (Silicon Detector) est basé sur une reconstruction des traces chargées à l'aide de détecteurs au silicium et va fonctionner dans un champ magnétique de 5 T. Le deuxième détecteur, l'ILD (International Large Detector), reconstruit de son coté les traces chargées dans un détecteur gazeux et aura un champ magnétique de 3,5 T. Comme montré dans la figure C.2, l'ILD est composé de plusieurs sous-détecteurs, placés les uns autour des autres. Une description de chaque système, tel que présent dans la simulation et en partant du plus proche du point d'interaction, est donnée ci-dessous:

– un détecteur de vertex à pixel multicouche (VTX). Le VTX permet la mesure de la position des particules chargées, et est optimisé pour une excellente résolution spatiale et une épaisseur minimale.

– une "Time Projection Chamber" (TPC) à grand volume avec jusqu'à 224 points par trace. La TPC, qui mesure la position des particules chargées, est optimisée pour une bonne résolution tridimensionnelle avec un minimum de matériel. Elle fournit également des capacités d'identification des particules basées sur la méthode dE/dx.
– un calorimètre électromagnétique, ECAL, hautement granulaire et ayant jusqu'à 30 couches en profondeur et une petite taille pour les cellules transversales. Il se compose de couches entrelacées d'absorbeurs en tungstène et de couches réactives en silicium. L'ECAL mesure les photons, les particules chargées et les hadrons neutres, qui laisseront une gerbe de particules secondaires en interagissant avec le tungstène.
– un calorimètre hadronique, HCAL, très segmenté avec jusqu'à 48 échantillons longitudinaux et une petite taille de cellule transversale. Il se compose de scintillateurs comme milieu actif et d'un matériau absorbeur en acier. Le HCAL mesure l'énergie déposée par les hadrons chargés et neutres.
– d'autres plus petits détecteurs calorimétriques permettent de couvrir 4π et de mesurer la luminosité.
– une bobine supraconductrice de volume important entourant les calorimètres, et créant un champ B axial de 3.5 Tesla. Elle fournit le champ magnétique nécessaire pour courber les particules chargées à l'intérieur du détecteur.
– un système d'acquisition (DAQ) de données sophistiqué qui fonctionne sans trigger externe, afin de maximiser la sensibilité physique.

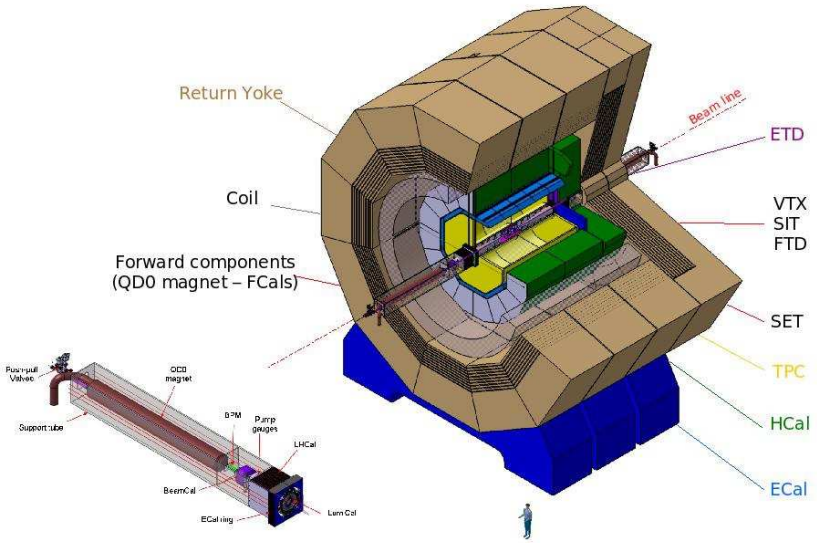

Figure C.2: Vue schématique de l'ILD.

Les calorimètres CALICE sont optimisés pour l'algorithme de particule Flow (PFA). L'idée du PFA est d'utiliser les sous-détecteurs les plus adaptés pour mesurer les propriétés de chacune des particules d'un jet. Cela signifie que les particules chargées (65 % de l'énergie du jet) seront mesurées à l'aide du tracker et pas dans les calorimètres. Les deux calorimètres, électromagnétiques et hadroniques, serviront à mesurer les particules neutres. Les photons (25 % de l'énergie du jet) seront mesurés dans le calorimètre électromagnétique, tandis que les hadrons neutres (10 % de l'énergie du jet) seront mesurés dans les calorimètres hadroniques et électromagnétiques. Le PFA est déjà appliqué, par CMS par exemple, mais avec des calorimètres non spécifiques, alors que la collaboration de CALICE travaille sur les calorimètres conçus pour le PFA. En effet, afin de réduire au minimum la confusion entre les particules chargées et neutres dans les calorimètres (menant à un double comptage/perte d'énergie), nous avons besoin de calorimètres hautement granulaires.

Le calorimètre éléctromagnétique silicium-tungstène

Un calorimètre électromagnétique de silicium tungstène (SiW-ECAL) est le choix standard pour des concepts de détecteurs ILD et SiD, proposé pour l'ILC. Le rôle principal de l'ECAL est de reconstruire les photons, même en présence de particules proches, et avec le calorimètre hadronique (HCAL) de mesurer l'énergie des gerbes de hadrons neutres. La physique de précision à l'ILC exige que les calorimètres restent à l'intérieur de la bobine magnétique. Avec ses faibles rayon de Moliere ($R_M = 9\,\text{mm}$) et longueur de rayonnement ($X_0 = 3.5\,\text{mm}$) le tungstène a été choisi comme matériau absorbeur. Le tungstène a également l'avantage d'avoir une grande longueur d'interaction ($\lambda_I = 96\,\text{mm}$), comparée à son X_0, ce qui conduit à une bonne séparation entre les photons et les hadrons. Du silicium avec une taille de pixel de $5 \times 5\,\text{mm}^2$ est utilisé comme matériau actif. Pour le design de référence de l'ILD, l'ECAL contient 30 couches, menant à 24 X_0 au total, équivalent à une longueur d'interaction.

Le prototype technologique du SiW-ECAL

Depuis 2007, un prototype technologique du SIW-ECAL est développé et testé. Ce prototype sera une preuve de la faisabilité technique du projet. Sa taille sera de 3/5 d'un module du coeur du détecteur ILD. Une grande structure mécanique en composite tungstène-carbone renforcé avec de l'époxy (CRP) a déjà été produite et testée avec succès. L'électronique frontale doit être intégrée à l'intérieur des couches de détecteurs (voir Fig. C.3 et Fig. C.4) pour garder le détecteur compact.

Les wafers de silicium sont la matière active du détecteur. Dans le prototype,

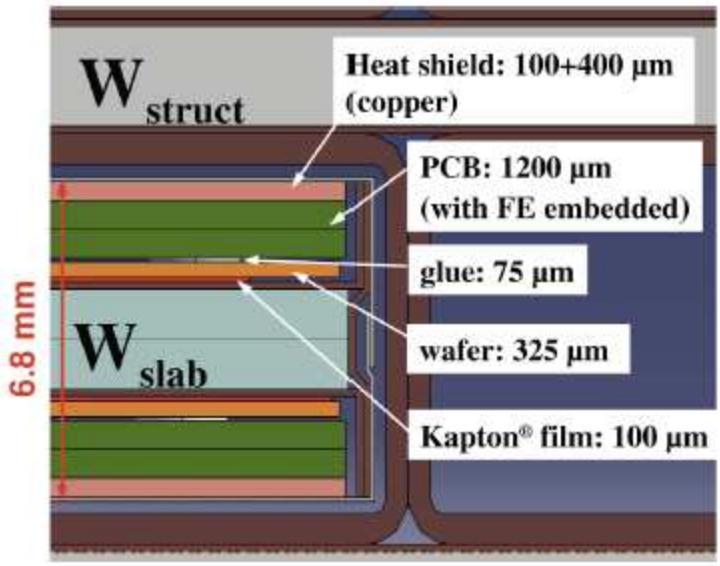

Figure C.3: Vue de coupe à travers une couche du prototype technologique.

des wafers de Si de $9 \times 9\,\mathrm{cm}^2$ avec une épaisseur de $320\,\mu$m sont utilisés. Le choix de la taille des pixels (5×5 mm^2) a été guidé par les études d'optimisation avec PFA.

Une unité de capteur actif (ASU) est l'entité composée des ASICs de lecture, d'une carte d'interface (PCB) et du wafer de silicium. L'ASIC SKIROC2 est conçu pour lire les wafers de silicium du SiW-ECA. C'est une puce de 64 canaux avec une gamme dynamique de 0,5 à $\approx$ 2500 MIPs et un système de déclenchement automatique à 50 % d'un signal de MIP. La taille de l'ASIC est de $7.2 \times 8.6\,\mathrm{mm}^2$. Les puces ne seront pas alimentées en continu afin de réduire la consommation

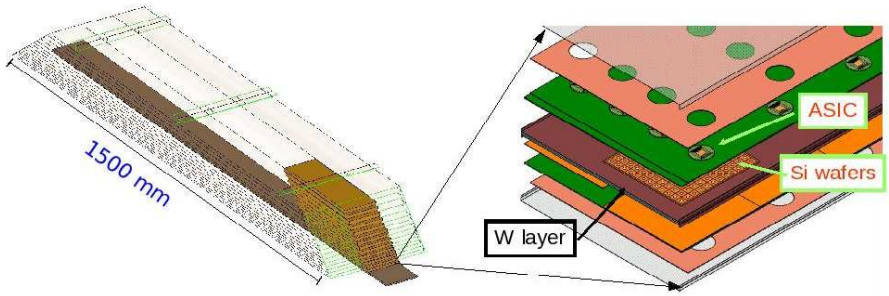

Figure C.4: à gauche: Esquisse des couches à l'intérieur de la structure mécanique du prototype technologique. à droite: Image éclatée d'une seule couche.

d'énergie jusqu'à 25 μW/ch en tirant parti de la structure temporelle du faisceau de l'ILC. Cette capacité est appelée le "Power Pulsing" ou power pulsé.

Résultats en test en faisceaux

Un premier prototype a été testé avec le faisceau d'électrons d'énergie de 1 à 6 GeV, à DESY en 2012 et 2013 (voir Fig. C.5). Le prototype est équipé de 6 à 10 couches, chacune avec un wafer de silicium de $9 \times 9\,\mathrm{cm}^2$ et 4 ASICs de lecture. La taille des pixels est 5×5 mm^2, donnant au total 1536 canaux fonctionnant avec le déclenchement automatique du SKIROC2, avec ou sans le mode power pulsé. Les résultats présentés par la suite sont obtenus après un filtrage des signaux parasites, venant principalement d'une gestion non optimale de l'alimentation de l'ASIC.

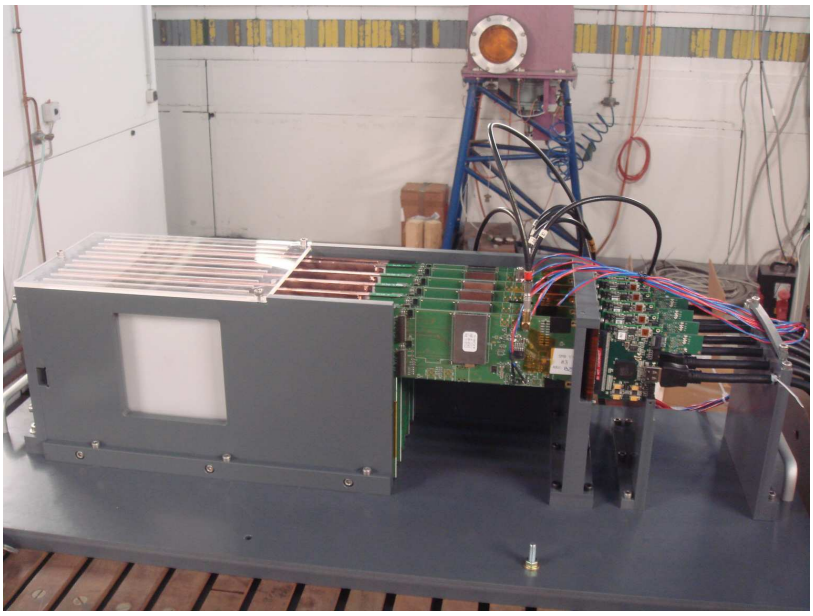

Figure C.5: Photo du prototype du SiW-ECAL testé en 2012 et 2013

.

Le but du test en faisceau était de déterminer le signal sur bruit du détecteur et d'établir une procédure d'étalonnage pour tous les canaux. Le signal sur bruit est défini comme le rapport entre la distance Piédestal- MIP et le sigma du piédestal (voir Fig. **??**).

Le signal sur bruit est supérieur à 10 dans toutes les cellules actives des couches à l'étude (voir Fig. C.7). Néanmoins, il existe un effet visible sur la Figure C.7 avec les deux puces sur la droite qui ont un signal sur bruit plus faible. Cela est dû au fait que ces ASICs ont une plus grande largeur du piédestal en raison d'une ligne électrique plus longue dans le routage du PCB.

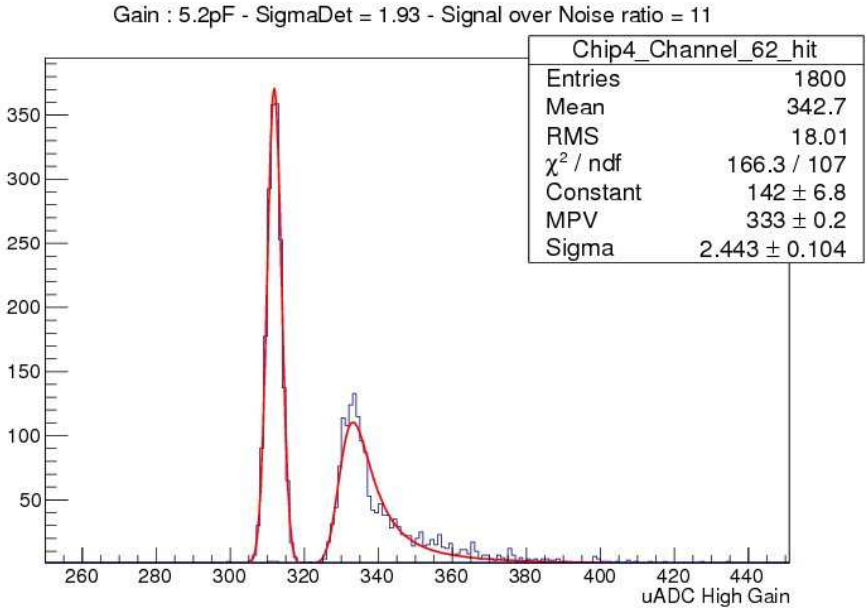

Figure C.6: Piédestal et distribution de MIP pour un canal.

Des études similaires ont également été menées en mode power pulsé. Elles ont montré que ce mode pouvait très bien fonctionner, comme illustré sur la figure C.8 pour les deux ASICs de gauche (M1 et M3). Au contraire pour les deux ASICs de droite (M2 et M4), dont le bruit est déjà supérieur en alimentation continue, l'effet est amplifié par le mode power pulsé.

Conclusion

Les premiers résultats du prototype technologique SiW-ECAL ont été très encourageants. La moyenne du signal sur bruit dépassait 10:1 pour tous les gains de preamplifier de l'ASIC. Cette valeur doit être comparée avec l'objectif de *R&D* de 10:1 et aussi avec la valeur de 7.5:1 réalisée par le prototype physique dans les mêmes conditions d'utilisation. D'autres améliorations peuvent être attendues une fois que les sources de bruit, qui ont été identifiées dans cette analyse, seront éliminées. Par exemple pour le prototype, l'excellent signal sur bruit a été compromis par des lignes de connexion trop longues sur la carte d'interface, une lacune qui sera réglée sur les futures versions de cette carte. L'essai du mode "power pulsé" fut aussi fructueuse. Du comportement des ASICs M1 et M3, nous avons appris que le mode power pulsing peut très bien fonctionner. Mais nous avons également appris des ASICs M2 et M4, que les détails de conception tels que le routage du PCB jouent un rôle important pour ce mode. La prochaine étape de *R&D* est de produire des ASUs avec quatre wafers et 16 ASICs. Cette étape comprend

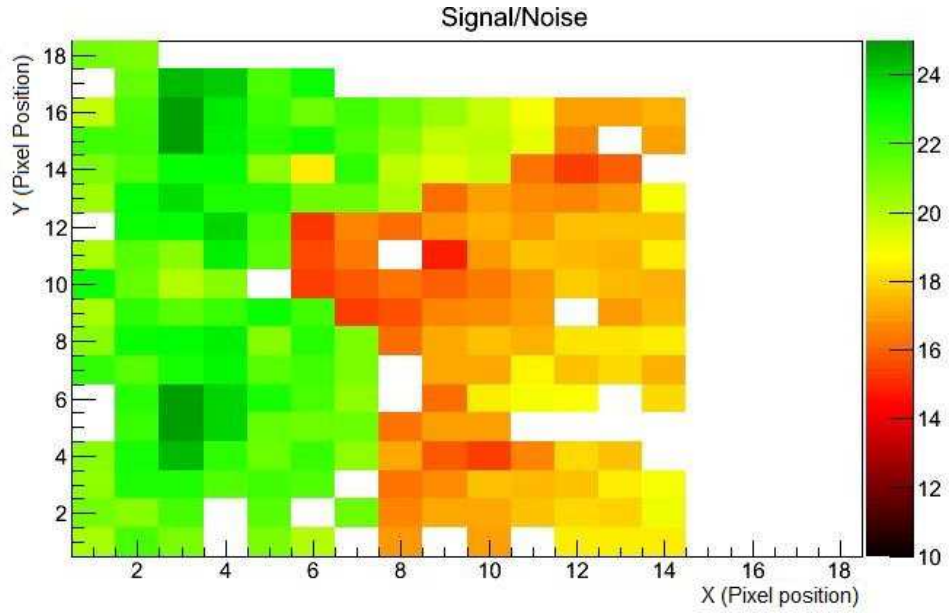

Figure C.7: Carte du signal sur bruit d'une seule couche. Les pixels blancs sont ceux éteints, principalement en raison de détails dans le routage du PCB.

d'autres études du PCB en ce qui concerne l'épaisseur et la planéité. La meilleure compréhension des performances du SKIROC2 permet aussi un nouveau cycle de développement de l'ASIC (SKIROC2b). La longueur des modules détecteur ECAL sera égale à 2,5 m, donc des prototypes avec des couches plus longues vont également être testés au cours de 2014. Les groupes de *R&D* travaillent maintenant à rendre possible le test de couches en mode power pulsé dans un champ magnétique afin d'étudier le comportement électrique et mécanique.

Le quark top à l'ILC

Le quark top est un composant très intéressant du Modèle Standard en raison de sa très haute masse, comparable à l'échelle de grandeur de la brisure de symétrie électromagnétique. Les couplages électrofaibles du quark top sont un bon test du Modèle Standard et pourraient être une bonne sonde de la physique au-delà du Modèle Standard. L'objectif de cette étude est d'estimer les erreurs sur les couplages électrofaibles qui peuvent être atteints à l'ILC. L'étude est réalisée à $\sqrt{s} = 500\,\text{GeV}$ avec une luminosité intégrée de $500\,\text{fb}^{-}1$. L'ILC permettra d'avoir des faisceaux d'électrons et de positrons polarisés, et donc les quarks t et $\bar{t}$ seront orientés vers différentes régions angulaires du détecteur. Ces différentes régions seront enrichies quark top d'hélicité gauche ou droite. Cela signifie qu'il est pos-

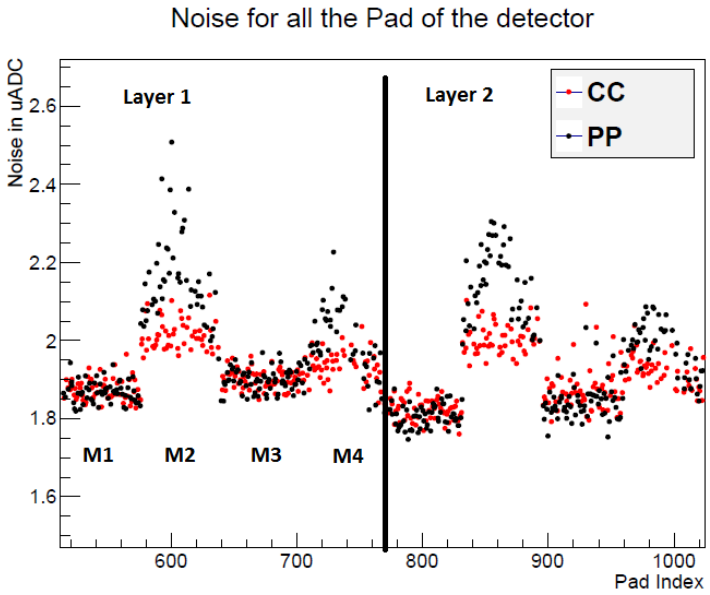

Figure C.8: Bruit dans les canaux de 2 couches du prototype dans les deux modes d'alimentation.

sible d'avoir accès de façon indépendante aux parties chirales gauche et droite du couplage du quark top avec le boson Z^0 et le photon. Pour mesurer les six facteurs de forme qui conservent CP, $F_{1V}, F_{1A} et F_{2V}$ pour chaque état d'hélicité, l'analyse a utilisé la mesure de la section efficace, de l'asymétrie avant-arrière A_{FB}^t et de l'asymétrie de l'hélicité pour deux paramètres de polarisation différents.

L'analyse

L'étude suppose une énergie dans le centre de masse de $\sqrt{s} = 500\,\text{GeV}$ et une luminosité intégrée de $500\,\text{fb}^-1$. La luminosité est également partagée entre les différentes polarisations des faisceaux. L'analyse est basée sur une simulation complète du détecteur ILD faite pour le DBD. L'analyse part du processus $e^+e^- \to t\bar{t}$.

Le quark top (anti-top) se désintègre presque exclusivement en une paire de bW. Le quark b s'hadronise donnant lieu à un jet. Le boson W peut se désintégrer hadroniquement en quarks légers, qui se transforment en jets, ou leptoniquement en une paire composée par un lepton chargé et un neutrino. Les processus semi-leptoniques sont définis par les événements dans lesquels un W se désintègre hadroniquement tandis que l'autre se désintègre leptoniquement, c'est-à-dire:

$$t\bar{t} \to (bW)(bW) \to (bqq')(bl\nu) \tag{C.1}$$

Dans le Modèle Standard la fraction des états finaux semi-leptoniques pour $e^+e^- \to t\bar{t}$ est d'environ 43 %.

Le lepton chargé permet la détermination de la charge du quark top. Le quark top est reconstruit à partir du boson W hadronique qui est combiné avec l'un des jets de quark b. Les leptons sont soit la particule la plus énergique dans un jet, soit ont une importante impulsion transverse par rapport aux jets voisins. En exploitant ces particularités, les leptons de décomposition peuvent être identifiés avec une efficacité d'environ 85 %. Des quatre jets, deux doivent être identifiés comme étant produits par les quarks b venant de la désintégration du quark top. Le b-tag est déterminé par un réseau de neurones qui utilise les informations du détecteur de traces comme entrée. Les vertex secondaires sont analysés au moyen de la masse du jet, la longueur de désintégration et la multiplicité des particules. Les jets avec le b-tag le plus haut sont sélectionnés (voir Fig. C.9). Enfin, les deux jets restants sont associés avec les produits de désintégration du W. Le signal est reconstruit en choisissant la combinaison jet b et W qui réduit au minimum l'équation suivante:

$$d^2 = \left(\frac{m_{\text{cand.}} - m_t}{\sigma_{m_t}}\right)^2 + \left(\frac{E_{\text{cand.}} - E_{\text{beam}}}{\sigma_{E_{\text{beam}}}}\right)^2 + \left(\frac{p_b^* - 68}{\sigma_{p_b^*}}\right)^2 + \left(\frac{\cos\theta_{bW} - 0.23}{\sigma_{\cos\theta_{bW}}}\right)^2 \tag{C.2}$$

Pour la détermination de l'asymétrie avant-arrière A_{FB}^t, le nombre d'événements dans les hémisphères du détecteur par rapport à l'angle polaire est compté. Encore une fois, l'analyse est effectuée séparément pour un faisceau d'électrons polarisés droite et gauche. Le résultat est donné dans la figure C.10.

La distribution reconstruite de l'angle polaire du quark top dans le cas des faisceaux d'électrons droit, en bleu sur la Figure C.10, est en accord avec celle générée. Pour le cas gauche, en rouge dans la Figure C.10, la distribution de $\cos\theta_t$ souffre de migrations d'événements passant de l'hémisphère avant à l'arrière. L'effet de migration dépend clairement de la polarisation du faisceau d'électrons et peut être expliqué par la cinématique de l'événement.

L'effet de migration pour les électrons gauches peut être supprimé en utilisant deux méthodes différentes. La première consiste à être plus strict sur la sélection des événements en appliquant une coupure sur le d^2 défini dans l'équation C.2. Le seconde méthode consiste à utiliser les détecteurs de traces pour mesurer la charge vertex du jet de b. Cela permet de lever l'ambiguité sur la combinaison du W avec le jet de b. Après avoir appliqué l'une des deux méthodes, la distribution pour les électrons gauches devient en accord avec celle générée (voir Fig. C.11).

Les résultats sur l'efficacité de reconstruction, A_{FB}^t et la pente de la distribution d'hélicité λ_t sont transformés en précisions sur les facteurs de forme $\tilde{F}_i$, en utilisant uniquement les erreurs statistiques. Les résultats sont résumés dans le tableau C.1

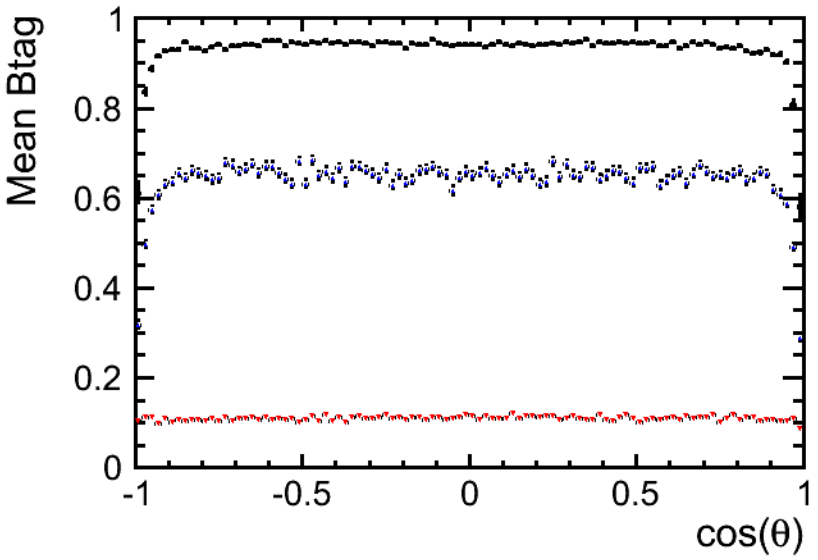

Figure C.9: Les valeurs de b-tag en fonction de l'angle polaire des jets. Les deux plus hautes valeurs de b-tag (points noirs et bleus) sont associés aux jets de quark b. Le troisième ensemble de valeurs (points rouges) est obtenu pour les jets de quarks légers.

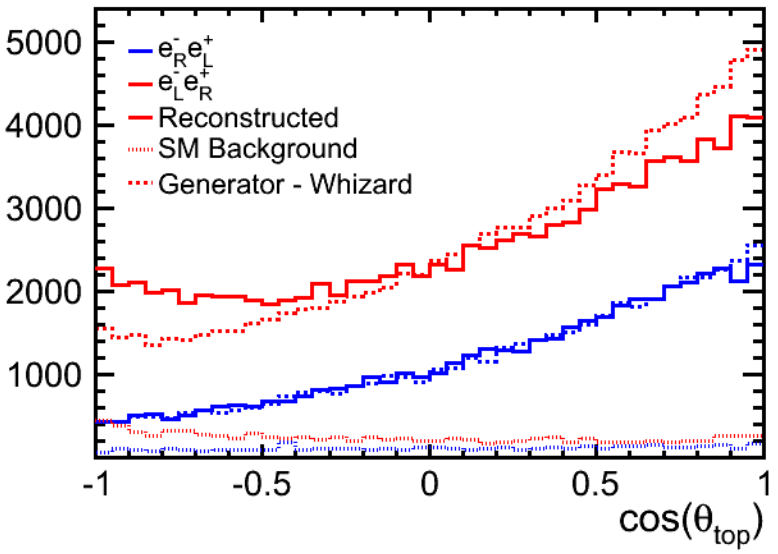

Figure C.10: Asymétrie avant-arrière reconstruite comparée à la prévision du générateur d'événement WHIZARD pour deux configurations des polarisations de faisceau.

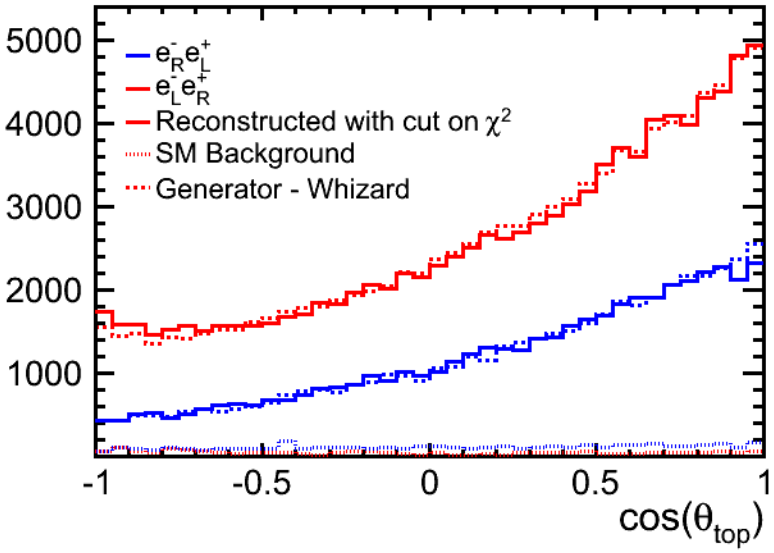

Figure C.11: Asymétrie avant-arrière reconstruite, ainsi que le bruit de fond du Modèle Standard par rapport à la prévision par le générateur d'événement WHIZARD après l'application d'une coupure sur $\chi^2 < 15$ pour le faisceau polarisé $\mathcal{P}, \mathcal{P}' = -1, +1$, comme il est expliqué dans le texte. Notez qu'aucune correction n'est appliquée pour le faisceau polarisé $\mathcal{P}, \mathcal{P}' = +1, -1$

et Figure C.12 et sont comparés avec les résultats des études antérieures pour un collisionneur linéaire e^+e^- tel que publié dans le TDR de TESLA, ainsi qu'avec les précisions obtenues dans une étude de simulation pour le LHC. Dans les études LHC et TESLA, un seul facteur de forme variait à la fois tandis que dans la présente étude les deux facteurs de forme $\tilde{F}_2$ ou les quatre $\tilde{F}_1$ sont variés en même temps.

Coupling	Standard Model value	LHC [] $\mathcal{L} = 300\, fb^{-1}$	e^+e^- [] $\mathcal{L} = 300\, fb^{-1}$ $\mathcal{P}, \mathcal{P}' = -0.8, 0$	e^+e^- ILC DBD $\mathcal{L} = 500\, fb^{-1}$ $\mathcal{P}, \mathcal{P}' = \pm 0.8, \mp 0.3$
$\Delta\tilde{F}_{1V}^{\gamma}$	0.66	$+0.043$	$-$	$+0.002$
		-0.041	$-$	-0.002
$\Delta\tilde{F}_{1V}^{Z}$	0.23	$+0.240$	$+0.004$	$+0.002$
		-0.620	-0.004	-0.002
$\Delta\tilde{F}_{1A}^{Z}$	-0.59	$+0.052$	$+0.009$	$+0.006$
		-0.060	-0.013	-0.006
$\Delta\tilde{F}_{2V}^{\gamma}$	0.015	$+0.038$	$+0.004$	$+0.001$
		-0.035	-0.004	-0.001
$\Delta\tilde{F}_{2V}^{Z}$	0.018	$+0.270$	$+0.004$	$+0.002$
		-0.190	-0.004	-0.002

Table C.1: Sensibilités réalisables à 68.3 % CL pour les facteurs de forme conservant CP $\tilde{F}_{1V,A}^{X}$ et $\tilde{F}_{2V}^{X}$ au LHC et à un collisionneur linéaire e^+e^-. Dans les études LHC et dans des études antérieures pour un collisionneur linéaire e^+e^- tel que publié dans l'étude du TDR de TESLA, un seul couplage à la fois est autorisé à s'écarter de sa valeur du Modèle Standard. Dans la présente étude, dénotée comme ILC DBD, soit les quatre facteurs de forme $\tilde{F}_1$, soit les deux facteurs de forme $\tilde{F}_2$ peuvent varier indépendamment. Les sensibilités sont basées sur des erreurs statistiques uniquement.

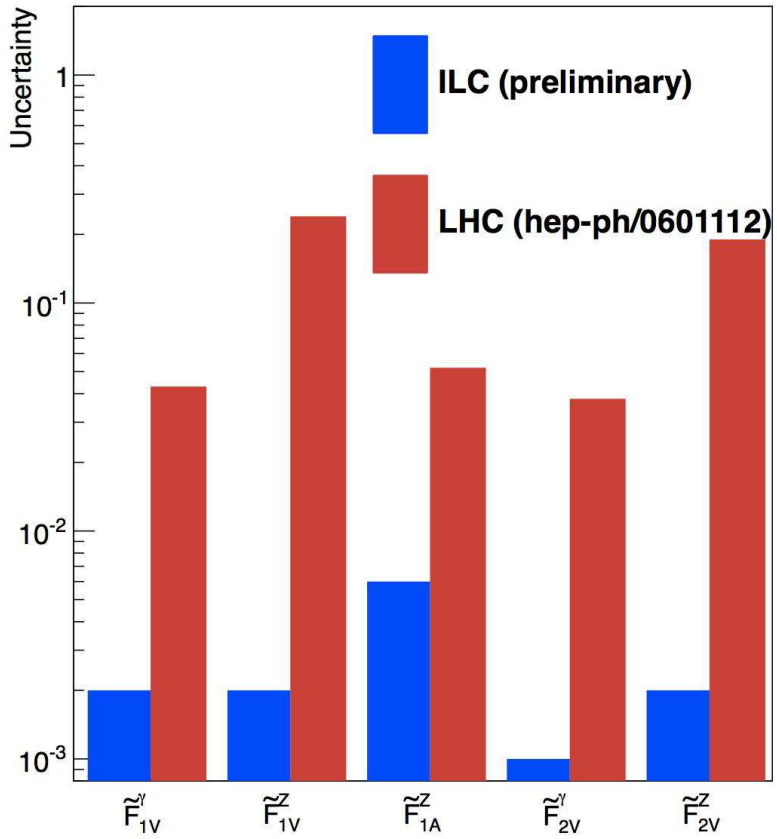

Figure C.12: Comparaison des précisions statistiques sur les facteurs de forme conservant CP attendues au LHC et à l'ILC. Les résultats LHC supposent une luminosité intégrée de $\mathcal{L} = 300\, fb^{-1}$. Les résultats de l'ILC supposent une luminosité intégrée de $\mathcal{L} = 500\, fb^{-1}$ à $\sqrt{s} = 500\,\text{GeV}$ et un faisceau polarisé $\mathcal{P}, \mathcal{P}' = \pm 0.8, \mp 0.3$.

Bibliography

[1] Particle Physics, third edition
B.R. Martin and G. Shaw, ISBN 978-0-470-03294-7.

[2] Quantum Electrodynamics.
R.P. Feynman.

[3] Fermi's Theory of Beta Decay (English Translation)
E. Fermi, 1934, American Journal of Physics.

[4] Partial Symmetries of Weak Interactions
S.L. Glashow, Nucl. Phys. 22:579, 1961.

[5] Weak and Electromagnetic Interactions
A. Salam, Proceedings of the Nobel Symposium, 1968.

[6] A Model of Leptons
S. Weinberg, Phys. Rev. Lett. 19:1264, 1968.

[7] F. J. Hasert *et al.*, Phys. Lett. 46B 138, 1973.

[8] Experimental Observation of Isolated Large Transverse Energy Electrons with Associated Missing Energy at $\sqrt{s} = 540\,\text{GeV}$
The UA1 Collaboration, Phys. Lett. B122:103, 1983.
Experimental Observation of Lepton Pairs of Invariant Mass Around 95 GeV at the CERN SPS Collider
The UA1 Collaboration, Phys. Lett. B126:398, 1983.

[9] Observation of Single Isolated Electrons of High Transverse Momentum in Events with Missing Transvers Energy at the CERN $\bar{p}p$ Collider
The UA2 Collaboration, Phys. Lett. B122:477, 1983.
Evidence for $Z^0 \to e^+e^-$ at the CERN $\bar{p}p$ Collider
The UA2 Collaboration, Phys. Lett. B129:130, 1983.

[10] Broken Symmetries
J. Goldstone, A. Salam and S. Weinberg, Phys. Rev. 127, 965.
Quasi-Particles and Gauge Invariance in the Theory of Super-conductivity
Y. Nambu, Phys. Rev. 117, 648.

[11] Broken Symmetries, Massless Particles and Gauge Fields
P.W. Higgs, Phys. Lett. 12:132, 1964.

[12] The Particle Data Group
`http://pdg.lbl.gov`

[13] Observation of a new particle in the search for the Standard Model Higgs boson with the ATLAS detector at the LHC.
Physics Letters B, Volume 716, Issue 1, 17 September 2012, Pages 1-29.
arXiv:1207.7214 [hep-ex]

[14] Observation of a new boson at a mass of 125 GeV with the CMS experiment at the LHC.
Physics Letters B, Volume 716, Issue 1, 17 September 2012, Pages 30-61.
arXiv:1207.7235 [hep-ex]

[15] Evidence for the spin-0 nature of the Higgs boson using ATLAS data
The ATLAS Collaboration, 4 July 2013
arXiv:13071432v1[hep-ex]

[16] Observation of tau neutrino interactions
K. Kodama *et al.*, DONUT Collaboration, Phys. Lett. B 504(3):218, 2001.

[17] Evidence for Anomalous Lepton Production in e^+e^- Annihilation
M.L. Perl *et al.*, Phys. Rev. Lett. 35(22):1489, 1975.

[18] CP Violation in renormalizable theory of Weak Interaction.
M. Kobayahi and T. Maskwa, Progress of Theoretical Physics Vol 49. Feb 1973.

[19] Observation of Top Quark Production in $\bar{p}p$ Collisions with the Collider Detector at Fermilab
CDF Collaboration, Phys. Rev. Lett.74:2626, 1995, arXiv:hep-ex/9503002v2.

[20] Observation of Top Quark
D0 Collaboration, Phys. Rev. Lett. 74:2632, 1995, arXiv:hep-ex/9503003

[21] Unitary Symmetry and Leptonic Decays
N. Cabibbo, Phys. Rev. Lett. 10:531-533, 1963.

[22] "Report of the 2005 Snowmass top/QCD working group"
A. Juste, Y. Kiyo, F. Petriello, T. Teubner, K. Agashe, *et al.*, arXiv:hep-ph/0601112 [hep-ph].

[23] The global electroweak Standard Model fit after the Higgs discovery
M. Baaka, R. Kogle, arXiv:1306.0571 [hep-ph].

[24] Electroweak symmetry breaking from dimensional deconstruction
N. Arkani-Hamed, A. G. Cohen, H. Georgi, Phys. Lett. B 513:232, 2001.

[25] Planck 2013 results XVI. Cosmological parameters
Planck Collaboration, arXiv:astro-ph.CO/1303.5076, 2013.

[26] A Multi-TeV linear collider based on CLIC Technology
M. Aicheler *et al.*, http://project-clic-cdr.web.cern.ch/project-clic-cdr/CDR_Volume1.pdf.

[27] Reference Design Report
International Linear Collider, http://ilcdoc.linearcollider.org/record/6321/files/ILC_RDR_Volume_3-Accelerator.pdf.

[28] "ILC TDR and DBD" ILC-Report-2013-040
T. Behnke *et al.*, http://www.linearcollider.org/ILC/Publications/Technical-Design-Report.

[29] SiD Detector Outline Document
http://hep.uchicago.edu/~oreglia/siddod.pdf.

[30] http://ilcild.org/.

[31] Undulator-Based Production of Polarized Positrons
G. Alexander *et al.*, arXiv:0905.3066 [physics.ins-det].

[32] Particle Flow Calorimetry and the PandoraPFA Algorithm.
M. A. Thomson, Nucl. Instr and Meth. A611:25, 2009, arXiv:0907.3577v1.

[33] TESLA Design Report
http://tesla.desy.de/new_pages/TDR_CD/start.html.

[34] The Calorimetry at the future e^+e^- linear collider
J. C. Brient and H. Videau, arXiv:hep-ex/0202004v1.

[35] CALICE Collaboration.
http://twiki.cern.ch/twiki/bin/view/CALICE/WebHome.

[36] Design and Electronics Commissioning of the Physics Prototype of a SiW Electromagnetic Calorimeter for the ILC
The CALICE Collaboration, J. Repond *et al.*, JINST 3:P08001, 2008, arXiv:0805.4833v1.

[37] Higgs Recoil Mass and Cross-Section Analysis at ILC and Calibration of the CALICE SiW-ECAL Prototype
Hengne Li, PhD Thesis, 2009, http://tel.archives-ouvertes.fr/tel-00430432/fr/.

[38] Response of the CALICE SiW Electromagnetic Calorimeter Physics Prototype to Electrons
CALICE Collaboration, J. Repond *et al.*, Nucl. Instr. Meth A608:372, 2009, arXiv:0811.2354v1.

[39] Study of the response of the CALICE Si-W ECAL Physics Prototype to positrons using data taken at the Fermilab test beam facility
CALICE Collaboration, J. Repond *et al.*, CALICE analysis notes.

[40] Position and Angular Resolution of the SiW-ECAL Prototype
M. Faucci-Giannelli, Calice Analysis Note, in preparation.

[41] Hadrons in a highly granular SiW-ECAL, Top quark production at the ILC
P. Doublet, PhD Thesis, 2011, `http://tel.archives-ouvertes.fr/tel-00657967`.

[42] Interactions of Pions in the CALICE Silicon-Tungsten Calorimeter Prototype
Naomi van der Kolk, Publication in progress.

[43] JRA3 electromagnetic calorimeter technical design report
M. Anduze, D. Bailey, R. Cornat, P. Cornebise, A. Falou, J. Fleury, J. Giraud, M. Goodrick, D. Grondin, B. Hommels, R. Poeschl, and R. Thompson, Technical Report EUDET-Report-2009-01, EUDET, 2009.

[44] The International Large Detector. Letter of Intent
`http://ilcild.org/documents/ild-letter-of-intent/LOI/20Feb2010.pdf`.

[45] SKIROC2 datasheet
`http://omega.in2p3.fr`.

[46] SKIROC2, front end chip designed to readout the Electromagnetic CALorimeter at the ILC
S. Callier, F. Dulucq, C. de La Taille, G. Martin-Chassard, and N. Seguin-Moreau, Journal of Instrumentation, 6(12):C12040, 2011.

[47] Construction and Testing of a Large Scale Prototype of a Silicon Tungsten Electromagnetic Calorimeter for a Future Lepton Collider
J. Rouënné, Proceedings of the Vienna Conference on Instrumentation, 2013, NIMA55701.

[48] Beam test performance of the SKIROC2 ASIC
T. Frisson *et al.*, Publication in progress.

[49] Development of a modular and scalable data acquisition system for calorimeters at a linear collider
M. J.Goodrick *et al.*, Journal of Instrumentation, 6:10011, October 2011.

[50] Acquisition system and detector interface for power pulsed detectors
R. Cornat. Physics Procedia, 37(0):1791-1798, 2012, Proceedings of the 2nd International Conference on Technology and Instrumentation in Particle Physics (TIPP 2011).

[51] SKIROC measurements, problems and solutions
S. Callier and N. Seguin-Moreau, 2012, Slides of a talk given at the CALICE electronics and DAQ and AHCAL main meeting.

[52] SiW-ECAL status and beam test in July
V. Balagura, 2013, Slides of a talk given at the CALICE meeting.

[53] Spin correlations in top quark pair production at e^+e^- colliders
S. J. Parke and Y. Shadmi, Phys.Lett. B387 (1996) 199–206, arXiv:hep-ph/9606419.

[54] Top quark production and decay at next-to-leading order in e^+e^- annihilation
C. R. Schmidt, Phys.Rev. D54 (1996) 3250–3265, arXiv:hep-ph/9504434.

[55] The Role of polarized positrons and electrons in revealing fundamental interactions at the linear collider
G. Moortgat-Pick, T. Abe, G. Alexander, B. Ananthanarayan, A. Babich, *et al.*, Phys.Rept. 460 (2008) 131–243, arXiv:hep-ph/0507011.

[56] T. Schwarz *et al.*, CDF Collaboration, CDF-Note 10584 (2011).

[57] V. M. Abazov *et al.*, D0 Collaboration, Phys. Rev. D 84, 112005 (2011).

[58] Inclusive and differential measurements of the $t\bar{t}$ charge asymmetry in proton-proton collisions at 7 TeV
CMS Collaboration, Phys. Lett. B 717 (2012) 129.

[59] The Top Quark Production Asymmetries A^t_{FB} and A^l_{FB}
E. L. Berger, Q.-H. Cao, C.-R. Chen, J.-H. Yu, and H. Zhang, Phys.Rev.Lett. 108 (2012) 072002, arXiv:1201.1790 [hep-ph].

[60] WHIZARD: Simulating Multi-Particle Processes at LHC and ILC
W. Kilian, T. Ohl, and J. Reuter, Eur.Phys.J. C71 (2011) 1742, arXiv:0708.4233 [hep-ph].

[61] O'Mega: An Optimizing matrix element generator
M. Moretti, T. Ohl, and J. Reuter, arXiv:hep-ph/0102195 [hep-ph].

[62] PYTHIA 6.4 Physics and Manual
T. Sjostrand, S. Mrenna, P. Skands, arXiv:hep-ph/0603175 [hep-ph].

[63] A_{FB} in Case of Polarised Beams
R. Poeschl, LAL internal note.

[64] Large mass hierarchy from a small extra dimension
L. Randall and R. Sundrum, Phys.Rev. Lett. 83(17):3370-3373, 1999.

[65] Resolving the A(FB)**b puzzle in an extra dimensional model with an extended gauge structure
A. Djouadi, G. Moreau, and F. Richard, Nucl.Phys. B773 (2007) 43–64, arXiv:hep-ph/0610173 [hep-ph].

[66] Forward-backward asymmetries of the bottom and top quarks in warped extra-dimensional models: LHC predictions from the LEP and Tevatron anomalies
A. Djouadi, G. Moreau, and F. Richard, Phys. Lett. B701 (2011) 458, arXiv:1105.3158 [hep-ph].

[67] Higgs boson mass and electroweak-gravity hierarchy from dynamical gauge-Higgs unification in the warped spacetime
Y. Hosotani and M. Mabe, Phys.Lett. B615 (2005) 257–265, arXiv:hep-ph/0503020 [hep-ph].

[68] Fermion Masses in Emergent Electroweak Symmetry Breaking
Y. Cui, T. Gherghetta, and J. Stokes, JHEP 1012 (2010) 075, arXiv:1006.3322 [hep-ph].

[69] Light Kaluza Klein States in Randall-Sundrum Models with Custodial SU(2)
M. S. Carena, E. Ponton, J. Santiago, and C. E. Wagner, Nucl.Phys. B759 (2006) 202–227, arXiv:hep-ph/0607106 [hep-ph].

[70] Light top partners and precision physics
C. Grojean, O. Matsedonskyi, G. Panico, 2013, arXiv:1306.4655.

[71] Present and future constraints on top EW couplings
F. Richard, 2014, arXiv:1403.2893.

[72] Constraining couplings of the top quarks to the Z boson in $t\bar{t}+Z$ production at the LHC
R. Roïtsch, M. Schulze, arXiv:1404.1005 [hep-ph].

[73] Longitudinally invariant Kt clustering algorithms for hadron hadron collisions
S. Catani, Y. L. Dokshitzer, M. Seymour, and B. Webber, Nucl.Phys. B406 (1993) 187–224.

[74] Hard QCD working group: Theory summary
W. J. Stirling, J.Phys. G17 (1991) 1567–1574.

[75] Beam-induced backgrounds in detectors at the ILC
A. Vogel, PhD thesis, Hamburg Univ., Hamburg, 2008.

[76] The LCFIPlus package
T. Suehara, `http://ilcagenda.linearcollider.org/getFile.py/access?contribId=183&sessionId=12&resId=1&materialId=slides&confId=5468`.

[77] The LCFIVertex package: vertexing, flavour tagging and vertex charge reconstruction with an ILC vertex detector
D. Bailey *et al.*, Nucl. Instrum. Meth. A610 (2009) 573-589, arXiv:0908.3019.

[78] Forward-Backward asymmetry in top pair production at the ILC
M. S. Amjad, PhD Thesis, 2014, `http://tel.archives-ouvertes.fr/tel-00949818`.

[79] Precision Electroweak Measurements on the Z Resonance
The ALEPH Collaboration, the DELPHI Collaboration, the L3 Collaboration, the OPAL Collaboration, the SLD Collaboration, the LEP Electroweak

Working Group, the SLD electroweak, heavy flavour groups, arXiv:hep-ex/0509008.

[80] Using the Semileptonic Decay of the B Meson to Measure the Charge of the Top Quark
J. Rouëné, 2014, Slides of a talk given at the FJPPL Top collaboration meeting.

[81] Impact of beam-beam effects on precision luminosity measurements at the ILC
C. Rimbault, P. Bambade, K. Monig, and D. Schulte, JINST 2 (2007) P09001.

[82] Measurement of the beam polarisation at the ILC using the WW annihilation data
A. Rosca, LC-REP-2013-009, `http://www-flc.desy.de/lcnotes/notes/LC-REP-2013-009.pdf`.

[83] Top quark mass measurements at and above threshold at CLIC
K. Seidel, F. Simon, M. Tesar, and S. Poss, 2013 , arXiv:1303.3758 [hep-ex].

[84] Reconstruction of heavy quark current correlators at $O(\alpha_s^3)$
Y. Kiyo, A. Maier, P. Maierhofer, and P. Marquard, Nucl.Phys. B823 (2009) 269–287, arXiv:0907.2120 [hep-ph].

[85] Two-Parton Contribution to the Heavy-Quark Forward-Backward Asymmetry in NNLO QCD
W. Bernreuther, R. Bonciani, T. Gehrmann, R. Heinesch, T. Leineweber, *et al.*, Nucl.Phys. B750 (2006) 83–107, arXiv:hep-ph/0604031 [hep-ph].

[86] Electroweak one loop corrections for e^+e^- annihilation into $t\bar{t}$ including hard bremsstrahlung
J. Fleischer, A. Leike, T. Riemann, and A. Werthenbach, Eur.Phys.J. C31 (2003) 37–56, arXiv:hep-ph/0302259 [hep-ph].

[87] Full $\mathcal{O}(\alpha)$ electroweak radiative correction to $e^+e^- \to t\bar{t}\gamma$ with GRACE-Loop
P. H. Khiem *et al.*, arXiv:1211.1112 [hep-ph].

[88] Measurement of associated production of vector bosons and top quark-antiquark pairs at $\sqrt{s} = 7\,\text{TeV}$
CMS Collaboration, S. Chatrchyan *et al.*, Phys.Rev.Lett. 110 (2013) 172002, arXiv:1303.3239 [hep-ex].

[89] Top quark properties in little Higgs models
C. Berger, M. Perelstein, and F. Petriello, arXiv:hep-ph/0512053 [hep-ph].

[90] Report of the 2005 Snowmass top/QCD working group
A. Juste *et al.*, arXiv:hep-ph/0601112.

[91] A precise determination of top quark electro-weak couplings at the ILC operating at 500 GeV
M.S. Amjad, M. Boronat, T. Frisson, I.Garcia Garcia, R. Poschl, E. Ros, F. Richard, J. Rouëné, P.Ruiz Femenia, M. Vos, 2013, arXiv:1307.8102, Publication in progress.

[92] Snowmass 2013 Top quark working group report
K. Agashe *et al.*, 2013, arXiv:hep-ph/1311.2028.

[93] Top quark physics: Theoretical aspects
W. Bernreuther, P. Igo-Kemenes, M. Jezabek, J. H. Kuhn, B. Lampe, O. Nacht- mann, P. Overmann and T. Schroder *et al.*, `http://inspirehep.net/record/325522?ln=en`.

[94] CP Nonconservation in Top Quark Production by (Un) Polarized e^+e^- and $\gamma\gamma$ Collisions
W. Bernreuther, A. Brandenburg, and P. Overmann, arxiv:hep-ph/9602.273.

[95] CPV with top quarks at ILC
F.Richard, `http://indico.lal.in2p3.fr/materialDisplay.py?contribId=3&materialId=slides&confId=2104`.

[96] Preliminary results for CP violating anomalous top-quark couplings at the ILC
I. Garcia, IFIC Valencia.